Int J Earth Sci (Geol Rundsch) (2018) 107:1059–1096
https://doi.org/10.1007/s00531-017-1515-4

ORIGINAL PAPER

# Petrography, geochemistry, and U–Pb geochronology of pegmatites and aplites associated with the Alvand intrusive complex in the Hamedan region, Sanandaj–Sirjan zone, Zagros orogen (Iran)

**Ali Asghar Sepahi**[1] · **Sedigheh Salami**[1] · **David Lentz**[2] · **Christopher McFarlane**[2] · **Mohammad Maanijou**[1]

Received: 13 December 2016 / Accepted: 1 July 2017 / Published online: 17 July 2017

**Abstract** The Alvand intrusive complex in the Hamedan area in Iran is in the Sanandaj–Sirjan zone of the Zagros orogen. It consists of a wide range of plutonic rocks, mainly gabbro, diorite, granodiorite, granite, and leucogranites that were intruded by aplitic and pegmatitic dykes. At least three successive magmatic episodes generated an older gabbro–diorite–tonalite assemblage, followed by a voluminous granodiorite–granite association, which was then followed by minor leucocratic granitoids. Aplitic and pegmatitic dykes and bodies have truncated both plutonic rocks of the Alvand intrusive complex and its metamorphic aureole. Chemically they belong to peraluminous LCT (Li-, Cs-, and Ta-bearing) family of pegmatites. Mineralogically, they resemble Muscovite (MS) and Muscovite Rare Element (MSREL) classes of pegmatites. High amounts of some elements, such as Sn (up to 10,000 ppm), Rb (up to 936 ppm), Ba (up to 706 ppm), and LREE (up to 404 ppm) indicate the highly fractionated nature of some of these aplites and pegmatites. U–Pb dating of monazite, zircon, and allanite by LA-ICPMS indicate the following ages: monazite-bearing aplites of Heydareh-e-Poshteshahr and Barfejin areas, southwest of Hamedan, give an age range of 162–172 Ma; zircon in Heydareh-e-Poshteshar gives an average age of ~165 Ma and for allanite-bearing pegmatites of Artiman area, north of Tuyserkan, an age of 154.1 ± 3.7 Ma was determined. These overlap with previously reported ages (ca. 167–153 Ma) for the plutonic rocks of the Alvand complex. Therefore, these data reveal that the Jurassic was a period of magmatism in the Hamedan region and adjacent areas in the Sanandaj–Sirjan zone, which was situated at the southern edge of the central Iranian microplate (southern Eurasian plate) at this time. Our results also suggest that advective heating in a continental arc setting has caused melting of fertile supracrustal lithologies, such as meta-pelites. These partial melts were then emplaced at much higher crustal levels, but within a thermally anomalous environment, which, therefore, leads to formation of evolved felsic rocks, such as the studied LCT aplite–pegmatite suite and their parental granitic rocks. This is a new result that indicates the role of syn-subduction crustal partial melting in the region as part of Zagros orogeny.

**Keywords** Aplite · Pegmatite · Geochemistry · Geochronology · Hamedan · Sanandaj–Sirjan · Iran

## Introduction

In recent years many petrogenetic studies have been done on pegmatites and aplites, with a diversity of petrogenetic models suggested (e.g., Webber et al. 1999; Thomas et al. 2003, 2012; London 2008, 2014a, b; Simmons and Webber 2008; Nabelek et al. 2010; Cerný et al. 2012; London and Morgan 2012; Thomas and Davidson 2015; Dill 2015). In this paper, the complex petrogenetic problems surrounding pegmatology (e.g. Simmons et al. 2003) are not discussed, but petrography, whole rock geochemistry, mineral chemistry, and especially U–Pb dating of accessory minerals in pegmatites/aplites of the Hamedan region, Sanandaj–Sirjan zone, Zagros orogen, Iran, are presented.

Pegmatites usually have simple mineralogy comprised of quartz, feldspar, and mica as essential minerals,

---

✉ Ali Asghar Sepahi
aasepahi@gmail.com

[1] Department of Geology, Bu Ali Sina University, Mehdieh Street, Hamedan, Iran

[2] Department of Earth Sciences, University of New Brunswick, Fredericton, NB E3B 5A3, Canada

but they also contain minor amounts of minerals suitable for U–Pb geochronology, such as monazite, zircon, and allanite. Monazite [(LREE, Th) $PO_4$] is a common accessory mineral in many magmatic rocks and is widely used for U–Pb geochronology. The high Th and relatively high U contents together with negligible common Pb and high closure temperature to Pb diffusion are the key features of this mineral chronometer (e.g., Mezeme et al. 2006; Chen et al. 2006; Paquette and Tiepolo 2007; Martin et al. 2007; McFarlane and Luo 2012, and references therein). Zircon is also ideally suited for U–Pb dating, because of its moderate to high U concentration and high closure temperature to diffusion of Pb. Both monazite and zircon exclude Pb during crystallization such that their Pb-isotopic signatures are highly radiogenic (Crowley et al. 2008 and references therein; Liu et al. 2010 and references therein). Allanite is the rare earth element (REE) rich epidote-group mineral ($[Ca,REE,Th]_2[Fe,Al]_3Si_3O_{12}[OH]$). Allanite can provide complementary, or unique, geochronological information on many geological processes (McFarlane 2016). It occurs in a wide range of rock types, especially in metaluminous granites and pegmatites (Gregory et al. 2007 and references therein).

Previous ages obtained by K–Ar and Rb–Sr record Late Cretaceous dates for plutonic rocks of the Hamedan region (e.g., Valizadeh and Cantagrel 1975; Braud 1987; Baharifar et al. 2004; see also Sepahi et al. 2014 for a time-event table of the Sanandaj–Sirjan zone). In recent years, a few research studies have been published on zircon U–Pb geochronology for the Alvand intrusive complex in the Hamedan region and other plutonic complexes in adjacent areas in the Sanandaj–Sirjan zone of Iran. These studies have been done on zircons from the main plutonic rock samples. Ahmadi-Khalaji et al. (2007) reported U–Pb zircon ages of 169–172 Ma for the Boroujerd pluton (Bj on Fig. 1); U–Pb zircon geochronology of the Alvand Intrusive complex (Al on Fig. 1) indicated that this is a multiphase complex that intruded over a period of 14 Ma (153–167 Ma; Shahbazi et al. 2010), Mahmoudi et al. (2011) determined a Late Jurassic emplacement age for the Qorveh pluton (Qr on Fig. 1; 157–149 Ma), using the U–Pb dating method; LAICP-MS zircon U–Pb ages of the Suffiabad granite (near Qr on Fig. 1) have a range between 149 ± 2 and 144 ± 3 Ma (Azizi et al. 2011); U–Pb data on the granites with LAICP-MS yield a crystallization age of ~165 Ma for the Aligoudarz pluton (Ag on Fig. 1; Esna-Ashari et al. 2012); Chiu et al. (2013) reported a U–Pb age of 164.6 ± 2.1 Ma for the Kolah Ghazi granite (Kz on Fig. 1); for the Ghalaylan pluton near Qorveh (Qr on Fig. 1), zircon U–Pb yielded ages from 157.9 ± 1.6 to 155.6 ± 5.6 Ma (Azizi et al. 2015); Yajam et al. (2015) used SHRIMP U–Pb zircon dating to report 140–160 Ma ages for plutons of Qorveh region (Qr on Fig. 1). Granitoid rocks with a possible Jurassic age are also reported from several other areas in the SSZ, such as Jiroft (Ji on Fig. 1; 175.2 ± 1.8 Ma; Chiu et al. 2013) and Chah-Dozdan (Ch on Fig. 1; 173–164 Ma; Fazlnia et al. 2007).

Our work is the first attempt at monazite, zircon, and allanite U–Pb dating on aplites and pegmatites of the region. In this paper, the earlier (K–Ar and Rb–Sr data) to recent (U–Pb) published studies on dating of plutonic rocks of the Hamedan region and adjacent areas are compared with our analyses to interpret the tectono-magmatic history of the region. This new data fill gaps in the geochronological dataset and tectono-magmatic history of the Hamedan region and the Sanandaj–Sirjan zone, one of the important tectono-stratigraphic units of Iran. Also, the geochronological and genetic links between the aplitic and pegmatitic rocks of the Hamedan region and their host plutonic and metamorphic rocks have not been considered in earlier published research work; therefore, we have considered interpreting the tectono-magmatic history of the Hamedan region and the Sanandaj–Sirjan zone of Zagros orogen as a part of Alpine-Himalayan orogenic system.

## Regional geological setting

The Zagros Orogen is a part of the Alpine–Himalayan orogenic system. The Sanandaj–Sirjan zone (SSZ) or Zagros imbricate zone of the Zagros orogeny is comprised of a metamorphic belt of low- to high-grade regional and contact metamorphic rocks that has been intruded by mafic, intermediate, and felsic plutonic bodies (Alavi 1994, 2004) (Fig. 1). The SSZ, as one of the tectono-stratigraphic units of Zagros orogen, has a width of 150–250 km and length of 1500 km, extending from the northwest to southeast in Iran. The SSZ occurs between the Zagros fold-thrust belt and the southwestern boundary of the Urumieh–Dokhtar Magmatic Arc. This zone can be divided into five sub-zones, i.e., the Marginal sub-zone, Ophiolite sub-zone, Bisotun sub-zone, Radiolarite sub-zone, and Complexly deformed sub-zone. The Hamedan region is located in the northwestern part of the SSZ in a complexly deformed sub-zone (Fig. 1; Mohajjel et al. 2003). Major metamorphic and magmatic events in the northwestern part of the SSZ occurred during the Mesozoic era (e.g., Baharifar 1997; Sepahi 1999; Rashidnejad-Omran et al. 2002; Sheikholeslami et al. 2003; Sepahi et al. 2004; Baharifar 2004; Ahmadi-Khalaji et al. 2007; Aliani et al. 2012). The ages of the major granitic plutons of this part of the SSZ are Mesozoic–Paleogene, ~200 to ~40 Ma (e.g., Valizadeh and Cantagrel 1975; Braud 1987; Masoudi 1997; Baharifar 2004; Ahmadi-Khalaji et al. 2007; Arvin et al. 2007; Shahbazi et al. 2010; Mahmoudi et al. 2011; Ahadnejad et al. 2011; Azizi et al. 2011, 2015; Esna-Ashari et al. 2012; Chiu et al. 2013;

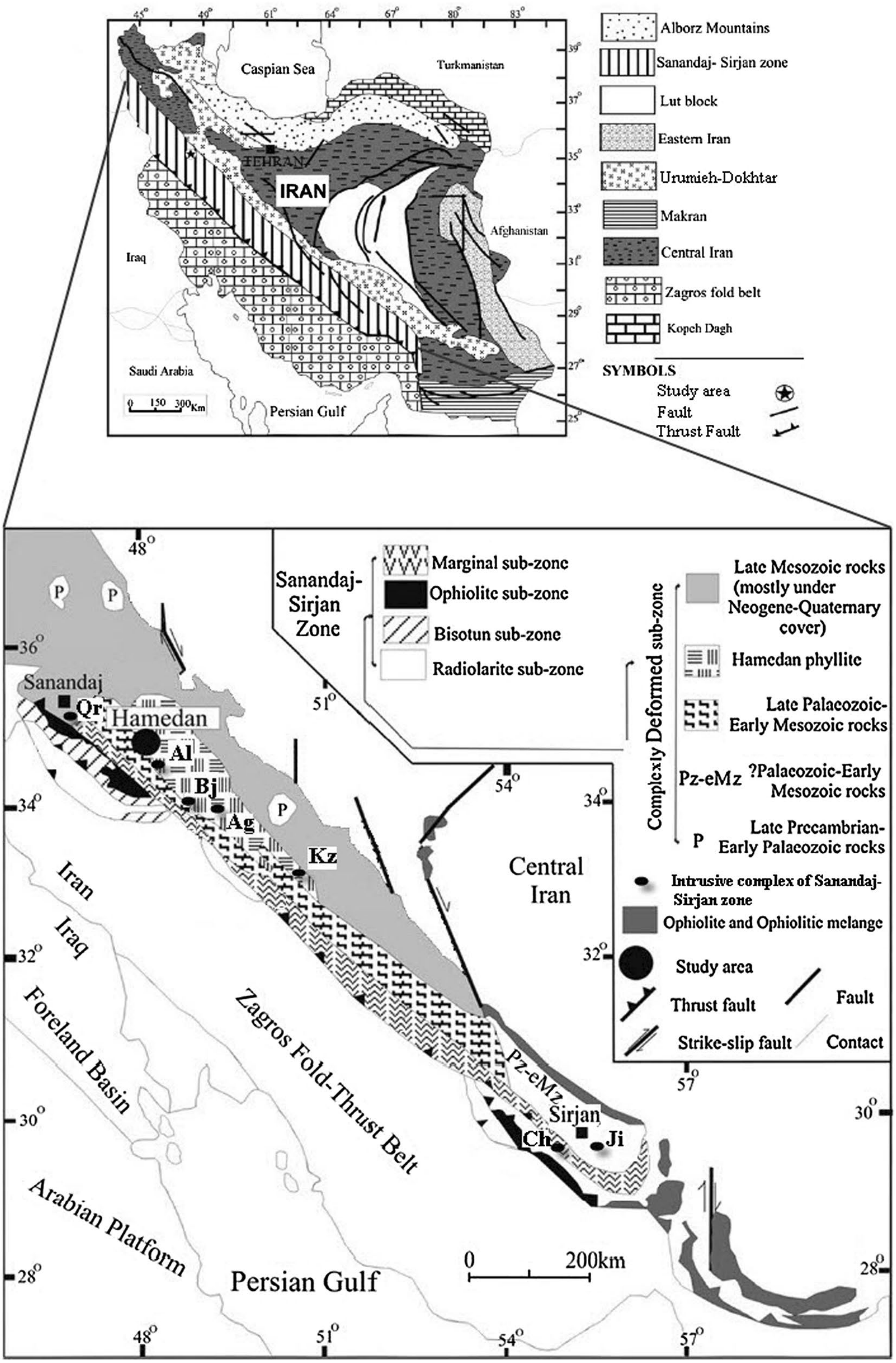

**Fig. 1** Simplified map showing major tectono-stratigraphic units of Iran and the Sanandaj–Sirjan zone, Zagros orogen, Iran. Plutons: *Qr* Qorveh, *Al* Alvand, *Bj* Boroujerd, *Ag* Aligoudarz, *Kz* Kolah-Ghazi, *Ch* Chahdozdan, *Ji* Jiroft (Modified after Mohajjel et al. 2003)

Sepahi et al. 2014). Locations of major plutons within the SSZ are shown in Fig. 1 (see the caption of Fig. 1). The metamorphic-magmatic events are considered to be related to the subduction of the Neo-Tethys oceanic crust beneath the central Iranian micro-continent (as southern part of Eurasia continent) and to the later collisional event of Afro-Arabia and Eurasia (e.g., Baharifar 1997, 2004; Sepahi 1999; Sepahi et al. 2004, 2014).

In the Hamedan region, various plutonic and metamorphic rocks crop out (Fig. 2). Plutonic rocks of the Alvand intrusive complex in the Hamedan region have been divided by Sepahi (2008) into three categories: gabbro–diorite–tonalite association, granite-granodiorite porphyroid (megacrystic), and hololeucocratic granitoids. Aplitic and pegmatitic dykes crosscut plutonic rocks of the complex. A middle Jurassic U–Pb age has been indicated for these plutonic rocks (e.g., Shahbazi 2010; Shahbazi et al. 2010; Mahmoudi et al. 2011; Chiu et al. 2013).

Metamorphic events in the Hamedan region predate major plutonic events and possibly occurred in Jurassic time. Multiple deformational phases have occurred in the metamorphic rocks through the known geologic time of

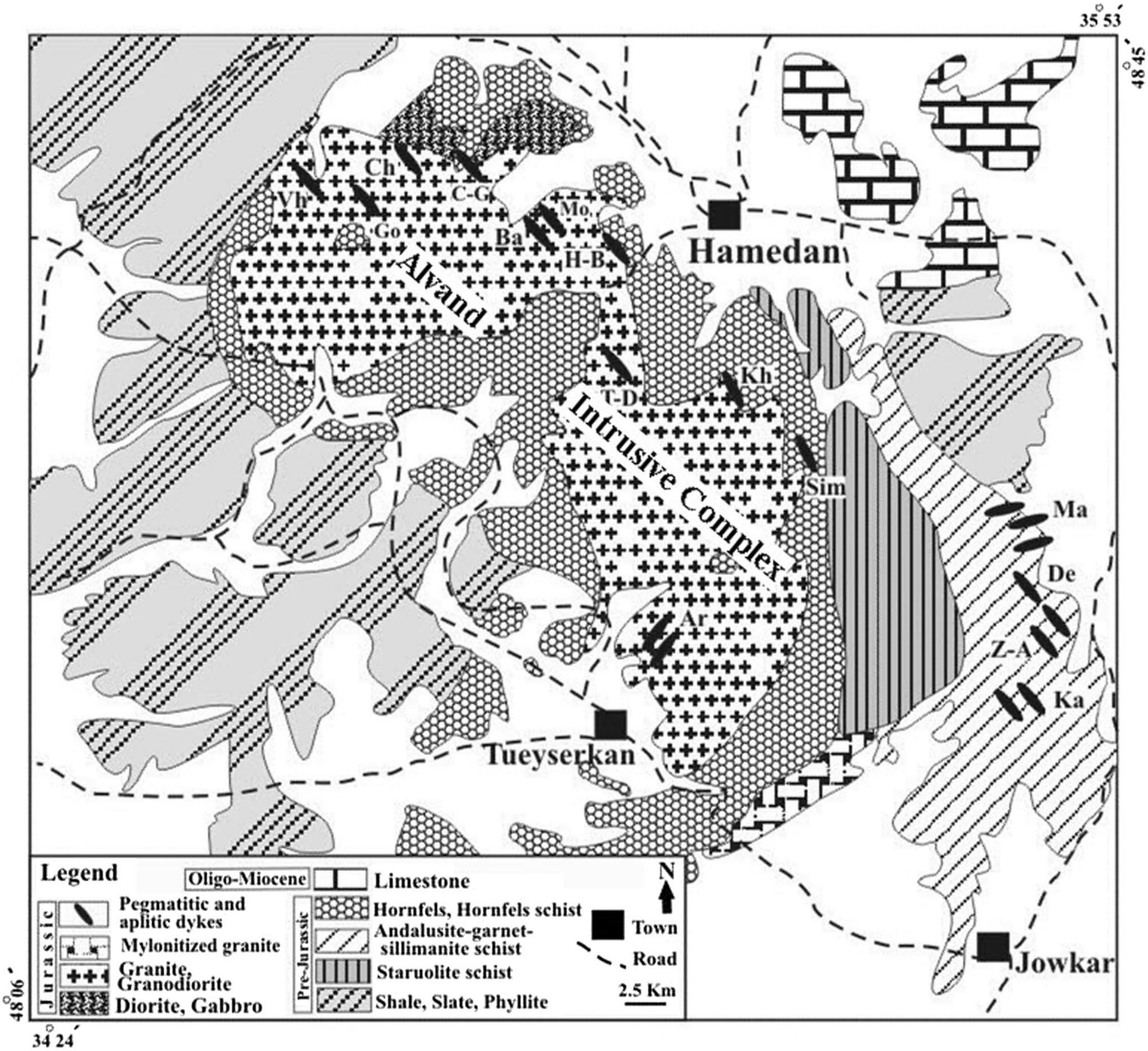

**Fig. 2** Simplified geological map of the Hamedan region (modified after 1/250,000 geological map, Geological Survey of Iran). Abbreviations of dyke locations; *Kh* Khaku, *T-D* Tarikdarreh, *H-P* Heydareh-e-Poshteshahr, *Ba* Barfejin, *Mo* Moeijin, *Go* Ghoshalan, *C-G* Cheshmeh-Ghassaban, *Ch* Chayan, *Vh* Vehnan, *Ar* Artiman, *Sim* Simin, *Ma* Mangavi, *De* Dehno, *Ka* Kamariand, *Z-A* Zaman-Abad. Samples for geochronological studies were collected from the Ar, Ba and H-P areas

this region (Izadikian 2009). Low- to high-grade metamorphic rocks with different compositions occur in the region. The main metamorphic rocks of the area are meta-pelites, but some meta-psammites, quartzites, meta-basites, calc-pelites, and calc-silicates also occur in the region. Meta-pelites are the most abundant lithology and include slate, phyllite, pelitic schist/migmatite, and hornfels (Fig. 2). Also, thin interlayers of amphibolite and amphibole schist occur in the metamorphic sequence. Various regional metamorphic zones including chlorite (±chloritoid), biotite, garnet, andalusite (chiastolite), sillimanite, and sillimanite-(±cordierite)-K-feldspar, and thermal (contact) metamorphic zones of cordierite (±andalusite, ±fibrolite), cordierite-K-feldspar, and sillimanite-K-feldspar are developed in the area in response to polyphase metamorphism. Major lithological units of the studied area are presented in the next section of the paper.

## Lithological units of the Hamedan area

A summary of lithologic units is shown in Fig. 2 with more detailed explanations of metamorphic and plutonic rocks following:

### Regional metamorphic rocks

Regional metamorphic rocks from low- to high-grade occur in the Hamedan region. The low P/high T (LP/HT) metamorphism of the region is characterized by the sequential development of various minerals, such as chlorite/chloritoid, biotite, garnet, andalusite (chiastolite), staurolite, sillimanite, and K-feldspar. Major metamorphic rocks of the region are as follows:

The low-grade rocks are very fine-grained slates and phyllites, interlayered with carbonate rocks, and quartzites. Slates contain quartz, sericite, chlorite, graphite, iron oxides, and pyrite. Phyllites contain quartz, chlorite, ±chloritoid, muscovite, and graphite. Mica schists show lepido-porphyroblastic texture. These rocks contain quartz, biotite, garnet, muscovite, and chlorite. Andalusite-bearing schists are medium to coarse grained, with porphyroblasts of garnet (up to 5 mm in diameter), and andalusite (chiastolite) crystals (up to 20 cm in length). Common minerals are quartz, biotite, andalusite (chiastolite), garnet, and muscovite. Staurolite schists are composed of quartz, staurolite, garnet, biotite, muscovite, chlorite, plagioclase, and graphite. Porphyroblasts of garnet are typically small (<5 mm), but staurolite crystals are as much as 10 cm long. Many quartzveins cut these metasedimentary rocks that are not common within the other lithologies in the region. Sillimanite-andalusite schists contain quartz, biotite, muscovite, plagioclase, and small garnet crystals (up to 1 mm) with large (5–10 cm long) porphyroblasts of andalusite partially replaced by prismatic sillimanite (±fibrolite). Kyanite schists/migmatites occur at scattered localities within other zones. They contain biotite + plagioclase + quartz + kyanite (±remnants of andalusite/sillimanite) ± garnet. In these rocks retrograde muscovite and chlorite occur as well. High-grade schists and migmatites occur in the vicinity of plutons in some places. In this zone sillimanite/andalusite schists/migmatites alternate with interlayers of cordierite-bearing migmatites. The highest grade schists in the regional metamorphic sequence contain sillimanite/andalusite (±kyanite) + quartz + biotite + muscovite + garnet + plagioclase + K-feldspar (perthitic orthoclase) ± staurolite. These schists grade into migmatitic rocks in which their mesosome mineralogy is similar to the mineral assemblages in the schists. These schists are cut by abundant granitic pegmatites, as well as sillimanite–quartz veins. Some inter-layers of cordierite migmatites occur in this zone and contain quartz, cordierite, andalusite/sillimanite, perthitic orthoclase, minor biotite, plagioclase, spinel (hercynite), and opaque minerals. This zone is associated with partial melting and development of granitic leucosomes in migmatites. Plagioclase-bearing leucosomes are predominant, but some contain K-feldspar. Mesosomes of migmatites have porphyro-lepidoblastic texture and contain quartz, biotite, garnet, and $Al_2SiO_5$ polymorphs, especially sillimanite (±andalusite/kyanite) ± staurolite ± graphite. Garnet crystals of millimeter to centimeter size (up to 2 cm) are common.

### Contact metamorphic rocks

Protoliths of the contact metamorphic rocks are similar to those in the regional metamorphic sequence and include abundant metapelitic rocks. Spotted schists contain spots of sericitized porphyroblasts of previous regional metamorphic rocks, such as staurolite and andalusite. Rocks with hornfelsic texture, but showing primary regional metamorphic assemblages, are common.

Cordierite (±andalusite) hornfels, cordierite-K-feldspar hornfels, sillimanite-K-feldspar hornfels, and sillimanite-(andalusite, ±kyanite)-garnet hornfels are major rock units in contact metamorphic sequences. Two metamorphic zones are widespread around plutonic bodies: cordierite ± andalusite and cordierite-K-feldspar zones. Also, a narrow sillimanite-K-feldspar zone is common around mafic bodies. The typical mineral assemblage of cordierite zone is quartz + biotite + cordierite ± garnet ± andalusite ± fibrolite + plagioclase + opaque minerals. Adjacent to the plutonic rocks (contact zone), there is a narrow zone of cordierite–orthoclase. This metamorphic zone is characterized by coexisting cordierite and perthitic orthoclase. The typical mineral assemblage of these rocks is similar to the cordierite zone, except for presence of perthitic orthoclase.

## Plutonic rocks

Various plutonic rocks, ranging from gabbro to diorite and granite crop out in the Hamedan region (Sepahi 1999, 2008). These were intruded by aplitic and pegmatitic dykes. In some places, the biotite granites–granodiorites contain feldspar phenocrysts and megacrysts. These rocks are composed of quartz, K-feldspar, plagioclase, and biotite; muscovite and zircon are accessory minerals. Some megacrysts of $Al_2SiO_5$-minerals, garnet, and cordierite occur in these rocks. Mafic rocks include gabbro to diorite. Gabbro has intergranular, ophitic, and sub-ophitic textures and is composed of clinopyroxene and plagioclase as major phases and olivine and hornblende as minor minerals. Diorites are composed of plagioclase, hornblende, and biotite as common minerals and contain accessory apatite and titanite. Small volumes of leucocratic granitoids crosscut other plutonic rocks in some localities. They are comprised of quartz and plagioclase as common minerals and accessory biotite, titanite, rutile, and zircon also occur.

The Alvand pluton (Hamedan) is a composite mesozonal pluton consisting of older mafic parts and younger felsic parts with sharp contacts between mafic and felsic plutonic facies. In some parts of pluton (in NW and SE) mafic rocks are autochthonous, but in many other parts they have been disrupted by younger plutonic phases producing enclaves and blocks of allochthonous mafic rocks inside younger felsic parts of the pluton. In the central parts of the pluton, small volumes of leucogranites crosscut older mafic and felsic rocks. Aplites and pegmatites crosscut different plutonic facies and their metamorphic country rocks (Sepahi 1999). U–Pb ages obtained by Shahbazi et al. (2010) are consistent with the intrusive order of various plutonic facies observed in this multiphase pluton.

The Alvand pluton has been emplaced in a compressional tectonic regime, because it shows preferred orientation of feldspar megacrysts and enclaves near the contact zone parallel to the pluton margin. Also, preferred orientation of porphyroblasts of minerals, such as cordierite in hornfelsic rocks near contact with plutonic rocks, confirms forceful intrusion of the pluton into country rocks. There is no evidence of ring dykes and cone sheets related to pluton emplacement (Sepahi 1999).

## Aplites and pegmatites

Outcrops with exposures of pegmatitic, aplitic, and composite aplitic and pegmatitic dykes intruding both plutonic rocks of the Alvand complex and surrounding regional and contact metamorphic rocks can be observed in the Hamedan region (Fig. 3). In this region, aplites and pegmatites are common in the interior and margin of the pluton and also in the exterior of the plutonic rocks. They crosscut various lithologies, such as granites, cordierite- and andalusite-hornfelses, and andalusite–sillimanite schists and migmatites (i.e., low pressure metamorphic environment). In areas such as Khaku, Tarikdarreh, Heydareh-e-Poshteshahr, Barfejin, Ghoshalan, Cheshmeh-Ghassaban, Chayan, Vehnan, and Artiman, these dykes intruded plutonic bodies and contact metamorphic rocks (hornfelses), but in some other places, such as Simin, Kamari, Zaman-Abad, Dehno, and Mangavi, they are exterior to the plutons and intrude regional metamorphic rocks (meta-pelitic schists/migmatites) (Fig. 2). Aplitic and pegmatitic dykes, cutting through the Alvand complex and its contact aureole, are thinner and show simple mineralogy and textures, but dykes in the exterior of the Alvand complex, which are hosted by medium- to high-grade metamorphic rocks, are thick, more complex in mineralogy and textures, and show well-defined internal zoning. Common features of aplites and pegmatites from various areas of the region have been classified in Table 1, and petrography of some aplitic and pegmatitic dykes is explained below. Typical geological features of the studied pegmatites are similar to Muscovite (MS) and Muscovite Rare Element (MSREL) classes in Cerný (1991) and Cerný et al. (2012) schemes of classification of pegmatite.

Aplitic and pegmatitic dykes in the interior and margin of the Alvand pluton do not show regular orientations and consist of network of veins that possibly filled synemplacement fractures inside the intrusive body. Dykes in Simin area appear to have resulted from migration of magma parallel to lithological contacts and tectonic foliation to accumulate in the shear zones (Fig. 3c). Most dykes in Kamari, Zaman-Abad, Dehno, and Mangavi areas have been intruded parallel to the foliation of their country rocks (commonly andalusite–sillimanite schists) (Fig. 4f).

### *Aplitic–pegmatitic dykes emplaced into the interior to plutonic rocks*

Aplitic–pegmatitic dykes of the Barfejin and Artiman areas crosscut granitic and dioritic rocks, and commonly are no more than 50 cm in width. In Barfejin area, they are aplitic and have typical hypidiomorphic granular texture, and are composed of quartz, perthitic K-feldspar, plagioclase, zoned tourmaline, zircon, and phosphate minerals, such as monazite, xenotime, apatite, and accessory amounts of U-silicate and U-oxide. Tourmalines show zoning with brown to dark blue color across the crystals. Samples Bar1 and Bar11 were collected from this area. In Artiman area, pegmatites are typical coarse-grained, but also have aplitic and graphic/granophyric textures in some parts. They appear as dykes of a few centimeters to a few meters in

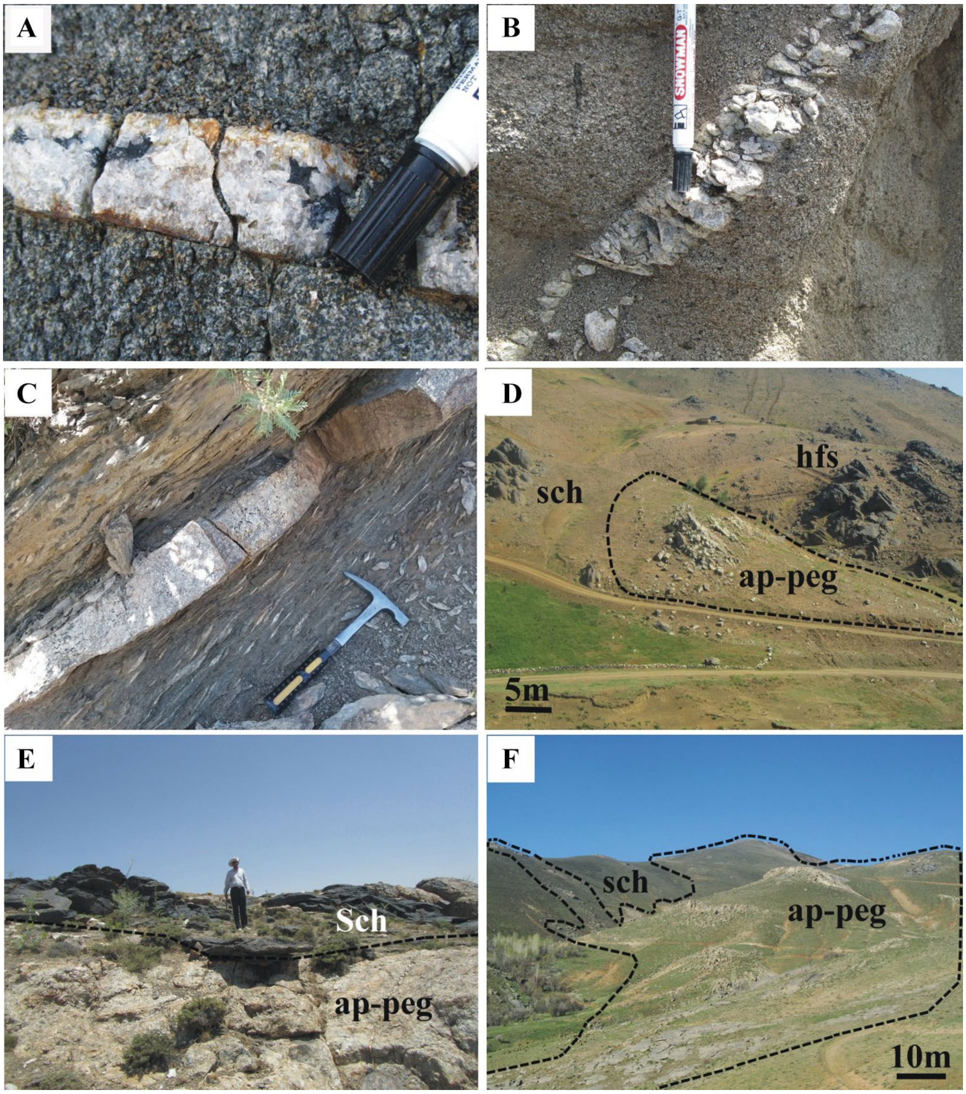

**Fig. 3** Outcrops of pegmatiticand aplitic dykes in are: **a** Tarikdarreh, southwest of Hamedan, dykes are intruded Alvandcomplex in this area. **b** Goshalan, west of Hamedan, dykes are intruded Alvand complex in these area. **c**, **d** Simin, southeast of Hamedan, dykes have intruded sillimanite schist, hornfels, and migmatite in this area. Note the sigmoid shape of andalusite porphroclasts in schists that are shear zone indicators (3**c**). **e**, **f** Mangavi, southeast of Hamedan, dykes have intruded sillimanite schist in this area

width. They usually have a pinkish appearance in outcrops in response to the high proportion of orthoclase. They commonly have a feldspar-rich wall zone and a quartz-rich core zone. These pegmatites comprise quartz, K-feldspar (orthoclase and microcline), plagioclase, muscovite, scarce biotite, tourmaline, garnet, titanite, allanite, needle-shaped apatite, and cassiterite. Biotite is very scarce in the studied aplitic and pegmatitic dykes and its crystals are commonly fine grained, except for pegmatites in this area where some coarse-grained biotite crystals occur. Sample Art19 that has been dated was collected from this area.

### *Aplite–pegmatite dykes emplaced marginal to plutonic rocks (in contact metamorphic rocks)*

In the Khaku area, southeast of Hamedan, aplitic and pegmatitic dykes crosscut hornfelsic host rocks. In some aplitic dykes tourmaline nodules with spherical and dendritic shapes are present (Fig. 4a). Some nodules have a light-colored halo that is a transitional zone between the core of nodules and their host aplites. These nodules consist of tourmaline, quartz, K-feldspar, plagioclase, and accessory amounts of muscovite. Tourmaline-feldspar and tourmaline-quartz intergrowths occur in outcrops of pegmatite dykes in southwest of Khaku (Fig. 4b). Aplitic and pegmatitic dykes from east of Khaku contain quartz, tourmaline, perthitic K-feldspar, and sapphire (blue corundum). White and colorless quartz and scarce rose quartz can be seen in these rocks. Sapphires are mostly converted to sericite and biotite along margins (Fig. 5a).

In the Heydareh-e-Poshteshahr area, aplites have anhedral granular texture and consist of quartz, K-feldspar, garnet, plagioclase, muscovite, scarce biotite, tourmaline, zircon, monazite, apatite, and Th-silicate. Some monazite crystals are coarse (up to 800 µm in diameter) (Fig. 5b). The quartz is typically white, but rose quartz also occurs

**Table 1** Common features of aplites and pegmatites from various areas of the region

| Area | Crosscutting features | Type of dyke | Mineral assemblage | Shape of outcrop | Textures | Host rock |
|---|---|---|---|---|---|---|
| Barfejin | Intruding plutonic rocks | Aplite | Quartz, K-feldspar, plagioclase, tourmaline, zircon, monazite, xenotime, apatite accessory amount of U-silicate and U-oxide | Vein | Anhedral granular | Granite and diorite |
| Artiman | | Aplite and pegmatite | Quartz, K-feldspar, plagioclase, muscovite, scarce biotite, tourmaline, garnet, titanite, allanite, needle-shaped apatite, and cassiterite | Vein, tabular | Graphic textures | Granite and diorite |
| Heydareh-e-Poshteshahr | Intruding both plutonic rocks and surrounding regional mtamorphic rocks | Aplite | Quartz, K-feldspar, garnet, plagioclase, muscovite, scarce biotite, tourmaline, zircon, monazite, apatite and Th-silicate | Tabular | Anhedral granular, skeletal textures | Porphyroid monzogranits and cordierite-hornfels |
| Khaku | | Aplite and pegmatite | Quartz, tourmaline, perthitic K-feldspar, muscovite, monazite and sapphire | Tabular | Spherical and dendritic nodules, anhedral granular, graphic textures | Granite and cordierite-hornfels |
| Mangavi | Intruding contact metamorphic rocks | Aplite and pegmatite | Quartz, K-feldspar, plagioclase, muscovite, tourmaline, garnet, monazite, xenotime | Body | Anhedral granular-1- anisotropic textures (fine-grained units, layering and graphic intergrowths). 2- interior zones with coarse grained and blocky textures | High-grade schists (sillimanite-bearing schists) |
| Kamari, Zaman-Abad and Dehno | | | Quartz, K-feldspar, plagioclase, muscovite, tourmaline, garnet, monazite, xenotime, and beryl | Tabular | 1- anisotropic textures (fine-grained units, layering and graphic intergrowths). 2- interior zones with coarse grained and blocky textures | |
| Simin | | | Quartz, K-feldspar, plagioclase, muscovite, tourmaline, garnet, zircon, monazite, xenotime, Nb-oxide | | | |

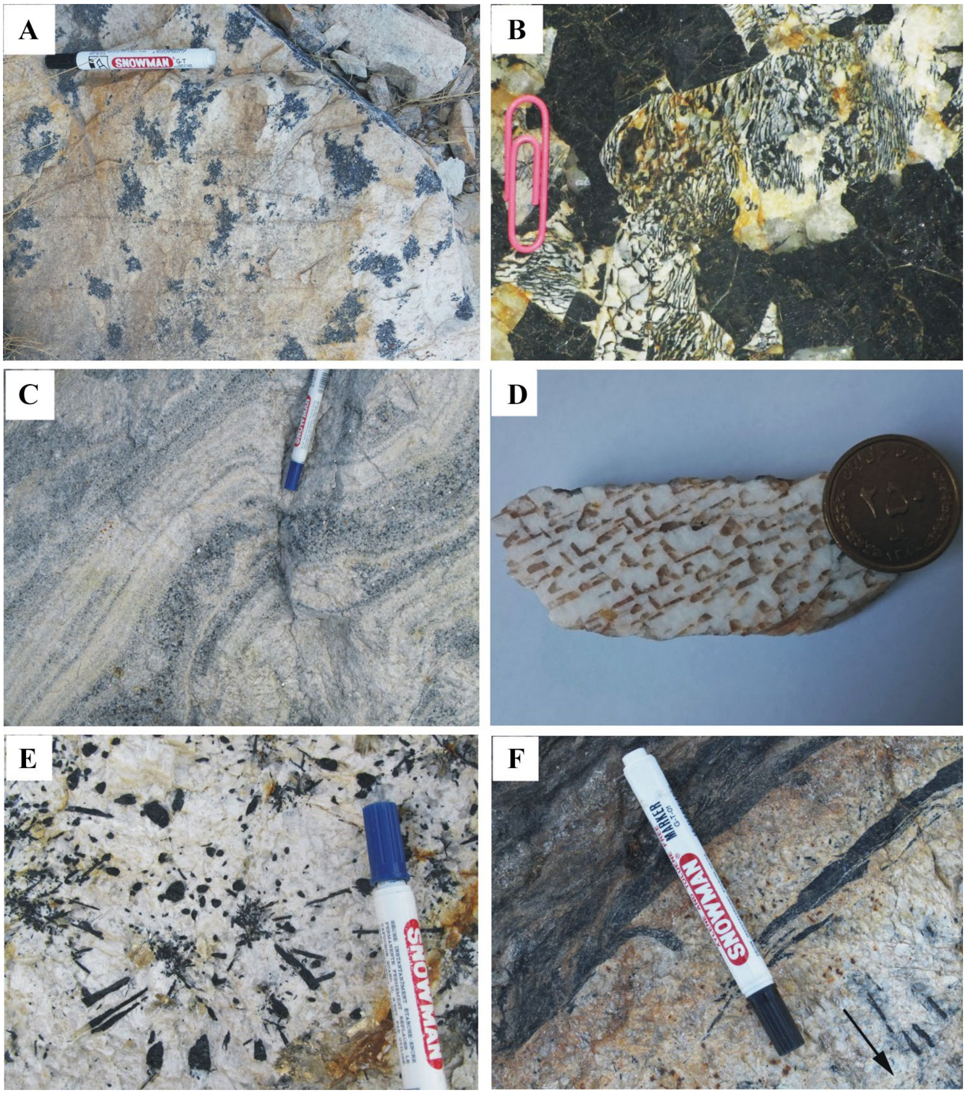

**Fig. 4** Selected sections of pegmatitic and aplitic dykes in various areas of the region; **a** Tourmaline nodules with light halo in Khaku area, south of Hamedan. **b** Tourmaline-feldspar and tourmaline-quartz intergrowths in pegmatite of Khaku area. Textures of Pegmatites in Dehnoareas, southeast of Hamedan including the following: **c** layering in tourmaline-bearing pegmatites. **d** Graphic intergrowths. **e** Radial aggregate of tourmalines. **f** Tourmalines grown perpendicular to the pegmatite margin and xenoliths of schist in contact of pegmatites. Diameter of coin is nearly 2 cm and clip's length is about 3 cm

in some dykes. Garnet occurs as translucent dark red to dark reddish brown crystals from a few millimeters to a few centimeters in diameter and is anhedral to euhedral in shape showing trapezohedron form. In some places they have skeletal shape and are intergrown with quartz possibly in response to fast growth (Fig. 5c, d). Zoned tourmalines with brown to green pleochroism are present and insome places are intergrown with quartz. Samples SNM4, SNM41, SNM42, and SNM422 were collected from this area.

### *Aplite–pegmatite dykes emplaced in regional metamorphic rocks (exterior to plutonic rocks)*

Among aplitic and pegmatitic dykes in the exterior of the Alvand complex those in Mangavi area have greater thickness (Fig. 3e, f). Several pegmatitic dykes are also distributed in the Kamari, Zaman-Abad, Dehno, and Simin areas. These dykes have complex mineralogy and textures. They commonly contain two textural domains: (1) outer zones with anisotropic textures, including fine-grained units, layering (Fig. 4c), graphic/granophyric intergrowths (Fig. 4d), and plumose aggregation; (2) interior zones with coarse-grained and blocky textures. The anisotropic textures in pegmatites are dominated by the effects of liquidus undercooling and blocky textures result mostly from the accumulation of fluxes (London 1999, 2005, 2009, 2014a, b). In layered aplitic–pegmatitic dykes, tourmaline-rich layers alternate with quartz-feldspar-rich layers across the dykes. Tourmaline locally grows as radial aggregates (Fig. 4e) or are perpendicular to the pegmatite margin (Fig. 4f) and are typically zoned prismatic crystals (Fig. 5e, f). Some tourmaline crystals have quartz, monazite, and zircon inclusions. Tourmalines have poikilitic texture (Fig. 5h) in response to very fast growth of porphyroblasts. Tourmaline crystals are color-zoned with normal (Fe-enriched cores

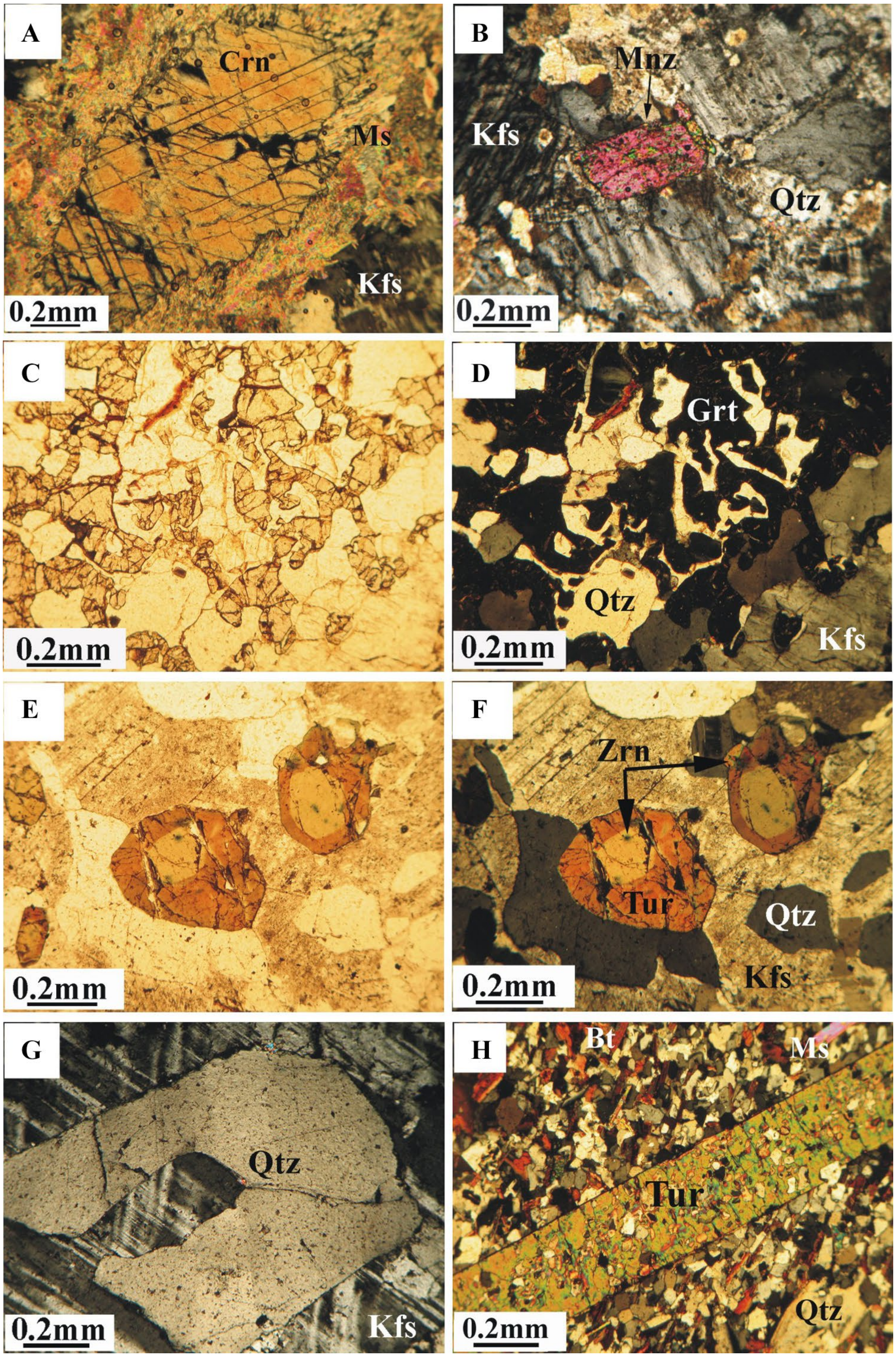

**Fig. 5** Thin section photomicrographs: **a** Existence of sapphire in aplitic and pegmatitic dykes east of Khaku that are mostly converted to sericite along margins. **b** Coarse-grained monazite in an aplitic dyke of the Heydareh-e-poshteshar area, southwest Hamedan. Skeletal shape garnet, intergrown with quartzin the same dyke, **c** in PPL, **d** in XPL. Zoned tourmaline from a layered pegmatitic dyke of the Dehno area, southeast of Hamedan, **e** in PPL, **f** in XPL. **g** Graphic texture in pegmatite dyke of Dehno area. **h** Tourmaline with poikilitic texture in schists near pegmatites in Dehno area. *Grt* Garnet, *Tur* Tourmaline, *Qtz* quartz, *Kfs* K-feldspar, *Crn* Corundum, *Ms* Muscovite, *Mnz* Monazite, and *Zrn* Zircon

relative to the rims), reverse, patchy, and oscillatory zoning represented in the tourmaline population. Pleochroism changes from light blue, pale green, yellow and light brown in the core to dark blue and dark brown in margin. In the pegmatites, graphic texture is composed of an intergrowth of microcline and quartz (Figs. 4d, 5g). Plumose muscovite clusters are seen in the wall zone of these pegmatites. Also, in host schists high amounts of tourmaline and muscovite have crystallized (exocontact metasomatism). Fine needle-shaped muscovite is seen as inclusions in quartz and feldspar in border zone and yellowish large crystalline books of muscovite are seen in wall and intermediate zones of some pegmatites. Xenoliths of schist are common in these pegmatites near the contact zone (Fig. 4f). Pegmatites in the

**Table 2** Whole rock geochemistry of pegmatite and aplite samples of the Hamedan region with ICP-MS and ICP-AES methods

| Sample | Fine grain pegmatite | | | | | Aplite | | | | | | | | | | |
|---|---|---|---|---|---|---|---|---|---|---|---|---|---|---|---|---|
| | Ba-Mo6 | Ar-4 | Ar-14 | So-3 | Pa-7 | T-5 | Ba-Mo4 | AS12.G17* | AS12.G18* | ASG1* | AS11G6* | MBG9 | MBG7 | GRT-AP | HMt6 | HH7 |
| $SiO_2$ | 69.40 | 66.60 | 69.70 | 71.80 | 71.70 | 72.50 | 72.60 | 74.50 | 73.00 | 75.60 | 76.90 | 76.40 | 75.10 | 75.20 | 73.10 | 72.60 |
| $TiO_2$ | 0.08 | 0.01 | 0.17 | 0.10 | 0.08 | 0.06 | 0.07 | 0.09 | 0.19 | 0.02 | 0.05 | 0.18 | 0.03 | 0.03 | 0.03 | 0.02 |
| $Al_2O_3$ | 13.00 | 16.00 | 15.80 | 13.30 | 13.80 | 13.60 | 12.10 | 13.25 | 14.40 | 12.90 | 14.55 | 12.75 | 13.15 | 12.85 | 15.5 | 15.0 |
| $Fe_2O_3$ | 1.18 | 0.09 | 1.62 | 1.03 | 1.00 | 1.29 | 0.90 | 0.87 | 1.47 | 1.50 | 1.06 | 1.65 | 1.44 | 1.22 | 1.03 | 0.82 |
| MgO | 0.22 | 0.02 | 0.29 | 0.19 | 0.23 | 0.10 | 0.11 | 0.14 | 0.33 | 0.08 | 0.12 | 0.22 | 0.06 | 0.10 | 0.08 | 0.38 |
| MnO | <0.01 | 0.29 | 0.04 | 0.03 | 0.02 | 0.04 | 0.01 | 0.02 | 0.03 | 0.18 | 0.02 | 0.02 | 0.05 | 0.05 | 0.09 | 0.19 |
| CaO | 0.43 | 0.53 | 0.84 | 1.04 | 1.55 | 0.49 | 0.35 | 0.60 | 1.40 | 0.42 | 0.51 | 0.76 | 0.47 | 0.31 | 0.72 | 0.85 |
| $Na_2O$ | 2.30 | 5.40 | 2.00 | 4.00 | 3.40 | 3.80 | 2.50 | 3.91 | 3.91 | 2.41 | 1.28 | 2.77 | 2.32 | 2.11 | 4.30 | 8.1 |
| $K_2O$ | 7.54 | 3.00 | 4.35 | 4.11 | 4.70 | 4.06 | 6.76 | 4.71 | 4.56 | 6.12 | 3.61 | 4.62 | 2.71 | 7.04 | 4.04 | 0.38 |
| $P_2O_5$ | 0.17 | 0.73 | 0.50 | 0.08 | 0.12 | 0.09 | 0.09 | 0.05 | 0.07 | 0.09 | 0.34 | 0.05 | 0.13 | 0.13 | 0.50 | 0.76 |
| LOI | 0.73 | 1.21 | 1.67 | 0.57 | 0.31 | 0.85 | 0.87 | 0.47 | 0.20 | 0.68 | 1.08 | 0. 50 | 0.50 | 0.40 | 1.07 | 0.46 |
| Sum | 95.0 | 95.1 | 96.9 | 96.2 | 96.9 | 96.8 | 96.4 | 98.2 | 99.1 | 99.5 | 98.1 | 99.9 | 95.9 | 99.2 | 100.4 | 99.2 |
| Rb | 211 | 590 | 936 | 205 | 101 | 257 | 197 | 162.5 | 154.5 | 156.5 | 199.0 | 163.5 | 157.5 | 185 | 527 | 47.6 |
| Cs | 5.1 | 25.1 | 152 | 7.3 | 7.0 | 24.7 | 5.4 | 3.43 | 4.47 | 8.66 | 7.93 | 7.91 | 3.86 | 4.25 | 89.53 | 2.1 |
| Th | 5.8 | 0.7 | 8.0 | 13.0 | 2.9 | 13.3 | 3.0 | 60.1 | 78.8 | 0.60 | 1.97 | 24.3 | 7.08 | 2.15 | 0.9 | 0.9 |
| U | 1.26 | 2.65 | 1.07 | 4.26 | 0.95 | 2.80 | 0.81 | 23.7 | 16.95 | 0.48 | 1.95 | 2.72 | 2.12 | 1.39 | 2.24 | 5.34 |
| Ba | 240 | 60 | 240 | 360 | 330 | 70 | 180 | 387 | 706 | 67.2 | 75.5 | 619 | 20.5 | 110.5 | 50 | <10 |
| Sr | 70 | 30 | 40 | 140 | 160 | 20 | 70 | 133.5 | 265 | 33.6 | 48.6 | 115.5 | 13.6 | 63.3 | 50 | 20 |
| Ga | 13 | 37 | 31 | 17 | 16 | 19 | 12 | 19.4 | 16.9 | 12.6 | 17.8 | 13.6 | 12.8 | 13.8 | 29 | 29 |
| Tl | <0.5 | 1.3 | 2.1 | <0.5 | <0.5 | 0.5 | <0.5 | <0.5 | <0.5 | <0.5 | <0.5 | <0.5 | <0.5 | <0.5 | 1.2 | <0.5 |
| Pb | – | – | – | – | – | – | – | 13 | 12 | 38 | 10 | 34 | 48 | 38 | – | – |
| Nb | 7 | 151 | 40 | 19 | 8 | 16 | 4 | 134.5 | 70.1 | 1.9 | 12.0 | 15 | 2.5 | 1.1 | 76 | 62 |
| Ta | 0.7 | 58.3 | 10.2 | 4.7 | 1.7 | 3.1 | <0.5 | 22.6 | 10.9 | 0.6 | 3.2 | 1.3 | 0.3 | 0.2 | 67.2 | 26.4 |
| Sn | 5 | >10,000 | 158 | 13 | 6 | 22 | 3 | 1 | 1 | 6 | 10 | 5 | 3 | 4 | 114 | 284 |
| W | <1 | 6 | 6 | 2 | 4 | 8 | <1 | 4 | 2 | 8 | 7 | 2 | 3 | 2 | 4 | 3 |
| Cu | 11 | 8 | 6 | 15 | 10 | 8 | 14 | <5 | <5 | <5 | <5 | 15 | 46 | 7 | 11 | 15 |
| Cr | – | – | – | – | – | – | – | 480 | 550 | 840 | 470 | <10 | 10 | 10 | – | – |
| Co | 3.5 | 0.5 | 2.6 | 1.3 | 3.5 | 0.9 | 1.3 | 0.9 | 2.2 | 0.9 | 0.9 | 2.4 | 1.2 | 1.0 | 0.9 | 1.1 |
| Ni | <5 | <5 | <5 | <5 | <5 | 5 | 6 | <5 | <5 | <5 | <5 | <5 | 5 | <5 | 6 | 7 |
| V | 5 | <5 | 17 | 10 | 9 | 5 | 8 | <5 | <5 | <5 | <5 | 8 | <5 | <5 | 8 | 6 |
| Y | 17.0 | 2.9 | 14.0 | 17.3 | 10.9 | 25.7 | 5.7 | 44.0 | 22.5 | 17.4 | 5.6 | 11.5 | 20.4 | 18.3 | 1.8 | 1.1 |
| Zn | 19 | 124 | 81 | 23 | 17 | 33 | 15 | 24 | 22 | 13 | 27 | 28 | 9 | 6 | 25 | 23 |
| Zr | 35.8 | 17.1 | 75.4 | 58.6 | 21.8 | 38.6 | 23.0 | 183 | 208 | 23 | 25 | 105 | 71 | 36 | 24.7 | 17.7 |
| Hf | 1 | 2 | 3 | 2 | 1 | 2 | <1 | 7.9 | 7.7 | 1.0 | 1.1 | 3.3 | 3.1 | 1.7 | 2 | 1 |
| La | 8.1 | 0.9 | 12.1 | 22.3 | 7.5 | 9.9 | 4.4 | 58.5 | 125.5 | 1.3 | 2.6 | 40.3 | 6.8 | 3.1 | 0.9 | 0.7 |

**Table 2** (continued)

| Sample | Fine grain pegmatite | | | | | Aplite | | | | | | | | | | |
|---|---|---|---|---|---|---|---|---|---|---|---|---|---|---|---|---|
| | Ba-Mo6 | Ar-4 | Ar-14 | So-3 | Pa-7 | T-5 | Ba-Mo4 | AS12.G17* | AS12.G18* | ASG1* | AS11G6* | MBG9 | MBG7 | GRT-AP | HMt6 | HH7 |
| Ce | 17.6 | 1.0 | 24.4 | 43.1 | 14.7 | 22.6 | 6.7 | 103.5 | 205 | 2.0 | 5.6 | 68.5 | 15.3 | 5.1 | 1.7 | 1.8 |
| Pr | 2.11 | 0.14 | 2.90 | 4.59 | 1.64 | 2.72 | 0.79 | 10.50 | 19.40 | 0.19 | 0.68 | 7.14 | 1.80 | 0.55 | 0.27 | 0.22 |
| Nd | 7.5 | 0.7 | 11.0 | 15.4 | 5.9 | 9.7 | 3.2 | 32.7 | 54.0 | 0.6 | 2.4 | 24.9 | 6.7 | 2.0 | 1.1 | 0.7 |
| Sm | 2.1 | 0.2 | 2.4 | 3.2 | 1.3 | 3.0 | 0.8 | 6.42 | 7.00 | 3 | 4.3 | 4.8 | 2.31 | 0.56 | 0.3 | 0.2 |
| Eu | 0.39 | 0.07 | 0.42 | 0.30 | 0.46 | 0.12 | 0.32 | 0.65 | 1.04 | 0.26 | 0.30 | 0.58 | 0.12 | 0.50 | 0.21 | 0.09 |
| Gd | 2.19 | 0.27 | 2.29 | 2.86 | 1.36 | 2.71 | 0.88 | 6.83 | 7.24 | 5.2 | 3.68 | 4.02 | 2.45 | 0.89 | 0.32 | 0.23 |
| Tb | 0.44 | 0.05 | 0.35 | 0.48 | 0.26 | 0.60 | 0.14 | 1.17 | 0.85 | 0.22 | 0.16 | 0.54 | 0.59 | 0.31 | 0.07 | <0.05 |
| Dy | 3.00 | 0.40 | 2.21 | 2.76 | 1.64 | 4.03 | 0.96 | 6.99 | 4.00 | 2.56 | 1.14 | 2.44 | 3.76 | 2.68 | 0.38 | 0.22 |
| Ho | 0.57 | <0.05 | 0.43 | 0.50 | 0.35 | 0.81 | 0.18 | 1.57 | 0.87 | 0.64 | 0.19 | 0.45 | 0.72 | 0.65 | 0.07 | <0.05 |
| Er | 1.70 | 0.22 | 1.36 | 1.42 | 1.12 | 2.41 | 0.54 | 5.33 | 2.92 | 2.63 | 0.61 | 1.29 | 1.98 | 2.03 | 0.14 | 0.08 |
| Tm | 0.20 | <0.05 | 0.18 | 0.19 | 0.14 | 0.43 | 0.07 | 0.95 | 0.49 | 0.49 | 0.90 | 0.19 | 0.27 | 0.36 | <0.05 | <0.05 |
| Yb | 1.4 | 0.1 | 1.2 | 1.3 | 1.2 | 3.0 | 0.5 | 7.04 | 3.52 | 4.31 | 0.69 | 1.27 | 1.67 | 2.50 | 0.1 | <0.1 |
| Lu | 0.18 | <0.05 | 0.18 | 0.18 | 0.17 | 0.41 | 0.08 | 1.06 | 0.56 | 0.61 | 0.09 | 0.19 | 0.22 | 0.35 | <0.05 | <0.05 |
| K/Rb | 148.26 | 21.09 | 19.28 | 83.18 | 193.06 | 65.54 | 142.36 | 120.25 | 122.45 | 162.24 | 75.26 | 117.23 | 71.38 | 157.88 | 31.8 | 33.1 |
| Rb/Sr | 3.01 | 19.66 | 23.4 | 1.46 | 0.63 | 12.58 | 2.81 | 1.21 | 0.58 | 4.65 | 4.09 | 1.41 | 11.58 | 2.92 | 10.54 | 2.38 |
| Eu/Eu* | 0.18 | 0.29 | 0.17 | 0.09 | 0.34 | 0.04 | 0.38 | 0.1 | 0.14 | 0.06 | 0.07 | 0.13 | 0.05 | 0.69 | 0.67 | 0.418 |
| A/NK | 1.08 | 1.31 | 1.97 | 1.20 | 1.29 | 1.27 | 1.05 | 1.14 | 1.26 | 1.21 | 2.41 | 1.33 | 1.94 | 1.15 | 1.35 | 1.09 |
| A/CNK | 1.02 | 1.22 | 1.65 | 1.02 | 1.02 | 1.17 | 1.00 | 1.04 | 1.03 | 1.13 | 2.09 | 1.16 | 1.72 | 1.10 | 1.21 | 0.98 |
| ∑LREE | 35.31 | 2.74 | 50.4 | 85.39 | 29.74 | 44.92 | 15.09 | 205.2 | 403.9 | 4.09 | 11.28 | 140.84 | 30.6 | 10.75 | 3.97 | 3.42 |
| ∑MREE | 8.69 | 0.99 | 8.1 | 10.1 | 5.37 | 11.27 | 3.28 | 23.63 | 21 | 11.88 | 9.77 | 12.83 | 9.95 | 5.59 | 1.35 | 0.74 |
| ∑HREE | 3.48 | 0.32 | 2.92 | 3.09 | 2.63 | 6.25 | 1.19 | 14.38 | 7.49 | 7.43 | 1.48 | 3.65 | 4.14 | 5.24 | 0.24 | 0.08 |
| ∑REE | 47.48 | 4.05 | 61.42 | 98.58 | 37.74 | 62.44 | 19.56 | 243.21 | 432.39 | 23.4 | 22.53 | 157.32 | 44.69 | 21.58 | 5.56 | 4.24 |

In some samples (i.e., Ba-Mo6, Ar14, So-3, Pa-7, T-5, and Ba-Mo4), due to existence of large amounts of tourmaline and no possibility to analyze the $B_2O_3$ amounts, the total values are low

* Data from Aliani et al. (2012). AS-12-G17, MBG-9 and Grt-AP from dykes in contact metamorphic rocks. AS11G6, MBG7 and Ar-14from dykes exterior of Alvand intrusive complex. Other samples from dykes interior to the complex

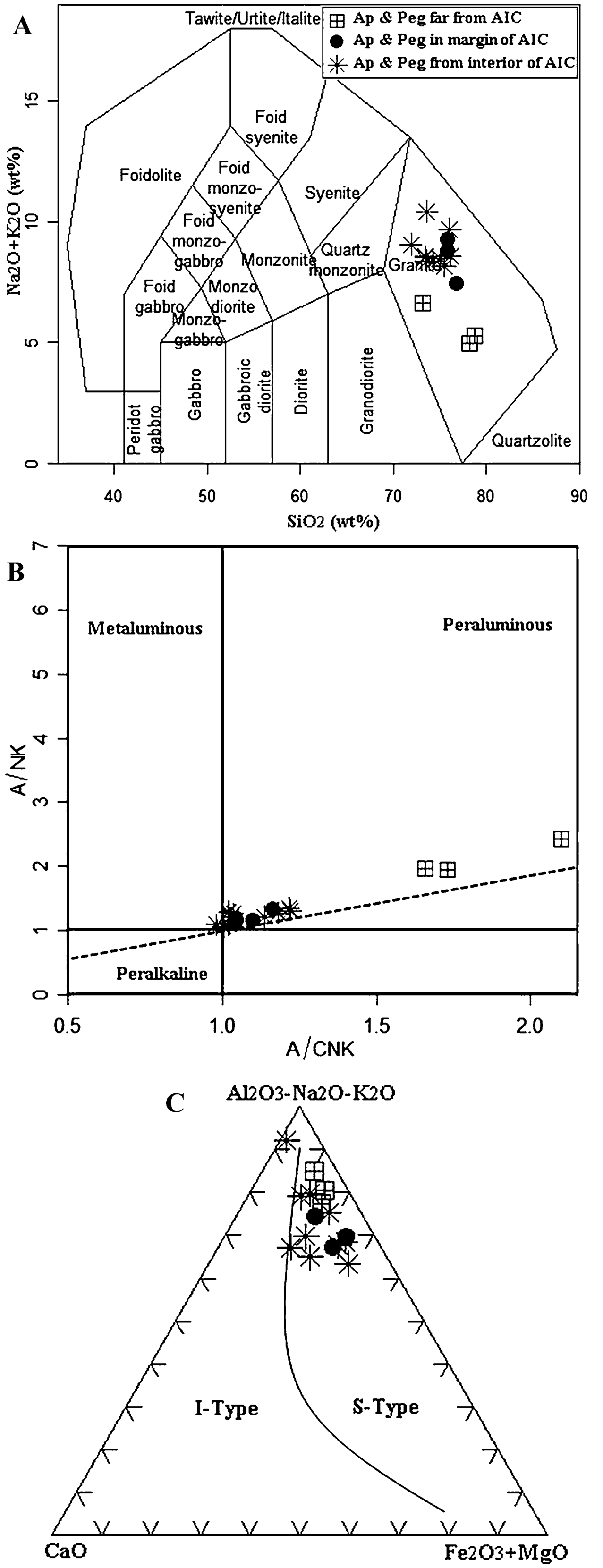

**Fig. 6** **a** TAS compositional discrimination diagram, based on classification of Middlemost (1985), **b** Plot of chemical composition of aplites and pegmatites of Hamedan region on Shand diagram, which indicates peraluminous affinity of rocks, **c** Plot of chemical composition of aplites and pegmatites of Hamedan region on diagram of Chappell and White (1992) ▸

Dehno area are comprised of quartz, K-feldspar, plagioclase, muscovite, tourmaline, garnet, and beryl. The hexagonal crystals of beryl are typically pale-green and blue (aquamarine) and up to 20 cm long. Quartz is milky, white or colorless.

K-feldspar and plagioclase occur in various aplitic and pegmatitic dykes. In general K-feldspar is more abundant than plagioclase in these rocks. K-feldspar commonly occurs as fine- to coarse-grained perthitic microcline. Zircon, monazite, xenotime, and apatite inclusions can be observed in them. It has graphic intergrowths with quartz and tourmaline in some places. In some studied pegmatites and aplites, K-feldspar is pinkish orthoclase.

## Method of study

One of the main objectives of this study was to provide constraints on the age of aplites and pegmatites in the Hamedan region using monazite, zircon, and allanite U–Pb geochronology. For this purpose, 250 samples were collected from outcrops. Seventy thin sections and 31 polished thin sections were prepared and examined with an optical microscope. Eight samples with fresh and suitable mineral assemblages were chosen for electron probe microanalysis (EPMA). The EPMA analyses were done at IMPRC Co., Karaj, Iran, using a Cameca SX 100 instrument at 15 kV voltage, $4 \times 10^{-7}$ Torr pressure, and 20 nA beam current, with maximum 30 s counting times. Ultimately, seven samples from polished thin sections were found to contain sufficiently large crystals for monazite, zircon, and allanite U–Pb laser ablation inductively coupled plasma-mass spectrometry (LAICP-MS) geochronology. For whole rock analyses, less altered and rather homogenous finer grained samples of rocks were chosen. ICP-MS and ICP-AES analyses on whole rocks were done at SGS Canada Inc., Minerals Services, Toronto, Canada.

U–Pb LA ICP-MS dating of 30 µm thick polished thin sections was done as follows: optical identification of accessory minerals by polarizing microscope was done. Then back-scattered electron (BSE) images and cathodoluminescence (CL) imaging onzircon and BSE imaging of allanite and monazite were taken. The target grains

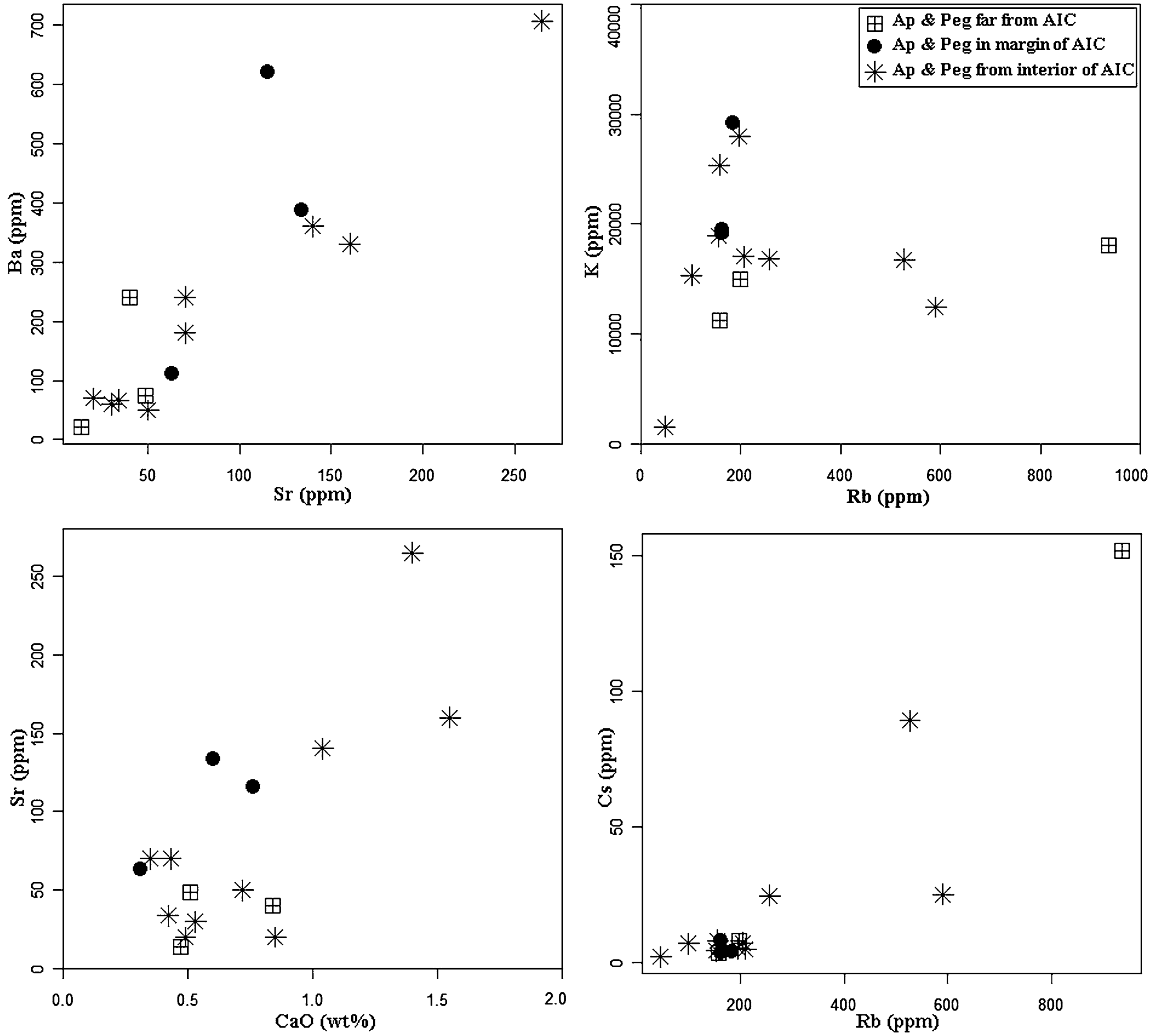

**Fig. 7** Variation diagrams of some LILE elements (see text)

were analyzed using an Australian Scientific InstrumentsM-50193 nm ArF excimer laser ablation system coupled to Agilent 7700× quadrupole ICP-MS (see McFarlane and Luo 2012). Crater diameter was 33 µm for zircon and allanite dating and 17 µm for monazite (McFarlane and McKeough 2013; McFarlane 2016). Data reduction was done by using Iolite™ and Vizual Age™. Data output and assessment of accuracy were done by using quality control standards (e.g., Plesovice zircon; 44069 monazite; SISS3 allanite). Concordia diagrams were drawn by ISOPLOT/EX 3.75 software (Ludwig 2003).

LA-ICP-MS was done on monazite, zircon, and allanite grains from five selected polished thin sections and is described as follows:

Total analyzed spots on monazite grains are 89 on 31 grains including sample Bar1; 14 spots on 11 grains, sample Bar11; 25 spots on 8 grains, sample SNM41; 17 spots on 4 grains, sample SNM42; 17 spots on 4 grains and sample SNM422; 16 spots on 4 grains. For zircon grains total analyzed spots on sample SNM4 are 9 spots on 8 grains. For allanite total analyzed spots are 25 spots on multiple grains sample Art19.

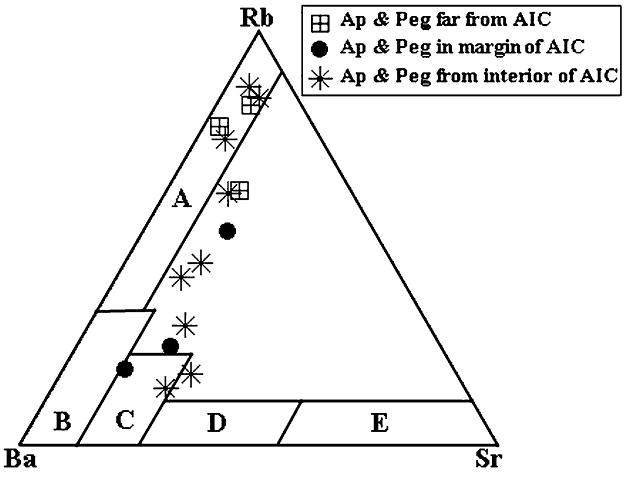

**Fig. 8** Rb–Ba–Sr ternary diagram illustrating the compositional variation of the studied aplites and pegmatites. **a** Strongly differentiated granites; **b** Normal granites; **c** Anomalous granite; **d** Quartz diorites and granodiorites; **e** Diorites (El Bouseily and El Sokkary 1975)

## Geochemistry

### Whole rock geochemistry

Whole rock analysis by fusion ICP-MS and ICP-AES has been done on 16 samples from the aplites and pegmatites of the Hamedan region (Table 2). The compositions of samples plot in the field of granite on ($Na_2O$ + $K_2O$) vs $SiO_2$ diagram of Middlemost (1985) (Fig. 6a). High amounts of $SiO_2$ (up to 76.9 wt%), $Al_2O_3$ (up to 16.0 wt%), $K_2O$ (up to 7.54 wt%), and $Na_2O$ (up to 8.10 wt%) are indicative of the importance of fractional crystallization in their petrogenesis and low amounts of CaO (0.31–1.55 wt%), $P_2O_5$ (0.05–0.76 wt%), $TiO_2$ (0.010–0.019 wt%), with $Fe_2O_{3T}$ (0.09–1.65 wt%), and MgO (0.02–0.38 wt%) and high FeOt/(FeOt + MgO) indicating a ferroan signature for these rocks (Frost et al. 2001). The latter could be related to crystallization of minerals, such as apatite, titanite, and biotite from magma in early stages of its evolution. The molar [$Al_2O_3$/(CaO + $Na_2O$ + $K_2O$)] ranges from 1.0 to 1.8 and diagrams of molar $Al_2O_3$/(CaO + $K_2O$ + $Na_2O$) versus molar $Al_2O_3$/($K_2O$ + $Na_2O$) (A/CNK vs A/NK) and molar A/CNK versus $SiO_2$ (wt%) (Shand 1943; Maniar and Piccoli 1989) reflect the peraluminous character of aplitic and pegmatitic rocks (Fig. 6b). Most pegmatites with the LCT signature have compositional affinity with S-type granites (Chappell and White 2001). On the basis of Alumina Saturation Index (ASI), these pegmatites resemble Lithium-Cesium-Tantalum (LCT) family of pegmatites (e.g., Cerný 1991; London 2008). Their A/NK values are in the range of 1.05–2.41 and A/CNK values are in the range of 1.00–2.09. These types of pegmatites are usually related to S-type granites of orogenic environments (i.e., subduction zones or continental collision zones) (Cerný 1991, 1992; Cerný and Ercit 2005; Martin and Vito 2005; Cerný et al. 2012). On the diagram from Chappell and White (1992) studied aplites and pegmatites plot in S-type granites field (Fig. 6c). A comparison of the geochemical characteristics of the studied pegmatites and aplites with geochemistry of three plutonic rock associations, which exist in the Alvand intrusive complex (see petrography section), indicates that the geochemical affinity of these rocks has similarity with the granite–granodiorite porphyry S-type assemblage (according to Sepahi 1999, 2008). Therefore, aplites and pegmatites cutting through this rock unit could be an evolved variety of granitic rocks that originated from the same magma, although those crosscutting high-grade schists and migmatites of the region may have an anatectic origin, because these pegmatites are surrounded only by sillimanite-bearing schists and migmatites in the region.

Trace element compositions of the studied rocks are presented, briefly. An increase in the amounts of Rb can be

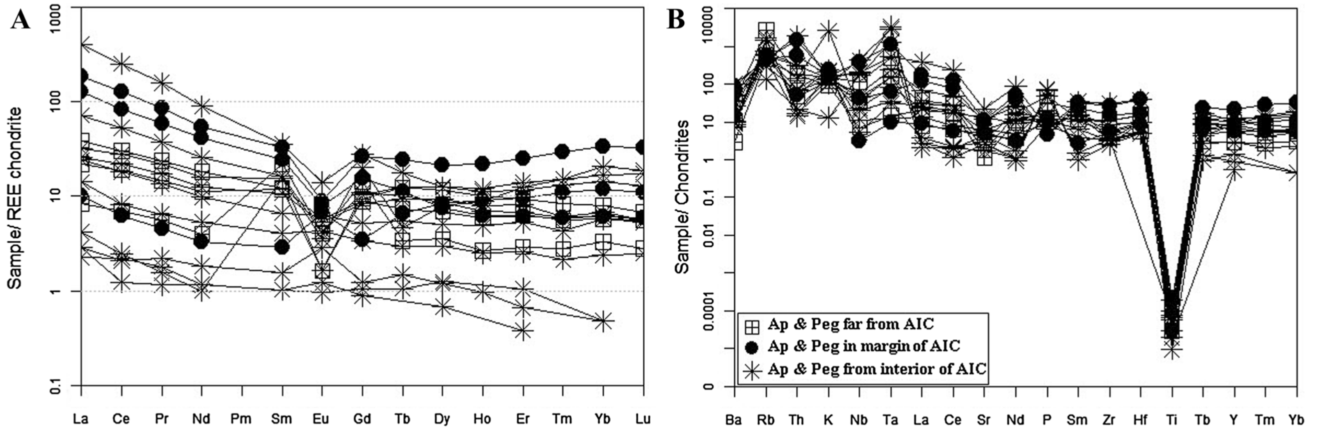

**Fig. 9** **a** Chondrite-normalized REE patterns (values from Boynton 1984) and **b** Chondrite-normalized patterns (values from Thompson 1982) in samples of aplites and pegmatites of Hamedan region

**Table 3** EPMA analyses of garnets of the Hamedan region

| Sample oxides | SNM4-1 | SNM4-2 | SNM4-3 | Kh2A72 | Kh2A73 | Mirz1 | Mirz2 | Mirz4 | SepP |
|---|---|---|---|---|---|---|---|---|---|
| Major elements (wt%) | | | | | | | | | |
| $SiO_2$ | 41.37 | 40.67 | 39.59 | 44.00 | 42.54 | 43.00 | 41.60 | 40.68 | 35.84 |
| $TiO_2$ | 0.00 | 0.00 | 0.00 | 0.00 | 0.00 | 0.01 | 0.15 | 0.18 | 0.16 |
| $Al_2O_3$ | 19.05 | 19.32 | 18.28 | 19.50 | 19.54 | 18.9 | 18.8 | 10.48 | 20.63 |
| FeO | 33.12 | 32.77 | 35.06 | 26.40 | 30.46 | 28.00 | 31.5 | 36.45 | 35.88 |
| MgO | 0.76 | 1.98 | 1.86 | 1.44 | 1.24 | 1.35 | 0.57 | 0.29 | 0.81 |
| MnO | 3.86 | 3.63 | 3.83 | 6.98 | 5.01 | 8.13 | 8.33 | 10.01 | 5.13 |
| CaO | 1.18 | 1.42 | 1.32 | 1.70 | 1.06 | 1.07 | 0.78 | 0.94 | 0.37 |
| Total | 99.34 | 99.79 | 99.94 | 100.0 | 99.85 | 101.0 | 102.0 | 99.03 | 98.82 |
| Number of cations on the basis of 12 oxygens | | | | | | | | | |
| Si | 3.31 | 3.24 | 3.20 | 3.42 | 3.35 | 3.38 | 3.29 | 3.45 | 2.98 |
| Ti | 0.00 | 0.00 | 0.00 | 0.00 | 0.00 | 0.00 | 0.01 | 0.01 | 0.01 |
| Al | 1.79 | 1.81 | 1.74 | 1.78 | 1.81 | 1.75 | 1.75 | 1.04 | 2.02 |
| Fe | 2.22 | 2.18 | 2.37 | 1.71 | 2.00 | 1.84 | 2.08 | 2.58 | 2.49 |
| Mn | 0.26 | 0.24 | 0.26 | 0.46 | 0.33 | 0.54 | 0.56 | 0.72 | 0.361 |
| Mg | 0.09 | 0.23 | 0.22 | 0.17 | 0.14 | 0.16 | 0.07 | 0.04 | 0.10 |
| Ca | 0.10 | 0.12 | 0.11 | 0.14 | 0.08 | 0.09 | 0.07 | 0.15 | 0.03 |
| Total | 7.78 | 7.84 | 7.92 | 7.69 | 7.74 | 7.79 | 7.82 | 8.01 | 7.99 |
| Fe/(Mn + Fe + Mg) | 0.86 | 0.82 | 0.83 | 0.73 | 0.80 | 0.72 | 0.76 | 0.77 | 0.84 |
| Alm (%) | 83.01 | 78.44 | 82.98 | 69.1 | 77.91 | 70.00 | 75.10 | 73.93 | 83.46 |
| Sps (%) | 9.80 | 8.79 | 9.19 | 18.5 | 12.96 | 20.60 | 20.10 | 20.57 | 12.08 |
| Grs (%) | 3.80 | 4.34 | 3.98 | 5.72 | 3.45 | 3.42 | 2.38 | 4.43 | 1.10 |
| Prp (%) | 3.39 | 8.43 | 3.85 | 6.74 | 5.68 | 6.03 | 4.80 | 1.07 | 3.36 |

correlated with late stage crystallization of K-feldspar and biotite, and decrease in Sr contents can be due to fractional crystallization of plagioclase. Barium content is commonly used as indicator of the evolution in granites and pegmatites, which decreases with increasing crystal fractionation (Cerný et al. 1985; Alfonso et al. 2003), and the decrease in content of Ba is marked. High amount of Ba (<10–706 ppm) is due to the presence of minerals, such as K-feldspar and biotite. Rubidium contents in the pegmatites and aplites vary from 48 to 936 ppm and Sr contents from 14 to 265 ppm. With increasing concentrations of K, the Rb contents of the rocks increase, as well. This positive correlation also occurs in Ba versus Sr values, CaO versus Sr values, and Cs versus Rb values, due to their similar geochemical behavior (Fig. 7). These chemical characteristics indicate that the studied aplites and pegmatites are highly evolved varieties of granitoids of the region. As a rare alkali metal Rb is enriched in K-bearing minerals during progress of pegmatite crystallization (Cerný et al. 1985), the ratio of K/Rb is indicative of the general fractionation.

A few samples contain progressively less Sr and Ba and more Rb as a result of fractionation. High amounts of Rb (48–936 ppm) in the studied aplites and pegmatites, especially in samples: Ar-14 (936 ppm), Ar-4 (590 ppm), MBG7 (158 ppm), T-5 (257 ppm), and HMt6 (526 ppm) indicate that these samples are placed in the category of strongly differentiated granites in the ternary Rb–Ba–Sr plot (El Bouseily and El Sokkary 1975). Other samples are moderately evolved chemically (Fig. 8).

On a chondrite-normalized spider diagram (Boynton 1984), the La/Lu ratio increases with increasing $\sum$REE content and profiles are virtually flat at very low concentrations of REE (Fig. 9a). $\sum$REE in the studied samples vary from 4.05 to 432 ppm and Eu/Eu* 0.04 to 0.37. LREE show enrichment against HREE. The enrichment of amounts of LREE (2.74–403.9 ppm) compared with HREE (0.08–14.38 ppm) correlates with monazite and allanite, which host the LREE in these rocks (Deer et al. 1982). Europium negative anomalies typically indicate residual plagioclase in the source region or fractional crystallization of plagioclase from magma (Henderson 1984). This anomaly is concordant with Ba and Sr anomalies in Fig. 9b.

On chondrite-normalized multi-element diagrams (Thompson 1982), high field strength elements (HFSE), such as Zr, Nb, and Ti show negative anomalies (Fig. 9b). These anomalies may result from the preservation of such elements in residual phases when magmas have been generated in a subduction zone by partial melting of source

**Table 4** EPMA analyses of tourmalines of the Hamedan region

| Sample oxides | 1/Kh | 2/Kh | 3/Kh | 4/Kh | 5/Kh | 1/Sep | 2/Sep | 3/Sep | 4/Sep | 5/Sep | 6/Sep | 7/Sep | 8/Sep | 9/Sep | 10/Sep | 9/MT | 10/MT | 11/MT | 8/AR | 9/AR | 10/AR | 7/Ar18 | 8/Ar18 | 9/Ar18 | 11/Ar18 | 12/Ar18 | 13/Ar18 | 14/Ar18 | 15/Ar18 |
|---|---|---|---|---|---|---|---|---|---|---|---|---|---|---|---|---|---|---|---|---|---|---|---|---|---|---|---|---|---|
| Major elements (wt%) | | | | | | | | | | | | | | | | | | | | | | | | | | | | | |
| $SiO_2$ | 35.4 | 35.98 | 35.64 | 35.75 | 36.08 | 37.39 | 36.32 | 36.12 | 36.15 | 35.96 | 35.32 | 36.12 | 35.99 | 35.62 | 35.07 | 36.37 | 36.38 | 36.33 | 36.59 | 36.25 | 35.66 | 35.6 | 36.47 | 36.2 | 36.53 | 36.45 | 36.27 | 36.76 | 36.35 |
| $TiO_2$ | 0.74 | 0.94 | 0 | 1.29 | 0.5 | 0.4 | 1 | 0.78 | 0.97 | 0.96 | 0.87 | 0.35 | 0.89 | 0.89 | 0.63 | 0.38 | 0.38 | 0.43 | 0.05 | 0.05 | 0.21 | 0.97 | 1.5 | 1.42 | 0.39 | 0.42 | 0.78 | 0.77 | 0.38 |
| $Al_2O_3$ | 30.05 | 30.44 | 31.9 | 30.4 | 30.54 | 38.04 | 37.03 | 36.84 | 37.06 | 37.09 | 36.57 | 36.88 | 36.98 | 36.65 | 36.77 | 34.68 | 34.32 | 35.04 | 35.5 | 35.25 | 35.3 | 32.9 | 32.04 | 32.5 | 34.25 | 33.84 | 34.15 | 35.03 | 34.33 |
| FeO | 17.56 | 16.78 | 16.3 | 16.79 | 16.7 | 12.88 | 14.33 | 14.34 | 14.12 | 13.3 | 13.41 | 13.08 | 13.45 | 13.35 | 13.17 | 12.58 | 12.52 | 12.54 | 13.2 | 13.09 | 12.6 | 11.79 | 11.92 | 11.85 | 11.88 | 11.5 | 10.62 | 9.93 | 11.74 |
| MgO | 1.05 | 0.98 | 1.04 | 0.99 | 0.96 | 0.52 | 0.54 | 0.65 | 0.62 | 0.78 | 0.78 | 0.5 | 0.62 | 0.67 | 0.84 | 1.39 | 1.35 | 1.4 | 0.04 | 0.01 | 0.06 | 2.56 | 2.54 | 2.45 | 2.2 | 1.96 | 1.67 | 1.61 | 1.71 |
| MnO | 0.78 | 0.82 | 0.84 | 0.89 | 0.86 | 0.23 | 0.16 | 0.17 | 0.03 | 0.02 | 0.16 | 0.17 | 0.16 | 0.17 | 0.15 | 0.12 | 0.15 | 0.16 | 0.44 | 0.42 | 0.44 | 0.19 | 0.19 | 0.35 | 0.3 | 0.34 | 0.5 | 0.62 | 0.49 |
| CaO | 0.22 | 0.22 | 0.14 | 0.16 | 0.11 | 0.09 | 0.26 | 0.34 | 0.24 | 0.26 | 0.28 | 0.09 | 0.22 | 0.27 | 0.28 | 0.11 | 0.1 | 0.1 | 0.01 | 0.02 | 0.07 | 0.31 | 0.26 | 0.09 | 0.15 | 0.36 | 0.05 | 0.06 | 0.05 |
| $Na_2O$ | 0 | 1.68 | 2.91 | 2.82 | 2.81 | 1.32 | 1.67 | 1.97 | 1.89 | 1.96 | 1.91 | 1.61 | 1.88 | 1.58 | 1.71 | 1.69 | 1.66 | 1.69 | 1.36 | 1.45 | 1.87 | 2.21 | 2.22 | 2.38 | 2.01 | 1.9 | 2.13 | 2.26 | 2.11 |
| $K_2O$ | 0.08 | 0.07 | 0.07 | 0.08 | 0.08 | 0.04 | 0.05 | 0.06 | 0.04 | 0.06 | 0.05 | 0.05 | 0.05 | 0.07 | 0.08 | 0.05 | 0.05 | 0.07 | 0.04 | 0.05 | 0.05 | 0.12 | 0.05 | 0.05 | 0.05 | 0.28 | 0.06 | 0.07 | 0.04 |
| Total | 85.88 | 87.91 | 88.84 | 89.17 | 88.64 | 90.91 | 91.36 | 91.27 | 91.12 | 90.39 | 89.35 | 88.85 | 90.24 | 89.27 | 88.7 | 87.37 | 86.91 | 87.76 | 87.23 | 86.59 | 86.26 | 86.65 | 87.19 | 87.29 | 87.76 | 87.05 | 86.23 | 87.11 | 87.2 |
| Number of cations on the basis of 31 oxygens | | | | | | | | | | | | | | | | | | | | | | | | | | | | | |
| Si | 6.233 | 6.209 | 6.095 | 6.12 | 6.201 | 6.019 | 5.896 | 5.884 | 5.876 | 5.873 | 5.85 | 5.975 | 5.89 | 5.887 | 5.838 | 6.112 | 6.149 | 6.086 | 6.162 | 6.149 | 6.082 | 6.062 | 6.172 | 6.118 | 6.108 | 6.153 | 6.138 | 6.139 | 6.124 |
| Ti | 0.097 | 0.122 | 0 | 0.166 | 0.064 | 0.044 | 0.122 | 0.095 | 0.118 | 0.117 | 0.108 | 0.04 | 0.109 | 0.11 | 0.079 | 0.044 | 0.044 | 0.0497 | 0.006 | 0.006 | 0.025 | 0.124 | 0.19 | 0.18 | 0.045 | 0.053 | 0.099 | 0.097 | 0.044 |
| Al | 6.247 | 6.185 | 6.43 | 6.134 | 6.179 | 7.21 | 7.081 | 7.067 | 7.109 | 7.142 | 7.145 | 7.195 | 7.133 | 7.149 | 7.221 | 6.874 | 6.833 | 6.91 | 7.047 | 7.058 | 7.097 | 6.603 | 6.383 | 6.474 | 6.761 | 6.724 | 6.823 | 6.89 | 6.812 |
| Fe | 2.028 | 1.897 | 1.824 | 1.882 | 1.879 | 1.359 | 1.519 | 1.524 | 1.499 | 1.422 | 1.452 | 1.418 | 1.446 | 1.449 | 1.438 | 1.386 | 1.383 | 1.37 | 1.455 | 1.455 | 1.407 | 1.315 | 1.317 | 1.316 | 1.301 | 1.27 | 1.174 | 1.085 | 1.29 |
| Mg | 0.215 | 0.197 | 0.19 | 0.181 | 0.192 | 0.097 | 0.102 | 0.123 | 0.117 | 0.148 | 0.15 | 0.096 | 0.118 | 0.129 | 0.163 | 0.272 | 0.266 | 0.273 | 0.007 | 0.001 | 0.01 | 0.508 | 0.501 | 0.483 | 0.434 | 0.385 | 0.329 | 0.313 | 0.336 |
| Mn | 0.116 | 0.119 | 0.121 | 0.129 | 0.125 | 0.031 | 0.022 | 0.023 | 0.041 | 0.003 | 0.206 | 0.023 | 0.022 | 0.023 | 0.021 | 0.017 | 0.021 | 0.022 | 0.062 | 0.06 | 0.063 | 0.027 | 0.027 | 0.05 | 0.042 | 0.048 | 0.071 | 0.087 | 0.069 |
| Ca | 0.032 | 0.031 | 0.019 | 0.022 | 0.016 | 0.011 | 0.034 | 0.046 | 0.032 | 0.035 | 0.039 | 0.011 | 0.03 | 0.037 | 0.039 | 0.015 | 0.014 | 0.014 | 0.001 | 0.003 | 0.009 | 0.044 | 0.037 | 0.013 | 0.021 | 0.05 | 0.007 | 0.008 | 0.007 |
| Na | 0 | 0.44 | 0.755 | 0.732 | 0.732 | 0.322 | 0.412 | 0.487 | 0.466 | 0.486 | 0.479 | 0.404 | 0.466 | 0.396 | 0.396 | 0.431 | 0.426 | 0.429 | 0.347 | 0.372 | 0.483 | 0.571 | 0.57 | 0.61 | 0.51 | 0.486 | 0.547 | 0.572 | 0.539 |
| K | 0.014 | 0.011 | 0.011 | 0.013 | 0.014 | 0.006 | 0.008 | 0.009 | 0.006 | 0.009 | 0.008 | 0.008 | 0.008 | 0.011 | 0.013 | 0.008 | 0.008 | 0.011 | 0.006 | 0.008 | 0.008 | 0.02 | 0.008 | 0.008 | 0.008 | 0.047 | 0.01 | 0.011 | 0.006 |
| Total | 15.62 | 15.93 | 16.25 | 16.19 | 16.19 | 15.61 | 15.78 | 15.87 | 15.82 | 15.82 | 15.85 | 15.72 | 15.81 | 15.76 | 15.83 | 15.85 | 15.73 | 15.755 | 15.6 | 15.63 | 15.73 | 15.96 | 15.88 | 15.93 | 15.86 | 15.843 | 15.775 | 15.76 | 15.84 |

**Table 5** EPMA analyses of K-feldspars of the Hamedan region

| Sample | 1. Kh | 2. Kh | 1. Sep | 2. Sep | 3. Sep | 4. Sep | 1. Ar4 | 2. Ar4 | 3. Ar4 | 4. Ar4 | 5. Ar4 | 6. Ar4 | 1. T5 | 2. T5 |
|---|---|---|---|---|---|---|---|---|---|---|---|---|---|---|
| $SiO_2$ | 64.34 | 64.47 | 64.35 | 65.05 | 65.08 | 65.05 | 64.24 | 64.01 | 64.33 | 64.21 | 64.06 | 64.14 | 65.16 | 65.2 |
| $TiO_2$ | 0.00 | 0.00 | 0.00 | 0.00 | 0.00 | 0.00 | 0.00 | 0.02 | 0.00 | 0.00 | 0.03 | 0.01 | 0.00 | 0.00 |
| $Al_2O_3$ | 18.39 | 18.51 | 19.07 | 18.59 | 18.22 | 18.92 | 18.34 | 18.43 | 18.31 | 18.44 | 18.39 | 18.48 | 18.23 | 18.25 |
| FeO | 0.07 | 0.12 | 0.00 | 0.00 | 0.00 | 0.00 | 0.00 | 0.00 | 0.00 | 0.00 | 0.00 | 0.00 | 0.11 | 0.00 |
| MnO | 0.00 | 0.01 | 0.00 | 0.01 | 0.00 | 0.01 | 0.00 | 0.00 | 0.00 | 0.01 | 0.01 | 0.00 | 0.00 | 0.00 |
| MgO | 0.00 | 0.00 | 0.00 | 0.00 | 0.00 | 0.00 | 0.01 | 0.01 | 0.00 | 0.00 | 0.01 | 0.00 | 0.00 | 0.01 |
| CaO | 0.00 | 0.00 | 0.02 | 0.03 | 0.00 | 0.02 | 0.01 | 0.00 | 0.00 | 0.00 | 0.01 | 0.00 | 0.01 | 0.00 |
| $Na_2O$ | 0.84 | 0.39 | 1.24 | 1.02 | 0.99 | 0.00 | 0.30 | 0.49 | 0.81 | 0.62 | 0.87 | 0.63 | 0.91 | 0.91 |
| $K_2O$ | 17.21 | 17.11 | 16.09 | 16.15 | 16.50 | 16.61 | 17.80 | 17.48 | 17.30 | 17.64 | 17.14 | 17.49 | 16.40 | 17.09 |
| Total | 100.85 | 100.61 | 100.77 | 100.85 | 100.79 | 100.61 | 100.70 | 100.44 | 100.75 | 100.92 | 100.52 | 100.80 | 100.80 | 101.46 |
| Number of cations on the basis of 8 oxygens | | | | | | | | | | | | | | |
| Si | 2.974 | 2.98 | 2.96 | 2.986 | 2.995 | 2.988 | 2.978 | 2.972 | 2.977 | 2.971 | 2.971 | 2.971 | 2.996 | 2.99 |
| Ti | 0 | 0 | 0 | 0 | 0 | 0 | 0 | 0.001 | 0 | 0 | 0.001 | 0 | 0 | 0 |
| Al | 1.002 | 1.009 | 1.034 | 1.006 | 0.988 | 1.024 | 1.002 | 1.009 | 0.999 | 1.006 | 1.005 | 1.009 | 0.988 | 0.986 |
| Fe | 0.003 | 0.005 | 0 | 0 | 0 | 0 | 0 | 0 | 0 | 0 | 0 | 0 | 0.004 | 0 |
| Mn | 0 | 0 | 0 | 0 | 0 | 0 | 0 | 0 | 0 | 0 | 0 | 0 | 0 | 0 |
| Mg | 0 | 0 | 0 | 0 | 0 | 0 | 0.001 | 0.001 | 0 | 0 | 0.001 | 0 | 0 | 0.001 |
| Ca | 0 | 0 | 0.001 | 0.001 | 0 | 0.001 | 0 | 0 | 0 | 0 | 0 | 0 | 0 | 0 |
| Na | 0.075 | 0.035 | 0.111 | 0.091 | 0.088 | 0 | 0.027 | 0.044 | 0.073 | 0.056 | 0.078 | 0.057 | 0.081 | 0.081 |
| K | 1.015 | 1.009 | 0.944 | 0.964 | 0.969 | 0.973 | 1.053 | 1.035 | 1.021 | 1.041 | 1.014 | 1.033 | 0.962 | 1 |
| Sum | 5.07 | 5.038 | 5.05 | 5.03 | 5.04 | 4.987 | 5.061 | 5.062 | 5.07 | 5.074 | 5.071 | 5.07 | 5.032 | 5.057 |

rocks, which is then recorded to some extent in all derivative crustal and supracrustal rocks (see Wedepohl 1995). Titanium negative anomalies may be related to fractional crystallization of titanite and ilmenite and other Ti-bearing phases like magnetite, clinopyroxene, hornblende, biotite, and even muscovite from evolving magmas. Positive anomalies of K and Rb in multi-elements spider diagram (Fig. 9b) may have resulted from late stage crystallization of muscovite and K-feldspar from magma. Barium, and Sr negative anomalies can be due to their co-substitution in plagioclase, which crystallizes at early stages (Fig. 9b). Positive P anomalies may be related to the presence of apatite in the rocks although P can remain incompatible in melts with high A/CNK and substitute into feldspar, although this has not been ascertained. On the whole, enrichment in some LILE, such as K, Rb, and Th and depletion in some HFSE, such as Nb, Ti, Zr, and Y, and HREE can be related to melting and fractionation processes in the region (Foley and Wheller 1990; Wilson 2007).

According to Linnen et al. (2012), the LCT (Li- Cs- Ta) family of pegmatites contains high concentrations of Rb, Cs, Be, Ta, Nb, and Sn, as well as elevated levels of fluxing components (Li, P, F, and B). Accordingly the studied aplite and pegmatites have high concentration of Rb (up to 936 ppm), Cs (up to 152 ppm), Ta (up to 67.2 ppm), Nb (up to 151 ppm), and Sn (>10,000 ppm). High amounts of Sn (to greater than 10,000 ppm/1%) are consistent with crystallization of cassiterite as accessory phase in some of these rocks. High amounts of HFSE elements, such as Th (up to 78.8 ppm), U (up to 23.7 ppm), and Zr (up to 208 ppm) (Table 2), are consistent with occurrence of some minerals, such as Th-silicate, U-silicate, U-oxides, and zircon in these rocks. High amounts of some REE and HFSE elements, such as Ce (up to 103.5 ppm), La (up to 125), Nb (up to 135), Ta (up to 67.2), and LILE elements, such as Cs (up to 152 ppm) (Table 2), K/Rb (19.3–193.1), and Rb/Sr (0.58–23.4) ratios and occurrence of some accessory minerals, such as Th-silicate, U-silicate, U-oxides, Nb-oxide, zircon, allanite, phosphate minerals (monazite, xenotime and apatite), beryl, and cassiterite emphasize the highly fractionated nature of some of these studied aplites and pegmatites.

## Mineral chemistry

In this section, mineral chemistry of common minerals of the pegmatites and aplites of the region, such as garnet, tourmaline, K-feldspar, plagioclase, muscovite, and biotite are presented to interpret crystallization and fractionation history of these rocks (Tables 3, 4, 5, 6, 7, 8).

**Table 6** EPMA analyses of plagioclases of the Hamedan region

| Sample | 1. Kh | 2. Kh | 1. Sep | 2. Sep | 3. Sep | 4. Sep | 1. Mt5 | 2. Mt5 | 3. Mt5 | 4. Mt5 | 5. Mt5 | 1. Ar4 | 2. Ar4 | 3. Ar4 |
|---|---|---|---|---|---|---|---|---|---|---|---|---|---|---|
| $SiO_2$ | 67.12 | 67.19 | 66.94 | 66.27 | 67.44 | 67.58 | 67.93 | 67.82 | 66.26 | 66.65 | 65.72 | 67.20 | 67.7 | 67.43 |
| $TiO_2$ | 0.00 | 0.00 | 0.00 | 0.00 | 0.00 | 0.00 | 0.01 | 0.00 | 0.01 | 0.00 | 0.03 | 0.03 | 0.02 | 0.00 |
| $Al_2O_3$ | 20.06 | 20.21 | 20.66 | 21.28 | 20.69 | 20.26 | 20.29 | 20.30 | 21.13 | 21.16 | 22.09 | 20.13 | 20.08 | 19.93 |
| FeO | 0.20 | 0.27 | 0.03 | 0.00 | 0.00 | 0.00 | 0.00 | 0.00 | 0.00 | 0.00 | 0.06 | 0.02 | 0.02 | 0.00 |
| MnO | 0.00 | 0.02 | 0.01 | 0.00 | 0.00 | 0.01 | 0.01 | 0.00 | 0.00 | 0.02 | 0.01 | 0.00 | 0.02 | 0.02 |
| MgO | 0.00 | 0.00 | 0.03 | 0.00 | 0.01 | 0.02 | 0.00 | 0.00 | 0.01 | 0.00 | 0.01 | 0.00 | 0.00 | 0.01 |
| CaO | 0.41 | 0.12 | 0.19 | 0.17 | 0.55 | 0.19 | 0.40 | 0.27 | 1.61 | 1.56 | 0.70 | 0.06 | 0.04 | 0.06 |
| $Na_2O$ | 12.02 | 13.08 | 12.01 | 12.21 | 11.93 | 11.43 | 11.17 | 11.03 | 11.36 | 11.20 | 10.02 | 11.49 | 11.09 | 11.77 |
| $K_2O$ | 0.13 | 0.09 | 0.11 | 0.10 | 0.09 | 0.07 | 0.15 | 0.12 | 0.27 | 0.25 | 1.85 | 0.16 | 0.09 | 0.12 |
| Total | 99.94 | 101.20 | 99.98 | 100.00 | 100.70 | 99.56 | 99.96 | 99.54 | 100.70 | 100.80 | 100.50 | 99.09 | 99.06 | 99.34 |
| Number of cations on the basis of 8 oxygens | | | | | | | | | | | | | | |
| Si | 2.95 | 2.934 | 2.936 | 2.909 | 2.937 | 2.965 | 2.968 | 2.971 | 2.899 | 2.907 | 2.885 | 2.964 | 2.979 | 2.969 |
| Ti | 0 | 0 | 0 | 0 | 0 | 0 | 0 | 0 | 0 | 0 | 0.001 | 0.001 | 0.001 | 0 |
| Al | 1.039 | 1.04 | 1.068 | 1.101 | 1.062 | 1.048 | 1.045 | 1.048 | 1.09 | 1.088 | 1.143 | 1.047 | 1.041 | 1.034 |
| Fe | 0.007 | 0.01 | 0.001 | 0 | 0 | 0 | 0 | 0 | 0 | 0 | 0.002 | 0.001 | 0.001 | 0 |
| Mn | 0 | 0.001 | 0 | 0 | 0 | 0 | 0 | 0 | 0 | 0.001 | 0 | 0 | 0.001 | 0.001 |
| Mg | 0 | 0 | 0.002 | 0 | 0.001 | 0.001 | 0 | 0 | 0.001 | 0 | 0.001 | 0 | 0 | 0.001 |
| Na | 1.024 | 1.107 | 1.021 | 1.039 | 1.007 | 0.972 | 0.946 | 0.937 | 0.964 | 0.947 | 0.853 | 0.983 | 0.946 | 1.005 |
| K | 0.006 | 0.005 | 0.006 | 0.006 | 0.005 | 0.004 | 0.008 | 0.007 | 0.015 | 0.014 | 0.104 | 0.009 | 0.005 | 0.007 |
| Ca | 0.019 | 0.006 | 0.009 | 0.008 | 0.026 | 0.009 | 0.019 | 0.013 | 0.075 | 0.073 | 0.033 | 0.003 | 0.002 | 0.003 |
| Sum | 5.045 | 5.102 | 5.044 | 5.063 | 5.038 | 4.999 | 4.987 | 4.976 | 5.045 | 5.03 | 5.021 | 5.007 | 4.975 | 5.019 |
| Ab% | 97.61 | 99.01 | 98.55 | 98.67 | 97.01 | 98.68 | 97.22 | 97.91 | 91.46 | 91.58 | 86.16 | 98.79 | 99.26 | 99.01 |
| Or% | 0.57 | 0.44 | 0.57 | 0.56 | 0.48 | 0.40 | 0.82 | 0.73 | 1.42 | 1.35 | 10.5 | 0.90 | 0.52 | 0.68 |
| An% | 1.82 | 0.55 | 0.88 | 0.77 | 2.51 | 0.92 | 1.96 | 1.36 | 7.12 | 7.07 | 3.34 | 0.31 | 0.22 | 0.31 |

### *Garnet*

The chemical analyses of garnet crystals from aplitic rocks of the Hamedan region show that they are almandine-rich garnets ($X_{Alm}$ = 69.1–83.5), but contain notable amounts of spessartine, as well ($X_{Sps}$ = 8.79–20.60) (Table 3; Fig. 10) that illustrate accumulation of Mn at late stages of crystallization (Cerný et al. 1985). Fe/(Fe + Mn + Mg) values (0.72–0.86) of these garnets also illustrate their almandine-rich nature. The mole fractions of Ca and Ti are negligible.

### *Tourmaline*

The chemical analyses of tourmaline crystals are shown in Table 4. These tourmalines have FeO (9.93–17.56 wt%), MgO (0.01–2.56 wt%), MnO (0.02–0.89 wt%), CaO (0.01–0.31 wt%), $Na_2O$ (<0.01–2.91 wt%), and $K_2O$ (0.04–0.28 wt%). The chemistry of tourmaline is consistent with its zoned texture in photomicrographs. In all studied samples, Na is dominant over Ca and K, at the X site. The Ca contents are low with the range from 0.001 to 0.05 apfu; accordingly on Ca-(X site vacancy)-(Na + K) diagram most studied tourmalines plot in the alkali field (Hawthorne and Henry 1999) (Fig. 11a). In all cases, FeO contents are greater than MgO and on Na/(Na + Ca) versus Fe/(Fe + Mg) diagram, tourmaline composition plots in the schorl field (Fig. 11b). On the Mg versus Fe diagram of London and Manning (1995), tourmaline shows composition below to the line Σ(Fe + Mg) = 3 that corresponds to the dravite–schorl exchange vector $FeMg_{-1}$ and there is, also, a systematic departure toward alkali-deficient tourmaline and oxy-tourmaline, which is due to Al substitution in the Y-site (R2) (Fig. 11c). On the diagram of Manning (1982), our compositional data are plotted in terms of the cation groups, i.e., R3 versus R1 + R2 where R1 = (Na + Ca), R2 = (Fe + Mg), and R3 = (Al + 1.33Ti). R1, R2, and R3 correspond to *X*, *Y*, and *Z* sites of the tourmaline formula, respectively. As can be seen in Fig. 11d, all tourmalines fall between the exchange vectors labeled proton deficient ($AlOMg_{-1}(OH)_{-1}$), and alkali deficient ($\square AlNa_{-1}Mg_{-1}$), substitution, implying that both alkali-deficient and proton-deficient substitutions have been effective on the composition of the studied tourmalines. Manning (1982) found that the extent of such coupled substitutions

**Table 7** EPMA analyses of muscovites of the Hamedan region

| Sample | 1. MT6 | 2. MT6 | 3. MT6 | 4. MT6 | 1. Ar4 | 2. Ar4 | 3. Ar4 |
|---|---|---|---|---|---|---|---|
| $SiO_2$ | 46.30 | 46.00 | 46.10 | 45.50 | 45.60 | 45.90 | 46.30 |
| $TiO_2$ | 0.43 | 0.43 | 0.32 | 0.32 | 0.06 | 0.07 | 0.06 |
| $Al_2O_3$ | 35.10 | 36.30 | 36.20 | 37.10 | 36.60 | 36.50 | 36.70 |
| FeO | 0.70 | 0.69 | 0.61 | 1.03 | 1.97 | 1.87 | 1.79 |
| MnO | 0.01 | 0.00 | 0.00 | 0.00 | 0.01 | 0.06 | 0.02 |
| MgO | 0.66 | 0.70 | 0.65 | 0.57 | 0.06 | 0.12 | 0.09 |
| CaO | 0.01 | 0.04 | 0.01 | 0.03 | 0.01 | 0.04 | 0.04 |
| $Na_2O$ | 0.82 | 0.94 | 0.90 | 1.04 | 0.56 | 0.54 | 0.63 |
| $K_2O$ | 10.90 | 10.90 | 11.00 | 10.10 | 11.50 | 11.50 | 11.20 |
| Total | 95.00 | 96.00 | 95.80 | 95.70 | 96.40 | 96.60 | 96.80 |
| Number of cations on the basis of 22 oxygens | | | | | | | |
| Si | 6.19 | 6.09 | 6.11 | 6.02 | 6.06 | 6.08 | 6.1 |
| Ti | 0.04 | 0.04 | 0.03 | 0.03 | 0.01 | 0.01 | 0.01 |
| Al | 5.52 | 5.66 | 5.65 | 5.78 | 5.73 | 5.69 | 5.7 |
| Fe | 0.08 | 0.08 | 0.07 | 0.11 | 0.22 | 0.21 | 0.2 |
| Mn | 0 | 0 | 0 | 0 | 0 | 0.01 | 0 |
| Mg | 0.13 | 0.14 | 0.13 | 0.11 | 0.01 | 0.02 | 0.02 |
| Ca | 0 | 0.01 | 0 | 0 | 0 | 0.01 | 0.01 |
| Na | 0.21 | 0.24 | 0.23 | 0.27 | 0.14 | 0.14 | 0.16 |
| K | 1.87 | 1.84 | 1.86 | 1.7 | 1.94 | 1.95 | 1.88 |
| Sum | 14.1 | 14.1 | 14.1 | 14 | 14.1 | 14.1 | 14.1 |

**Table 8** EPMA analyses of biotites of the Hamedan region

| Sample | 1. Mso4 | 2. Mso4 | 3. Mso4 | 4. Mso4 | 5. Mso4 | 1. Ar10 | 2. Ar10 | 3. Ar10 | 4. Ar10 |
|---|---|---|---|---|---|---|---|---|---|
| $SiO_2$ | 35.43 | 36.02 | 36.34 | 35.75 | 36.85 | 35.53 | 34.32 | 34.13 | 34.95 |
| $TiO_2$ | 4.82 | 4.77 | 4.76 | 4.75 | 4.81 | 2.97 | 2.91 | 3.03 | 2.94 |
| $Al_2O_3$ | 13.96 | 13.83 | 13.84 | 14.49 | 14.13 | 15.14 | 14.44 | 13.85 | 14.02 |
| FeO | 21.84 | 22.13 | 21.48 | 21.97 | 18.91 | 24.34 | 24.01 | 24.04 | 23.85 |
| MnO | 0.16 | 0.16 | 0.13 | 0.14 | 0.11 | 0.35 | 0.36 | 0.32 | 0.33 |
| MgO | 9.14 | 9.33 | 9.00 | 9.08 | 10.68 | 8.47 | 8.13 | 7.65 | 7.86 |
| CaO | 0.10 | 0.02 | 0.05 | 0.05 | 0.00 | 0.11 | 0.10 | 0.26 | 0.07 |
| $Na_2O$ | 0.12 | 0.10 | 0.18 | 0.09 | 0.08 | 0.22 | 0.24 | 0.19 | 0.12 |
| $K_2O$ | 10.17 | 10.23 | 10.12 | 10.03 | 10.44 | 9.63 | 9.64 | 9.61 | 9.68 |
| Total | 95.74 | 96.59 | 95.90 | 96.35 | 96.01 | 96.76 | 94.15 | 93.08 | 93.82 |
| Number of cations on the basis of 22 oxygens | | | | | | | | | |
| Si | 5.51 | 5.55 | 5.61 | 5.51 | 5.61 | 5.5 | 5.49 | 5.53 | 5.6 |
| Ti | 0.56 | 0.55 | 0.55 | 0.55 | 0.55 | 0.35 | 0.35 | 0.37 | 0.35 |
| Al | 2.56 | 2.51 | 2.52 | 2.63 | 2.54 | 2.76 | 2.72 | 2.65 | 2.65 |
| Fe | 2.84 | 2.85 | 2.77 | 2.83 | 2.41 | 3.15 | 3.21 | 3.26 | 3.19 |
| Mn | 0.02 | 0.02 | 0.02 | 0.02 | 0.01 | 0.05 | 0.05 | 0.04 | 0.04 |
| Mg | 2.12 | 2.14 | 2.07 | 2.08 | 2.42 | 1.96 | 1.94 | 1.85 | 1.88 |
| Ca | 0.02 | 0 | 0.01 | 0.01 | 0 | 0.02 | 0.02 | 0.05 | 0.01 |
| Na | 0.04 | 0.03 | 0.05 | 0.03 | 0.02 | 0.07 | 0.07 | 0.06 | 0.04 |
| K | 2.02 | 2.01 | 1.99 | 1.97 | 2.03 | 1.9 | 1.97 | 1.99 | 1.98 |
| Sum | 15.68 | 15.66 | 15.6 | 15.63 | 15.59 | 15.75 | 15.82 | 15.8 | 15.73 |
| Mg/Fe + Mg | 0.43 | 0.43 | 0.43 | 0.42 | 0.5 | 0.38 | 0.38 | 0.36 | 0.37 |

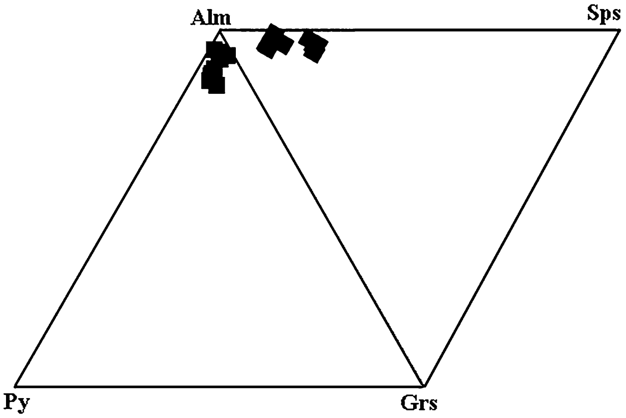

**Fig. 10** Plot of chemical compositions of garnets in almandine-pyrope-grossular-spessartine diagram. Garnet compositions are almandine-rich

become greater with decreasing temperature, i.e., with an increase in the degree of fractionation. On the Al–Fe–Mg and Ca–Fe–Mg diagrams of Henry and Guidotti (1985) that show the relationship between tourmaline composition and the host rock type, tourmaline compositions exclusively plot in field 2, corresponding to tourmaline from Li-poor granitic rocks and associated pegmatites and aplites (Fig. 12).

### *Feldspars*

The $Na_2O$ contents (0.00–1.24 wt%) and also CaO contents are very low (0.00–0.03 wt%) in K-feldspars. The chemical analyses of K-feldspars (Table 5) plotted on Or–Ab–An diagram indicate that orthoclase component of the bulk K-feldspar is higher than 90, which means that this mineral is nearly Na-poor alkali feldspar. The CaO contents (anorthite components) of analyzed plagioclase crystals are very low (near zero) (Table 6), which indicates an evolved affinity of these pegmatites.

### *Muscovite*

Muscovite compositions show low amounts of FeO (0.61–1.97 wt%), MgO (0.06–0.7 wt%), and $TiO_2$ (0.06–0.43 wt%). The chemical analyses of white micas (Table 7; Fig. 13a) are near the muscovite end-member in $SiO_2$-$Al_2O_3$-(FeO + MgO) triangular plot (Vidal et al. 1999). As indicated in the plot muscovites are low paragonite end-member in their compositions (Fig. 13a). Muscovite compositions in the diagram of Al (apfu) vs. Si (apfu) have plots in the muscovite area (Si <3.1 apfu) (Fig. 13b) that indicate the Si:Al ratio in the muscovite composition is not greater than 3:1, so these white micas are nearly pure muscovite.

### *Biotite*

The EPMA of biotites are shown in Table 8. The ranges in wt% are $TiO_2$ 2.91 to 4.82, FeO 18.91 to 24.34, MgO 7.65 to 10.68, $Al_2O_3$ 13.83 to 15.14, and $K_2O$ 9.62 to 10.44. Biotites contain moderate to high contents of Ti and their XMg are between 38 and 50. Biotite compositions plot near the siderophyllite field in eastonite–siderophyllite–phlogopite–annite rectangular diagram (Deer et al. 1982) (Fig. 14a). Also, in $SiO_2$–$Al_2O_3$–(FeO + MgO) ternary diagram (Vidal et al. 1999), the compositions of biotites plot near the siderophyllite-eastonite field (Fig. 13a). Abdel-Rahman (1994) defined discrimination diagrams on the basis of major elements (FeO, MgO, $Al_2O_3$) of biotites in igneous rocks crystallized from A (Anorogenic alkaline suites), P (Peraluminous suites), and C (Calc-alkaline orogenic suites) magma types. Based on his classification, the studied biotites belong to peraluminous granite (P) suites (S-type) (Fig. 14b–d) that are consistent with the peraluminous whole rock composition of the studied pegmatites and aplites (Fig. 6b).

Nachit et al. (1985) used mica composition in granitoids to relate magma types in which biotite crystallized. On the basis of the Al (tot) vs. Mg classification diagram, the nature of granitoid magmas from biotite compositions from the Hamedan region pegmatites and aplites plots in the peraluminous field (Fig. 14e).

## U–Pb geochronology

Cathodoluminescence (CL) and SEM-BSE images of selected analyzed zircon, monazite, and allanite are shown in Fig. 15. Monazites are anhedral to subhedral prismatic grains. Sizes of analyzed monazite grains were 50–800 µm. Zircon grains are anhedral to euhedral prismatic. Sizes of analyzed zircon grains were 10–150 µm. Allanite occurs as large subhedral crystals up to 1.5 cm in size (easily visible even in field outcrops and hand specimens).

For sample SNM41, the monazite has a Concordia age (weighted mean of overlapping concordant analyses) of 172.2 ± 0.9 Ma (MSWD of concordance = 0.019; probability of concordance = 0.89; Fig. 16a). For sample SNM42, monazite has a Concordia age of 169.2 ± 0.9 Ma (MSWD of concordance = 0.0012; probability of concordance = 0.97; Fig. 16b). For sample SNM422, monazite has a Concordia age of 169.8 ± 0.8 Ma (MSWD of concordance = 4.43; probability of concordance = 0.037; Fig. 16c). For sample Bar1,

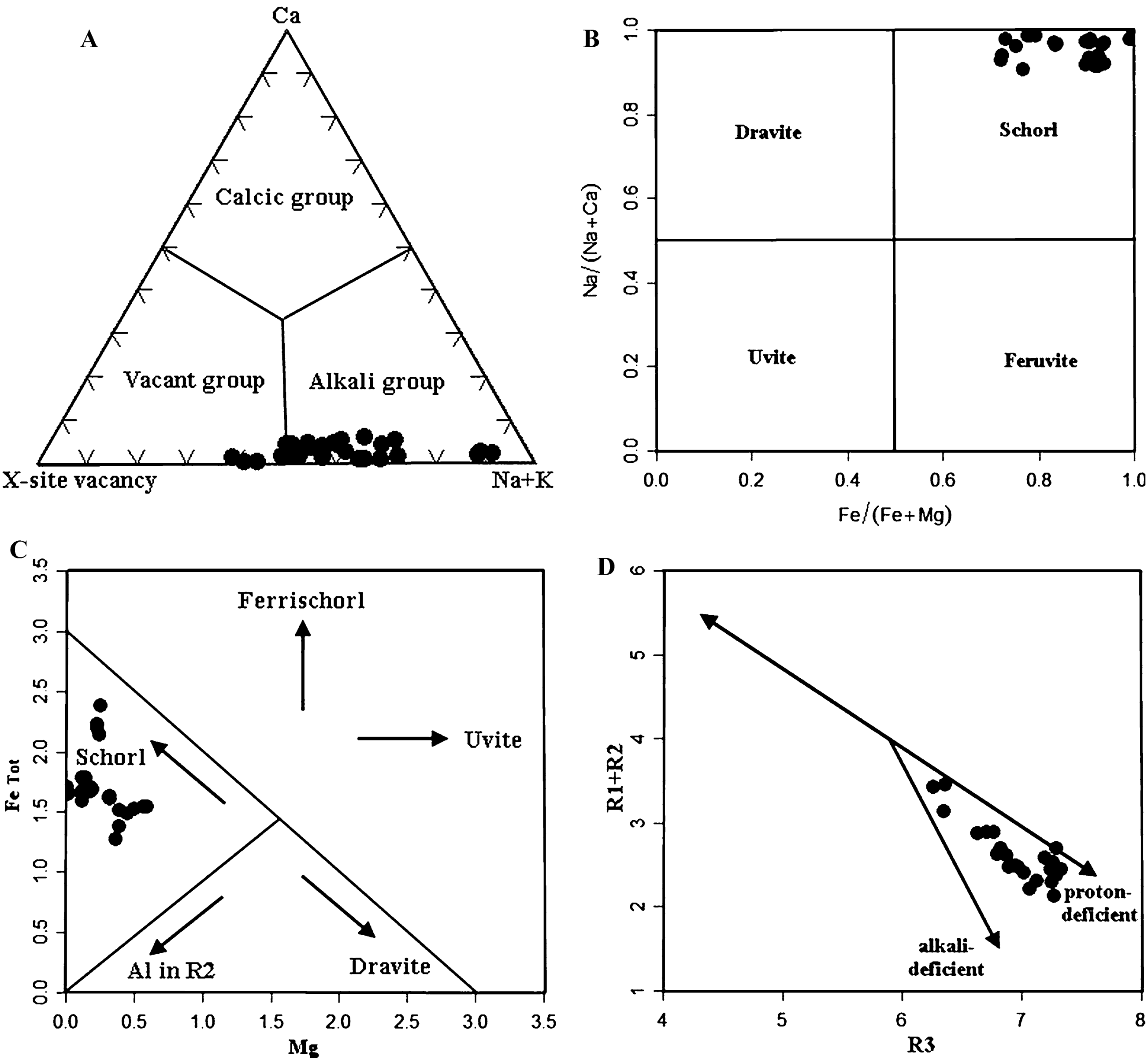

**Fig. 11** **a** Plot of tourmaline compositions of Hamedan region on Ca-(X site vacancy)-(Na + K) diagram (Hawthorne and Henry 1999), which indicate that most studied tourmalines plot in the alkali field. **b** Plot of tourmaline compositions on Na/(Na + Ca)-Fe/(Fe + Mg) diagram. Tourmaline compositions are plotted in schorl field. **c** Plot of concentration of Fe versus that of Mg in study tourmalines (London and Manning 1995). Values are expressed in atoms per formula unit. **d** Compositional variations in study tourmalines are shown in relation to common substitution mechanisms in tourmalines (Manning 1982). The R1 variable is Ca + Na, the R2 variable is Fe + Mg + Mn, and the R3 variable is Al + 1.33Ti. The variations can be related to alkali defect and proton-loss substitutions in tourmaline. The vectors represent the possible exchange operator that could have operated in these tourmalines

monazite has a Concordia age of 166.2 ± 1.1 Ma (MSWD of concordance = 0.64; probability of concordance = 0.42; Fig. 16d). For sample Bar11, the monazite has a Concordia of 162.6 ± 0.8 Ma (MSWD of concordance = 0.42; probability of concordance = 0.52; Fig. 16e). Th/U ratios of monazite are quite variable with monazites of the Heydareh-e-Poshteshahr area having values ranging from7.92 to 39.59 (ave. 23.32), whereas monazites from the Barfejin area have a wider range of 0.08 to 81.82 (ave. 15.85).

For sample SNM4 near-concordant zircon analyses range between between ~158 and ~172 Ma with average $^{206}Pb/^{238}U$ age near ~165 Ma (Fig. 16f). Th/U ratios for zircon of Heydareh-e-Poshteshahr area are 0.02 to 1.23 (ave. 0.31).

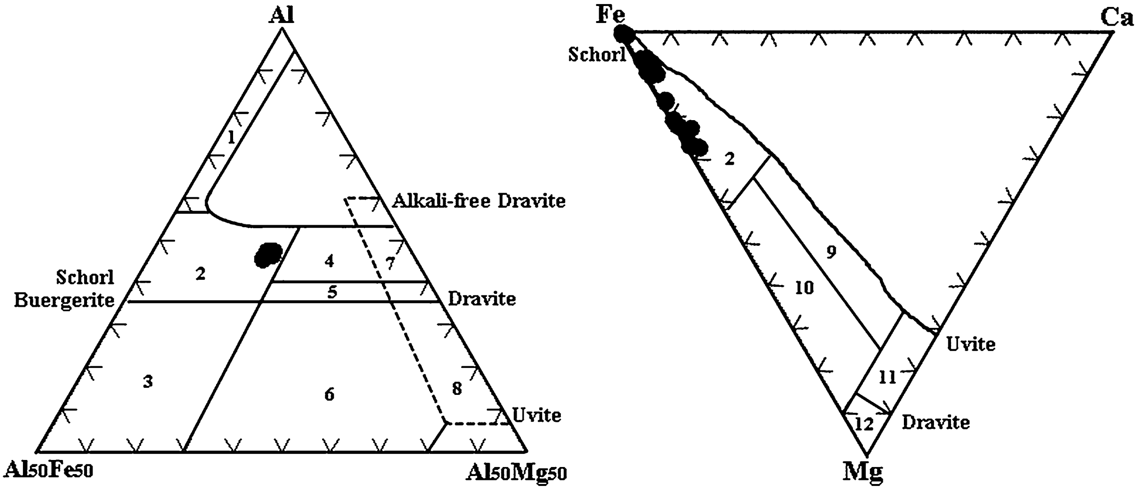

**Fig. 12** Ternary Al–Fe–Mg and Ca–Fe–Mg diagram showing compositions of tourmaline from aplite and pegmatite of Hamedan area. The regions define the compositions of tourmaline from different rock types (Henry and Guidotti 1985). *1* Li-rich granitoids and associated pegmatites and aplites; *2* Li-poor granitoids and associated pegmatites and aplites; *3* $Fe^{3+}$ rich quartz–tourmaline rocks (hydrothermally altered granites); *4* metapelites and metapsammites coexisting with an Al-saturating phase; *5* metapelites and metapsammites not coexisting with an Al-saturating phase; *6* $Fe^{3+}$ rich quartz–tourmaline rocks, calc silicate rocks, and metapelites; *7* low Ca metaultramafics and Cr, V-rich metasediments; *8* metacarbonates and metapyroxenites. *9* Ca-rich metapsammites and metapelites. *10* quartz–tourmaline rocks, Ca poor metapsammites and metapelites. *11* metacarbonates. *12* metaultramafics

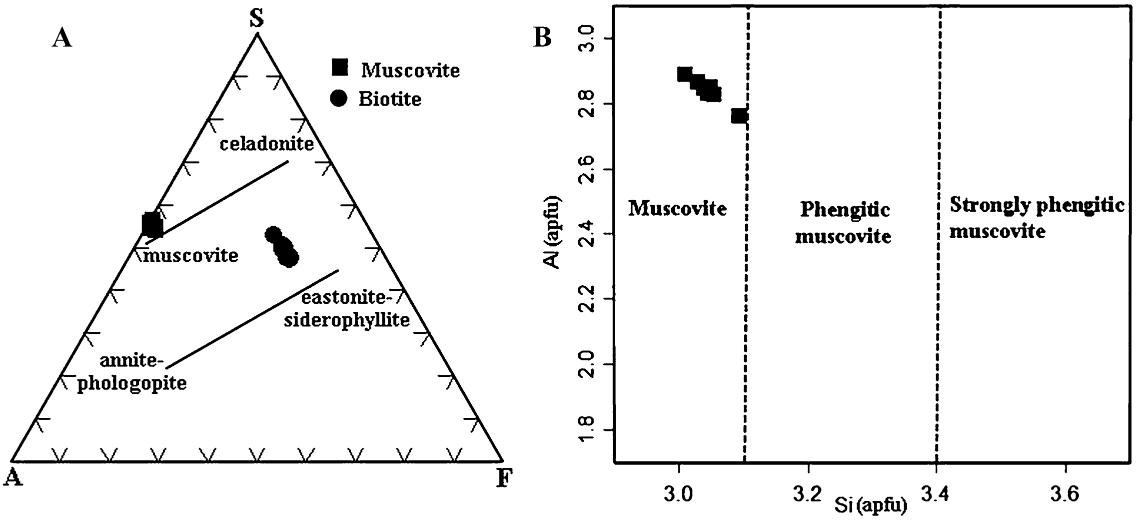

**Fig. 13** **a** Chemical analyses of white micas and biotites on $SiO_2$-$Al_2O_3$-(FeO + MgO) *triangular plot* (Vidal et al. 1999). **b** Composition of study muscovites on the Al (apfu) vs. Si (apfu) diagram

For sample Art19, allanite produced an inverse isochron (Fig. 17) with a lower intercept at 154.1 ± 3.7 Ma (MSWD = 2.4) and Th/U ratios for allanite of Artiman area 7.05 to 46.96 (ave. 17.80).

Details of determined values, isotopic ratios, and age calculations for the studied samples are reported in Tables 9, 10, 11 and 12.

## Discussion

The concentration of incompatible elements of the studied pegmatites and aplites is not as much as Tanco pegmatites in Canada as extremely fractionated LCT pegmatites, but it can be compared with LCT pegmatites of Moose II, Canada (Anderson et al. 2013), for lithophile elements and

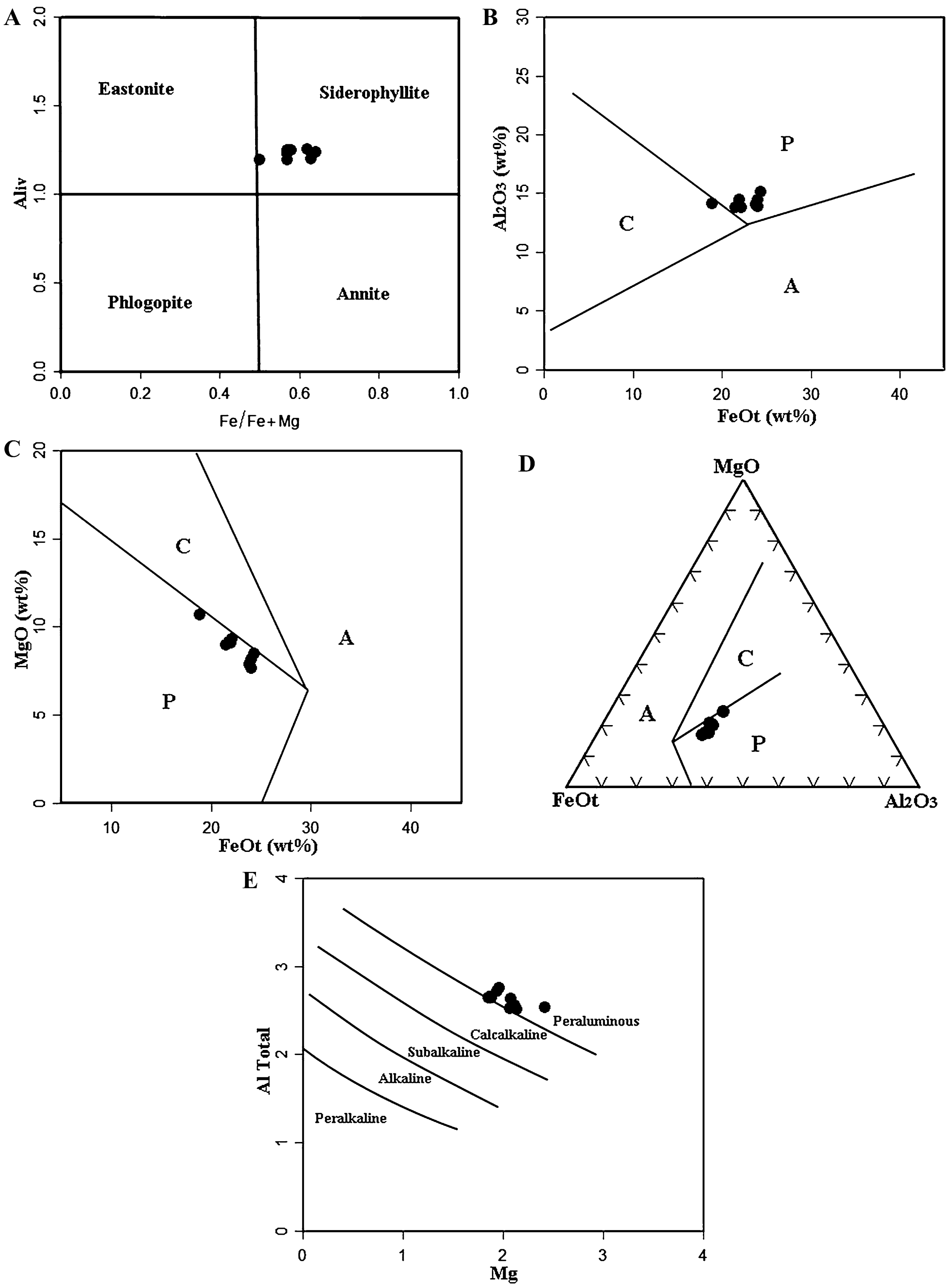

**Fig. 14** **a** Chemical analyses of biotites on $Al^{IV}$–Fe/(Fe + Mg) diagram (Deer et al. 1982). **b–d** Distribution of biotites on Abdel-Rahman's tectonomagmatic discrimination diagrams (Abdel-Rahman 1994), *A* alkaline, *C* calc-alkaline, and *P* peraluminous granite fields. **e** Biotites from Hamedan region pegmatites and aplites plotted in Nachit et al. (1985) diagram to find out the type of magma

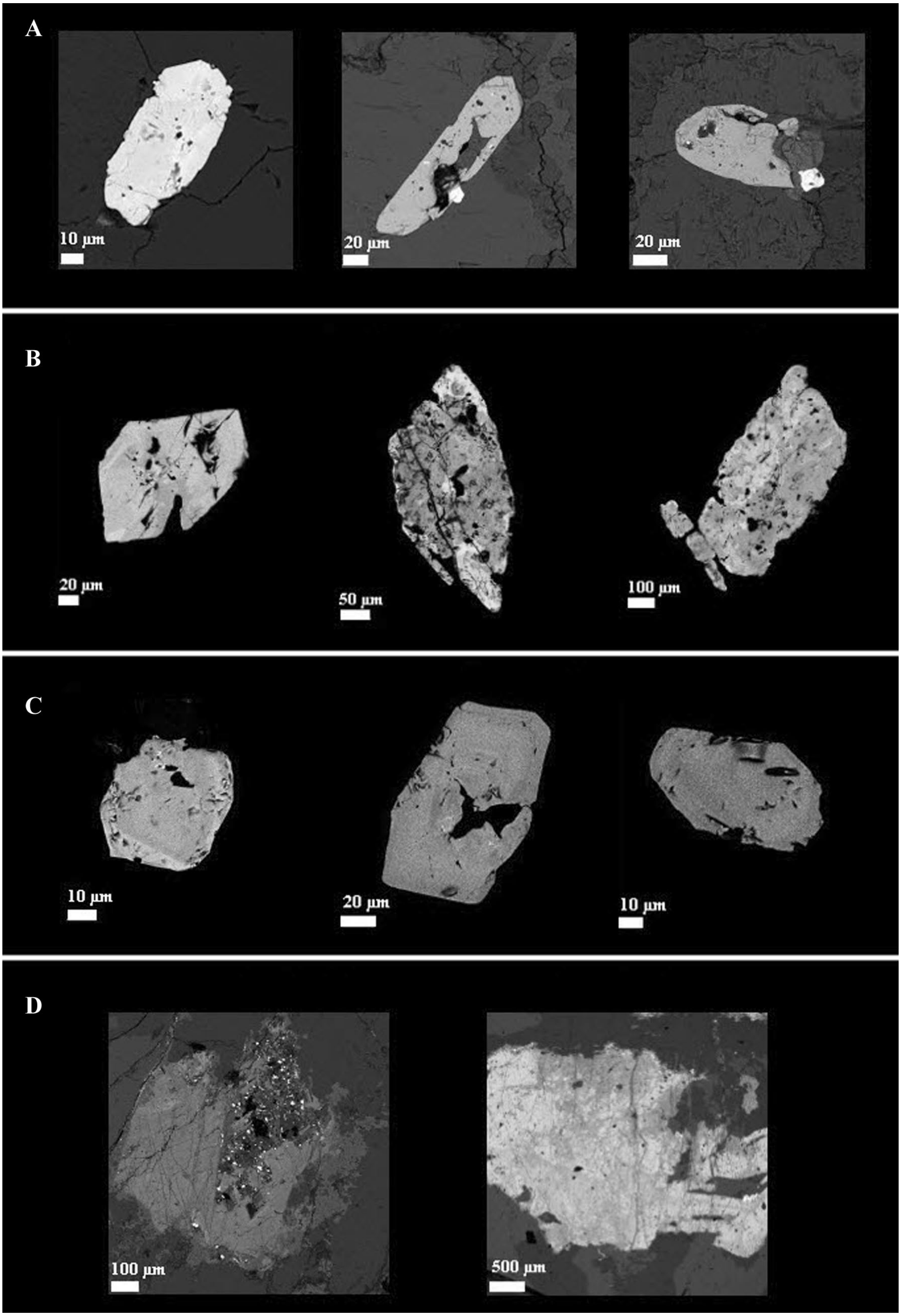

**Fig. 15** **a** SEM-BSE images of analyzed zircons of the Heydare-e-Poshteshahr area, west of Hamedan. **b** CL images of analyzed monazites from Heydareh-e-Poshteshahr area, west of Hamedan. **c** CL images of analyzed monazites from Barfejin area, west of Hamedan. **d** SEM-BSE images of analyzed allanites from Artiman area, north of Tueyserkan, south of Hamedan

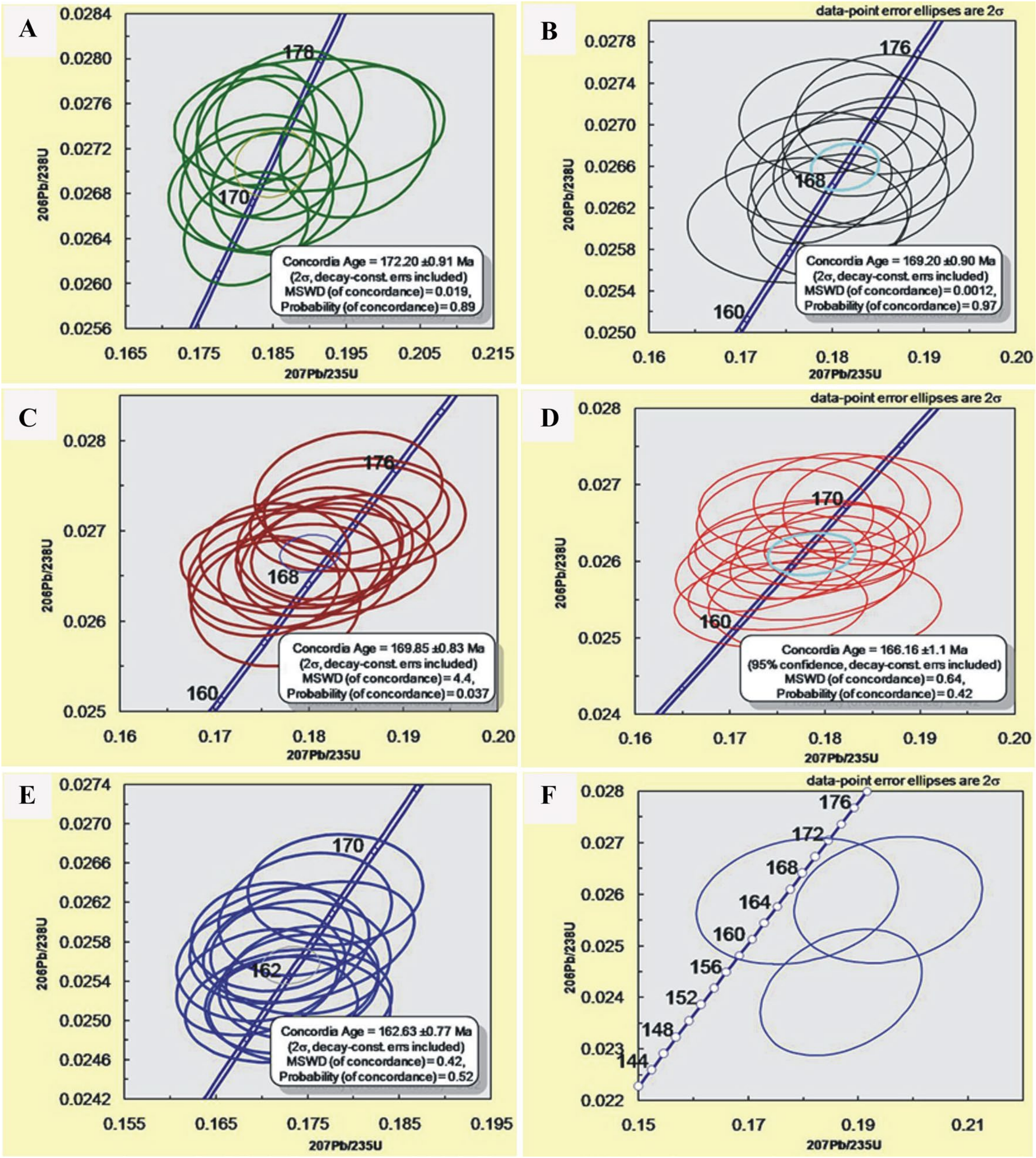

**Fig. 16** Concordia diagrams for various samples of the studied region (**a**–**e** on monazite and **f** on zircon). **a** SNM41, **b** SNM42, **c** SNM422, **d** Bar1, **e** Bar11, and **f** SNM4 (see text)

REE. The concentration of LILE in the studied aplites and pegmatites are commonly higher than the fine-grained wall zone of the Moose II pegmatites. Also, according to the classification scheme of Cerný and Ercit (2005), their geochemical (aluminum saturation index (peraluminous affinity) and concentration of essential rare elements) and geological properties resemble the LCT family of pegmatites.

As shown in Fig. 6c, the studied aplites and pegmatites are geochemically similar to S-type granites according to Chappell and White (1992) scheme of classification of granitic rocks. Also, Sepahi (1999, 2008) has referred to the existence of a genetic link between S-type granites and, aplites and pegmatites in the Hamedan region by using geochemical properties of these rocks. Mineralogically, the studied aplites and pegmatites resemble Muscovite (MS) and Muscovite Rare Element (MSREL) classes of pegmatites (cf. Cerný and Ercit 2005).

The aplitic–pegmatitic dykes have intruded various host lithologies including plutonic, contact metamorphic, and regional metamorphic rocks. Those dykes located inside

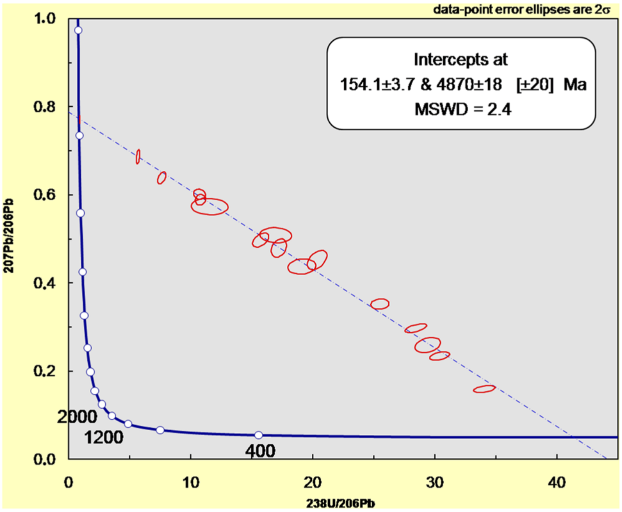

**Fig. 17** Inverse isochron for allanite from sample Art19

pluton (mostly intruding biotite monzogranite-granodiorite) and its contact aureole appear to be spatially and genetically related to each other (see also Sepahi 1999, 2008). Regional metamorphic host of dykes located outside of the pluton are commonly medium- to high-grade schists and migmatites (i.e., commonly garnet–andalusite–sillimanite schists and low-pressure migmatites). These aplites–pegmatites can be considered as partial melts resulting from anatexis of their metasedimentary hosts. All aplitic–pegmatitic dykes (i.e., those located at the interior, margin, and exterior to pluton) have peraluminous affinity and could be considered as S-type orogenic group pegmatites. This S-type suite of granites and aplites-pegmatites has been produced by intense partial melting (diatexis) of continental crustin an intra-continental arc setting by intrusion of large amounts of mafic magmas (e.g., Sepahi 1999, 2008). Therefore, they are considered to be synchronous with subduction rather than small syn-collisional leucogranitic S-type granitoids. Mineralogical and geochemical characteristics of these aplite–pegmatite dykes indicate that they likely were injected from highly fractionated granitic melts at depth (see Sects. 3 and 5) within a thermally anomalous gradient that may enhance further fractionation during emplacement.

Field observations, mineral assemblages, and chemical compositions of the studied rocks are consistent with each other. According to Christiansen and Keith (1996), the trace element signatures of granitic rocks can be closely related to their melting and crystallization histories. For example, they have emphasized that Be concentrations are high enough to saturate beryl just in highly evolved granites and pegmatites. In the studied pegmatites, concentrations of Be were not determined, although high concentrations of Be could be inferred by field observations for occurrence of coarse-grained beryl crystals inthe pegmatites in some localities, such as the Dehno area. According to Baker (1998), more-evolved pegmatitic dykes usually occur far from their host pluton than less-evolved ones and that pegmatites should not be associated with small plutons. This is in accordance with our observation that pegmatitic dykes near Alvand pluton have no beryl mineral, but in dykes far from pluton large crystals of beryl with a fractionated assemblage have been found. Also, the Alvand pluton is large enough (nearly 400 km$^2$ in area) to produce associated pegmatitic dykes at its interior, margin, and exterior.

Tourmaline occurs as a common accessory phase in nearly all the aplites and pegmatites. Boron activity has been high in the source melts according to ubiquitous tourmaline crystallization in many pegmatitic and aplitic dykes of the region. High concentrations of B and the presence of tourmaline can be good indicators of anatectic origin for S-type silicic magmas. Boron is highly concentrated in sediments (nearly up to 100 ppm) compared to the mantle (0.1 ppm). This characteristic may become intrinsic to metasedimentary rocks and to magmas derived from these rocks. On the basis of the observation that tourmaline modal percent reached up to 25 in some studied pegmatitic/aplitic dykes, metasedimentary pelitic rocks can be considered as one of the source rocks for silicic magmas in the region.

S-type granites occur both as isolated small plutons and in batholithic associations. Although S-type granites are commonly considered as syn-collisional granites (e.g., Pearce et al. 1984), these rocks may be abundant in other convergent environments in association with I-type (including M-type) granites. The S-type granites are usually formed in regions underlain by thick sequences of metasedimentary rocks, such as metamorphosed shales, greywackes, and sandstones. The composition of source rocks is the most important factor in determining the compositions of partial melts and granites produced by this process (e.g., Gao et al. 2016). The cause of the melting of metasedimentary rocks to produce S-type silicic magmas varies from one tectonic setting to another.

Mantle-derived mafic magmas can be a source of heat and fluid necessary for partial melting of crustal rocks (Gao et al. 2016). These magmas may provide the heat necessary for crustal melting and producing S-type granites, especially in arc settings (Brown 2013 and references therein). The formation of upper crustal plutons (especially S-type granitic plutons) requires that melt be generated and separated from solid residue within lower crustal sources and then become focused into high-permeability ascent conduits to feed the roots of plutons (Brown 2010, 2013). According to a general model for emplacement of plutons (Fig. 14 in Brown 2013), the Alvand pluton is similar to blobby and composite plutons formed in a ductile compressive regime.

**Table 9** U–Pb LA-ICPMS data of analyzed monazite grains from the Heydareh-e-Poshteshahr area, west of Hamedan

| Comments | U (ppm) | Th (ppm) | Th/U | 207Pb/235U | 2σ | 206Pb/238U | 2σ | Err. corr. | 207Pb/206Pb | 2σ | 207Pb/235U | 2σ | 206Pb/238U | 2σ | 238U/206Pb | 2σ | 207Pb/206Pb | 2σ | Err. corr. |
|---|---|---|---|---|---|---|---|---|---|---|---|---|---|---|---|---|---|---|---|
| SNM41-1mz-1 | 6020 | 208,700 | 34.67 | 0.197 | 0.009 | 0.0273 | 0.0006 | 0.216 | 0.0516 | 0.0019 | 182 | 7 | 173 | 3 | 42.00 | 0.74 | 0.052 | 0.002 | 0.32 |
| SNM41-1mz-2 | 8430 | 172,100 | 20.42 | 0.183 | 0.008 | 0.0269 | 0.0005 | 0.173 | 0.0490 | 0.0019 | 172 | 7 | 171 | 3 | 37.00 | 0.68 | 0.049 | 0.002 | 0.15 |
| SNM41-1mz-3 | 9180 | 160,700 | 17.51 | 0.184 | 0.011 | 0.0268 | 0.0005 | 0.119 | 0.0494 | 0.0027 | 171 | 10 | 171 | 3 | 50.00 | 0.63 | 0.049 | 0.003 | 0.19 |
| SNM41-1mz-5 | 7860 | 198,200 | 25.22 | 0.187 | 0.008 | 0.0275 | 0.0005 | 0.183 | 0.0491 | 0.0019 | 174 | 7 | 175 | 3 | 44.00 | 0.62 | 0.049 | 0.002 | 0.27 |
| SNM41-1mz-6 | 6169 | 160,700 | 26.05 | 0.210 | 0.028 | 0.0265 | 0.0006 | 0.256 | 0.0572 | 0.0057 | 193 | 21 | 169 | 4 | 30.00 | 0.81 | 0.057 | 0.006 | 0.23 |
| SNM41-2mz-1 | 7430 | 172,900 | 23.27 | 0.185 | 0.007 | 0.0268 | 0.0004 | 0.057 | 0.0494 | 0.0016 | 172 | 6 | 171 | 3 | 39.00 | 0.61 | 0.049 | 0.002 | 0.41 |
| SNM41-2mz-2 | 7960 | 143,400 | 18.02 | 0.183 | 0.007 | 0.0274 | 0.0004 | 0.149 | 0.0474 | 0.0016 | 170 | 6 | 174 | 3 | 32.00 | 0.59 | 0.047 | 0.002 | 0.51 |
| SNM41-2mz-3 | 7272 | 154,700 | 21.27 | 0.190 | 0.015 | 0.0274 | 0.0005 | 0.091 | 0.0494 | 0.0035 | 176 | 12 | 174 | 3 | 62.00 | 0.64 | 0.049 | 0.004 | 0.35 |
| SNM41-2mz-4 | 5913 | 134,700 | 22.78 | 0.182 | 0.007 | 0.0272 | 0.0005 | 0.078 | 0.0471 | 0.0017 | 169 | 6 | 173 | 3 | 36.00 | 0.68 | 0.047 | 0.002 | 0.45 |
| SNM41-2mz-5 | 6200 | 138,700 | 22.37 | 0.181 | 0.007 | 0.0265 | 0.0004 | 0.231 | 0.0490 | 0.0015 | 170 | 6 | 169 | 3 | 32.00 | 0.58 | 0.049 | 0.002 | 0.15 |
| SNM41-3mz-1 | 8770 | 161,400 | 18.40 | 0.185 | 0.008 | 0.0272 | 0.0005 | 0.036 | 0.0479 | 0.0021 | 172 | 7 | 173 | 3 | 33.00 | 0.70 | 0.048 | 0.002 | 0.39 |
| SNM41-3mz-2 | 7610 | 273,900 | 35.99 | 0.275 | 0.012 | 0.0279 | 0.0005 | 0.045 | 0.0699 | 0.0028 | 246 | 10 | 177 | 3 | 66.00 | 0.62 | 0.070 | 0.003 | 0.31 |
| SNM41-3mz-3 | 6995 | 202,300 | 28.92 | 0.174 | 0.007 | 0.0263 | 0.0005 | 0.260 | 0.0480 | 0.0017 | 164 | 6 | 167 | 3 | 42.00 | 0.71 | 0.048 | 0.002 | 0.13 |
| SNM41-14MzZr-1 | 6400 | 124,400 | 19.44 | 0.268 | 0.028 | 0.0273 | 0.0007 | 0.570 | 0.0710 | 0.0060 | 239 | 18 | 174 | 4 | 84.00 | 0.94 | 0.071 | 0.006 | −0.29 |
| SNM41-14MzZr-2 | 5650 | 93,500 | 16.55 | 0.237 | 0.009 | 0.0273 | 0.0005 | 0.090 | 0.0626 | 0.0020 | 216 | 7 | 174 | 3 | 44.00 | 0.64 | 0.063 | 0.002 | 0.29 |
| SNM41-14MzZr-3 | 7650 | 136,100 | 17.79 | 0.175 | 0.007 | 0.0261 | 0.0004 | 0.281 | 0.0481 | 0.0014 | 164 | 6 | 166 | 3 | 42.00 | 0.63 | 0.048 | 0.001 | 0.15 |
| SNM41-14MzZr-4 | 10,080 | 122,600 | 12.16 | 0.933 | 0.084 | 0.0360 | 0.0016 | 0.650 | 0.1790 | 0.0120 | 649 | 43 | 228 | 10 | 92.00 | 1.23 | 0.179 | 0.012 | −0.19 |
| SNM42-1Mz-1 | 6330 | 187,300 | 29.59 | 0.183 | 0.008 | 0.0266 | 0.0005 | 0.186 | 0.0496 | 0.0017 | 170 | 7 | 169 | 3 | 35.00 | 0.66 | 0.050 | 0.002 | 0.24 |
| SNM42-1Mz-2 | 9400 | 170,900 | 18.18 | 0.179 | 0.006 | 0.0264 | 0.0004 | 0.338 | 0.0490 | 0.0014 | 167 | 6 | 168 | 3 | 33.00 | 0.59 | 0.049 | 0.001 | 0.10 |
| SNM42-1Mz-3 | 7910 | 275,000 | 34.77 | 0.220 | 0.010 | 0.0273 | 0.0005 | 0.162 | 0.0590 | 0.0026 | 202 | 9 | 173 | 3 | 56.00 | 0.66 | 0.059 | 0.003 | 0.19 |
| SNM42-1Mz-4 | 6797 | 157,300 | 23.14 | 0.185 | 0.009 | 0.0267 | 0.0005 | 0.153 | 0.0496 | 0.0020 | 173 | 7 | 170 | 3 | 47.00 | 0.70 | 0.050 | 0.002 | 0.26 |
| SNM42-1Mz-5 | 6011 | 194,700 | 32.39 | 0.131 | 0.082 | 0.0266 | 0.0008 | 0.710 | 0.0160 | 0.0200 | 110 | 77 | 169 | 147 | 31.00 | 0.54 | 0.246 | 0.006 | −0.02 |
| SNM42-2Mz-1 | 7380 | 165,300 | 22.40 | 0.186 | 0.008 | 0.0271 | 0.0005 | 0.046 | 0.0502 | 0.0020 | 173 | 7 | 172 | 3 | 40.00 | 0.64 | 0.050 | 0.002 | 0.30 |

**Table 9** (continued)

| Comments | U (ppm) | Th (ppm) | Th/U | 207Pb/235U | 2σ | 206Pb/238U | 2σ | Err. corr. | 207Pb/206Pb | 2σ | 207Pb/235U | 2σ | 206Pb/238U | 2σ | 238U/206Pb | 2σ | 207Pb/206Pb | 2σ | Err. corr. |
|---|---|---|---|---|---|---|---|---|---|---|---|---|---|---|---|---|---|---|---|
| SNM42-2Mz-2 | 8600 | 165,500 | 19.24 | 0.176 | 0.010 | 0.0261 | 0.0005 | 0.069 | 0.0481 | 0.0024 | 165 | 8 | 166 | 3 | 35.00 | 0.72 | 0.048 | 0.002 | 0.45 |
| SNM42-2Mz-3 | 8420 | 227,000 | 26.96 | 0.254 | 0.018 | 0.0269 | 0.0006 | 0.403 | 0.0676 | 0.0043 | 228 | 14 | 171 | 4 | 70.00 | 0.88 | 0.068 | 0.004 | −0.03 |
| SNM42-6Mz-1 | 7360 | 173,900 | 23.63 | 0.183 | 0.007 | 0.0269 | 0.0005 | 0.152 | 0.0484 | 0.0017 | 171 | 6 | 171 | 3 | 39.00 | 0.66 | 0.048 | 0.002 | 0.23 |
| SNM42-6Mz-2 | 8580 | 266,900 | 31.11 | 0.182 | 0.009 | 0.0264 | 0.0005 | 0.034 | 0.0487 | 0.0022 | 169 | 8 | 168 | 3 | 46.00 | 0.74 | 0.049 | 0.002 | 0.34 |
| SNM42-6Mz-3 | 6328 | 141,600 | 22.38 | 0.280 | 0.014 | 0.0280 | 0.0005 | 0.411 | 0.0709 | 0.0029 | 251 | 11 | 178 | 3 | 73.00 | 0.63 | 0.071 | 0.003 | −0.09 |
| SNM42-6Mz-4 | 7060 | 243,300 | 34.46 | 0.218 | 0.008 | 0.0265 | 0.0004 | 0.156 | 0.0584 | 0.0016 | 200 | 7 | 169 | 3 | 31.00 | 0.63 | 0.058 | 0.002 | 0.27 |
| SNM42-6Mz-5 | 8020 | 144,700 | 18.04 | 0.278 | 0.020 | 0.0278 | 0.0005 | 0.102 | 0.0734 | 0.0046 | 250 | 15 | 177 | 3 | 93.00 | 0.63 | 0.073 | 0.005 | 0.16 |
| SNM42-6Mz-6 | 9270 | 127,000 | 13.70 | 0.180 | 0.007 | 0.0261 | 0.0005 | 0.194 | 0.0489 | 0.0015 | 168 | 6 | 166 | 3 | 31.00 | 0.70 | 0.049 | 0.002 | 0.24 |
| SNM42-9Mz-1 | 5826 | 98,300 | 16.87 | 0.179 | 0.008 | 0.0266 | 0.0005 | 0.072 | 0.0488 | 0.0021 | 167 | 7 | 169 | 3 | 47.00 | 0.64 | 0.049 | 0.002 | 0.28 |
| SNM42-9Mz-2 | 5455 | 140,500 | 25.76 | 0.250 | 0.013 | 0.0270 | 0.0005 | 0.194 | 0.0663 | 0.0031 | 228 | 11 | 172 | 3 | 80.00 | 0.66 | 0.066 | 0.003 | 0.12 |
| SNM42-9Mz-3 | 7100 | 140,200 | 19.75 | 0.180 | 0.008 | 0.0271 | 0.0005 | 0.085 | 0.0468 | 0.0017 | 167 | 7 | 172 | 3 | 47.00 | 0.61 | 0.047 | 0.002 | 0.24 |
| SNM422-3mz-1 | 6980 | 226,000 | 32.38 | 0.181 | 0.007 | 0.0268 | 0.0005 | 0.197 | 0.0481 | 0.0016 | 169 | 6 | 170 | 3 | 27.00 | 0.70 | 0.048 | 0.002 | 0.27 |
| SNM422-3mz-2 | 8050 | 173,400 | 21.54 | 0.181 | 0.007 | 0.0267 | 0.0005 | 0.249 | 0.0489 | 0.0015 | 169 | 6 | 170 | 3 | 40.00 | 0.72 | 0.049 | 0.002 | 0.19 |
| SNM422-3mz-3 | 6190 | 139,000 | 22.46 | 0.182 | 0.008 | 0.0268 | 0.0005 | 0.064 | 0.0489 | 0.0019 | 170 | 7 | 171 | 3 | 47.00 | 0.74 | 0.049 | 0.002 | 0.44 |
| SNM422-3mz-4 | 14,840 | 117,600 | 7.92 | 0.180 | 0.008 | 0.0265 | 0.0005 | 0.088 | 0.0491 | 0.0018 | 167 | 6 | 169 | 3 | 39.00 | 0.67 | 0.049 | 0.002 | 0.31 |
| SNM422-8mz-1 | 9830 | 127,300 | 12.95 | 0.178 | 0.008 | 0.0266 | 0.0005 | 0.205 | 0.0474 | 0.0021 | 166 | 7 | 169 | 3 | 53.00 | 0.75 | 0.047 | 0.002 | 0.13 |
| SNM422-8mz-2 | 7350 | 156,600 | 21.31 | 0.177 | 0.007 | 0.0262 | 0.0006 | 0.060 | 0.0480 | 0.0018 | 166 | 6 | 167 | 4 | 42.00 | 0.83 | 0.048 | 0.002 | 0.44 |
| SNM422-8mz-3 | 7170 | 111,900 | 15.61 | 0.180 | 0.011 | 0.0267 | 0.0005 | 0.024 | 0.0483 | 0.0030 | 168 | 9 | 170 | 3 | 48.00 | 0.69 | 0.048 | 0.003 | 0.39 |
| SNM422-8mz-4 | 6930 | 118,500 | 17.10 | 0.183 | 0.008 | 0.0268 | 0.0005 | 0.296 | 0.0491 | 0.0016 | 171 | 7 | 171 | 3 | 36.00 | 0.65 | 0.049 | 0.002 | 0.10 |
| SNM422-9mz-1 | 6027 | 238,600 | 39.59 | 0.174 | 0.006 | 0.0259 | 0.0004 | 0.194 | 0.0474 | 0.0013 | 162 | 5 | 165 | 3 | 30.00 | 0.63 | 0.047 | 0.001 | 0.26 |
| SNM422-9mz-2 | 7940 | 186,300 | 23.46 | 0.175 | 0.007 | 0.0264 | 0.0005 | 0.114 | 0.0472 | 0.0015 | 165 | 6 | 168 | 3 | 41.00 | 0.65 | 0.047 | 0.002 | 0.29 |
| SNM422-9mz-3 | 4030 | 121,700 | 30.20 | 0.190 | 0.014 | 0.0282 | 0.0005 | 0.297 | 0.0487 | 0.0030 | 176 | 11 | 179 | 3 | 61.00 | 0.59 | 0.049 | 0.003 | 0.02 |
| SNM422-9mz-4 | 8320 | 153,400 | 18.44 | 0.192 | 0.008 | 0.0280 | 0.0005 | 0.253 | 0.0489 | 0.0017 | 178 | 7 | 178 | 3 | 52.00 | 0.61 | 0.049 | 0.002 | 0.08 |

**Table 9** (continued)

| Comments | U (ppm) | Th (ppm) | Th/U | 207Pb/235U | 2σ | 206Pb/238U | 2σ | Err. corr. | 207Pb/206Pb | 2σ | 207Pb/235U | 2σ | 206Pb/238U | 2σ | 238U/206Pb | 2σ | 207Pb/206Pb | 2σ | Err. corr. |
|---|---|---|---|---|---|---|---|---|---|---|---|---|---|---|---|---|---|---|---|
| SNM422-9mz-5 | 8900 | 149,500 | 16.80 | 0.184 | 0.009 | 0.0271 | 0.0005 | 0.213 | 0.0486 | 0.0018 | 171 | 8 | 173 | 3 | 34.00 | 0.65 | 0.049 | 0.002 | 0.14 |
| SNM422-10mz-1 | 8090 | 170,400 | 21.06 | 0.184 | 0.008 | 0.0274 | 0.0006 | 0.147 | 0.0472 | 0.0019 | 171 | 7 | 174 | 4 | 48.00 | 0.73 | 0.047 | 0.002 | 0.28 |
| SNM422-10mz-2 | 7040 | 269,500 | 38.28 | 0.176 | 0.007 | 0.0267 | 0.0005 | 0.026 | 0.0475 | 0.0017 | 165 | 6 | 170 | 3 | 38.00 | 0.66 | 0.048 | 0.002 | 0.40 |
| SNM422-10mz-3 | 8720 | 291,400 | 33.42 | 0.186 | 0.009 | 0.0272 | 0.0005 | 0.008 | 0.0493 | 0.0021 | 173 | 8 | 173 | 3 | 45.00 | 0.69 | 0.049 | 0.002 | 0.40 |

In active continental margins, the cause of melting could be mafic mantle-derived magmas, partly mixed with produced S-type magmas. The produced S-type silicic magmas slightly post-date mafic magmas in a subduction zone (e.g., Christiansen and Keith 1996). Our obtained U–Pb ages for aplites and pegmatites (162–172 Ma) reveal that ages of plutonic rocks of the region (~165 Ma; Shahbazi et al. 2010; Mahmoudi et al. 2011; Chiu et al. 2013) are nearly similar to the studied aplitic–pegmatitic rocks. Therefore, aplites and pegmatites can be related chronologically to plutonic rocks, namely S-type granitoids. On the other hand, mafic plutons have nearly the same age as S-type granitoids and, therefore, mafic plutons may have acted as heat source for melting of meta-sedimentary rocks to form S-type plutons and associated aplites and pegmatites. Also, from other adjacent areas, such as Boroujerd and Aligoudarz areas (e.g., Ahmadi-Khalaji et al. 2007; Esna-Ashari et al. 2012), similar ages have been reported. They are mostly related to Middle Jurassic magmatism. On the other hand, some late Jurassic ages were obtained by previous researchers (e.g., Shahbazi et al. 2010; Mahmoudi et al. 2011; Azizi et al. 2011, 2015; Yajam et al. 2015) for the Hamedan region and adjacent areas, such as Qorveh. This means that Middle to Late Jurassic magmatism (especially granitic magmatism and associated pegmatite-aplite dykes) constitutes an important magmatic episode in the region.

It is most likely that repetitive injections of precursor mafic magmas (ca.167 Ma) have been so important to cause melting of fertile supracrustal lithologies (i.e., metapelites) to form migmatites, diatexites, S-type granites (ca. 165 Ma), and related aplite–pegmatite dykes in the region (e.g., Sepahi 1999, 2008). The signatures of these hot mafic magmas are a spectrum of mafic plutonic rocks, such as olivine-gabbros, gabbros, and diorites that are near granites and partly intruded by later intrusion of granitic and aplitic–pegmatitic dykes. Therefore, advective heating in a continental arc setting can explain the formation of felsic rocks, such as the studied aplite–pegmatite dykes and their parental evolved granitic rocks. Models by Annen and Sparks (2002) could be helpful for proving of melting of fertile rocks in a continental crust by intrusions of mafic (basaltic/gabbroic) magmas. According to Karakas et al. (2017), when basaltic magma is emplaced in the lower crust, a significant increase of temperature occurs within the whole crust after a few million years to generate upper crustal felsic magmas. The total duration of lower and upper crustal magmatism can be between 1.5 and 7 million years which is consistent with our geochronological data.

Hybridism of newly formed felsic magmas with continuing injections of mafic magmas may have occurred in this environment. Signs of this hybridism are reported by Sepahi (1999) and Ghalamghash et al. (2009) in the Alvand intrusive complex.

**Table 10** U–Pb LA-ICPMS data of analyzed monazite grains from the Barfejin area, west of Hamedan

| Comments | U (ppm) | Th (ppm) | Th/U | 207Pb/235U | 2σ | 206Pb/238U | 2σ | Err. corr. | 207Pb/206Pb | 2σ | 207Pb/235U | 2σ | 206Pb/238U | 2σ | 238U/206Pb | 2σ | 207Pb/206Pb | 2σ | Err. corr. |
|---|---|---|---|---|---|---|---|---|---|---|---|---|---|---|---|---|---|---|---|
| Bar1-4mz-1 | 6045 | 71,720 | 11.86 | 0.180 | 0.010 | 0.0254 | 0.0005 | 0.055 | 0.0513 | 0.0023 | 168 | 9 | 162 | 3 | 43.00 | 0.81 | 0.051 | 0.002 | 0.49 |
| Bar1-5mz-1 | 2060 | 79,500 | 38.59 | 0.182 | 0.007 | 0.0262 | 0.0004 | 0.153 | 0.0501 | 0.0016 | 170 | 6 | 167 | 3 | 30.00 | 0.63 | 0.050 | 0.002 | 0.25 |
| Bar1-5mz-2 | 5150 | 64,340 | 12.49 | 0.185 | 0.008 | 0.0267 | 0.0006 | 0.033 | 0.0504 | 0.0019 | 172 | 6 | 170 | 4 | 71.00 | 0.82 | 0.050 | 0.002 | 0.40 |
| Bar1-6mz-1 | 22 | 1800 | 81.82 | 0.413 | 0.061 | 0.0370 | 0.0031 | 0.551 | 0.0796 | 0.0090 | 324 | 37 | 233 | 19 | 130.00 | 2.26 | 0.080 | 0.009 | 0.02 |
| Bar1-6mz-3 | 6380 | 89,800 | 14.08 | 0.179 | 0.007 | 0.0261 | 0.0004 | 0.326 | 0.0492 | 0.0015 | 167 | 6 | 166 | 3 | 36.00 | 0.65 | 0.049 | 0.002 | 0.06 |
| Bar1-6mz-4 | 3996 | 86,900 | 21.75 | 0.173 | 0.007 | 0.0259 | 0.0005 | 0.259 | 0.0485 | 0.0016 | 162 | 6 | 165 | 3 | 36.00 | 0.67 | 0.049 | 0.002 | 0.15 |
| Bar1-8mz-1 | 5512 | 81,200 | 14.73 | 0.197 | 0.009 | 0.0263 | 0.0006 | 0.007 | 0.0541 | 0.0022 | 183 | 8 | 167 | 4 | 41.00 | 0.81 | 0.054 | 0.002 | 0.47 |
| Bar1-9mz-1 | 5680 | 86,200 | 15.18 | 0.175 | 0.008 | 0.0261 | 0.0005 | 0.084 | 0.0489 | 0.0019 | 164 | 7 | 166 | 3 | 44.00 | 0.68 | 0.049 | 0.002 | 0.26 |
| Bar1-10mz-2 | 5369 | 86,500 | 16.11 | 0.178 | 0.009 | 0.0263 | 0.0005 | 0.193 | 0.0493 | 0.0022 | 167 | 8 | 167 | 3 | 42.00 | 0.65 | 0.049 | 0.002 | 0.11 |
| Bar1-10mz-3 | 6400 | 89,100 | 13.92 | 0.176 | 0.008 | 0.0265 | 0.0005 | 0.124 | 0.0472 | 0.0019 | 164 | 7 | 169 | 3 | 64.00 | 0.77 | 0.047 | 0.002 | 0.35 |
| Bar1-11mz-2 | 6940 | 104,400 | 15.04 | 0.174 | 0.008 | 0.0254 | 0.0005 | 0.120 | 0.0490 | 0.0021 | 163 | 7 | 162 | 3 | 42.00 | 0.70 | 0.049 | 0.002 | 0.24 |
| Bar1-11mz-3 | 6415 | 100,400 | 15.65 | 0.180 | 0.008 | 0.0262 | 0.0005 | 0.026 | 0.0495 | 0.0019 | 168 | 7 | 167 | 3 | 35.00 | 0.68 | 0.050 | 0.002 | 0.31 |
| Bar1-12mz-1 | 6800 | 90,900 | 13.37 | 0.167 | 0.008 | 0.0254 | 0.0005 | 0.055 | 0.0475 | 0.0020 | 157 | 7 | 161 | 3 | 47.00 | 0.73 | 0.048 | 0.002 | 0.30 |
| Bar1-12mz-3 | 7460 | 101,100 | 13.55 | 0.182 | 0.008 | 0.0268 | 0.0005 | 0.006 | 0.0493 | 0.0020 | 170 | 7 | 170 | 3 | 50.00 | 0.74 | 0.049 | 0.002 | 0.41 |
| Bar11-1mz-1 | 3940 | 67,100 | 17.03 | 0.172 | 0.008 | 0.0258 | 0.0005 | 0.184 | 0.0473 | 0.0019 | 161 | 7 | 164 | 3 | 42.00 | 0.72 | 0.047 | 0.002 | 0.19 |
| Bar11-1mz-2 | 5870 | 82,900 | 14.12 | 0.174 | 0.007 | 0.0254 | 0.0004 | 0.158 | 0.0492 | 0.0015 | 163 | 6 | 162 | 3 | 36.00 | 0.68 | 0.049 | 0.002 | 0.27 |
| Bar11-4mz-1 | 5320 | 91,600 | 17.22 | 0.174 | 0.008 | 0.0256 | 0.0005 | 0.005 | 0.0489 | 0.0021 | 163 | 7 | 163 | 3 | 40.00 | 0.71 | 0.049 | 0.002 | 0.32 |
| Bar11-4mz-2 | 1392 | 85,500 | 61.42 | 0.174 | 0.008 | 0.0251 | 0.0004 | 0.024 | 0.0496 | 0.0021 | 163 | 7 | 160 | 3 | 48.00 | 0.70 | 0.050 | 0.002 | 0.35 |
| Bar11-5mz-1 | 6770 | 96,600 | 14.27 | 0.170 | 0.008 | 0.0256 | 0.0005 | 0.106 | 0.0479 | 0.0018 | 159 | 7 | 163 | 3 | 39.00 | 0.72 | 0.048 | 0.002 | 0.33 |
| Bar11-5mz-2 | 6440 | 90,900 | 14.11 | 0.174 | 0.007 | 0.0254 | 0.0004 | 0.143 | 0.0493 | 0.0017 | 163 | 6 | 161 | 3 | 38.00 | 0.67 | 0.049 | 0.002 | 0.24 |
| Bar11-5mz-3 | 7147 | 104,500 | 14.62 | 0.191 | 0.008 | 0.0260 | 0.0005 | 0.160 | 0.0521 | 0.0018 | 178 | 7 | 165 | 3 | 44.00 | 0.68 | 0.052 | 0.002 | 0.25 |
| Bar11-5mz-4 | 11,710 | 78,000 | 6.66 | 0.172 | 0.007 | 0.0252 | 0.0004 | 0.093 | 0.0483 | 0.0016 | 161 | 6 | 160 | 3 | 37.00 | 0.63 | 0.048 | 0.002 | 0.25 |

**Table 10** (continued)

| Comments | U (ppm) | Th (ppm) | Th/U | 207Pb/235U | 2σ | 206Pb/238U | 2σ | Err. corr. | 207Pb/206Pb | 2σ | 207Pb/235U | 2σ | 206Pb/238U | 2σ | 238U/206Pb | 2σ | 207Pb/206Pb | 2σ | Err. corr. |
|---|---|---|---|---|---|---|---|---|---|---|---|---|---|---|---|---|---|---|---|
| Bar11-6mz-1 | 13.81 | 4.05 | 0.29 | 0.178 | 0.008 | 0.0263 | 0.0005 | 0.058 | 0.0482 | 0.0020 | 166 | 7 | 168 | 3 | 45.00 | 0.66 | 0.048 | 0.002 | 0.25 |
| Bar11-6mz-2 | 23.2 | 17.2 | 0.74 | 0.173 | 0.009 | 0.0252 | 0.0005 | 0.195 | 0.0500 | 0.0023 | 162 | 8 | 160 | 3 | 47.00 | 0.74 | 0.050 | 0.002 | 0.20 |
| Bar11-6mz-3 | 6140 | 93,900 | 15.29 | 4.710 | 0.650 | 0.053 | 0.007 | 0.410 | 0.6500 | 0.3100 | 1740 | 120 | 332 | 41 | 140.00 | 2.35 | 0.650 | 0.310 | 0.73 |
| Bar11-6mz-4 | 7150 | 107,900 | 15.09 | 8.220 | 0.860 | 0.090 | 0.009 | 0.755 | 0.7070 | 0.0710 | 2199 | 99 | 551 | 53 | 87.00 | 1.12 | 0.707 | 0.071 | 0.49 |
| Bar11-7mz-1 | 6630 | 96,400 | 14.54 | 14.000 | 1.600 | 0.140 | 0.021 | 0.527 | 0.6900 | 0.5500 | 2720 | 120 | 820 | 110 | 130.00 | 1.07 | 0.690 | 0.550 | 0.85 |
| Bar11-7mz-2 | 6020 | 85,200 | 14.15 | 7.850 | 0.920 | 0.091 | 0.009 | 0.008 | 0.8200 | 0.1700 | 2150 | 110 | 558 | 55 | 170.00 | 1.13 | 0.820 | 0.170 | 0.90 |
| Bar11-7mz-3 | 37.7 | 3.16 | 0.08 | 0.254 | 0.023 | 0.027 | 0.001 | 0.168 | 0.0675 | 0.0048 | 229 | 15 | 172 | 3 | 41.00 | 0.74 | 0.068 | 0.005 | 0.21 |
| Bar11-7mz-4 | 34.9 | 3.56 | 0.10 | 0.221 | 0.022 | 0.027 | 0.001 | 0.173 | 0.0596 | 0.0034 | 204 | 16 | 170 | 5 | 39.00 | 1.17 | 0.060 | 0.003 | 0.21 |
| Bar11-8mz-1 | 8570 | 102,400 | 11.95 | 0.171 | 0.007 | 0.0259 | 0.0005 | 0.062 | 0.0470 | 0.0017 | 160 | 6 | 165 | 3 | 30.00 | 0.67 | 0.047 | 0.002 | 0.27 |
| Bar11-8mz-2 | 8370 | 87,700 | 10.48 | 0.227 | 0.023 | 0.027 | 0.001 | 0.468 | 0.0597 | 0.0047 | 207 | 17 | 172 | 3 | 92.00 | 0.71 | 0.060 | 0.005 | −0.13 |
| Bar11-8mz-3 | 8400 | 79,700 | 9.49 | 0.170 | 0.007 | 0.0254 | 0.0004 | 0.269 | 0.0478 | 0.0016 | 159 | 6 | 162 | 3 | 36.00 | 0.68 | 0.048 | 0.002 | 0.09 |
| Bar11-8mz-4 | 8837 | 93,600 | 10.59 | 0.174 | 0.011 | 0.0248 | 0.0006 | 0.167 | 0.0500 | 0.0024 | 162 | 9 | 158 | 4 | 54.00 | 1.03 | 0.050 | 0.002 | 0.34 |
| Bar11-9mz-1 | 4406 | 78,000 | 17.70 | 0.175 | 0.009 | 0.0258 | 0.0005 | 0.330 | 0.0491 | 0.0023 | 164 | 8 | 164 | 3 | 52.00 | 0.75 | 0.049 | 0.002 | 0.05 |
| Bar11-9mz-2 | 6219 | 78,900 | 12.69 | 5.640 | 0.360 | 0.155 | 0.008 | 0.920 | 0.2594 | 0.0076 | 1908 | 88 | 927 | 48 | 29.00 | 0.35 | 0.259 | 0.008 | 0.02 |
| Bar11-12mz-1 | 5629 | 80,100 | 14.23 | 0.203 | 0.010 | 0.026 | 0.000 | 0.122 | 0.0557 | 0.0025 | 188 | 8 | 166 | 3 | 47.00 | 0.70 | 0.056 | 0.003 | 0.25 |
| Bar11-12mz-2 | 7770 | 98,700 | 12.70 | 0.175 | 0.008 | 0.0261 | 0.0005 | 0.188 | 0.0489 | 0.0019 | 164 | 7 | 166 | 3 | 37.00 | 0.75 | 0.049 | 0.002 | 0.26 |
| Bar11-12mz-3 | 402,000 | 98,800 | 0.25 | 4.040 | 0.880 | 0.082 | 0.013 | 0.506 | 0.4700 | 0.1500 | 1450 | 160 | 501 | 74 | 200.00 | 1.93 | 0.470 | 0.150 | 0.71 |

**Table 11** U–Pb LA-ICPMS data of analyzed zircon grains from the Heydareh-e-Poshteshar area, west of Hamedan

| Comments | U (ppm) | Th (ppm) | Th/U | 207Pb/235U | 2σ | 206Pb/238U | 2σ | Err. corr. | 207Pb/206Pb | 2σ | 207Pb/206Pb | 2σ | 207Pb/235U | 2σ | 206Pb/238U | 2σ | 238U/206Pb | 2σ | 207Pb/206Pb | 2σ | Err. corr. |
|---|---|---|---|---|---|---|---|---|---|---|---|---|---|---|---|---|---|---|---|---|---|
| SNM4-1-13-zr-1 | 1981 | 43.6 | 0.02 | 0.179 | 0.015 | 0.026 | 0.001 | 0.207 | 0.0509 | 0.0026 | 215 | 78 | 167 | 13 | 165 | 6 | 38.65 | 1.49 | 0.051 | 0.003 | 0.18 |
| SNM4-1Zr-1 | 1922 | 82 | 0.04 | 0.196 | 0.014 | 0.026 | 0.001 | 0.180 | 0.0550 | 0.0017 | 395 | 45 | 181 | 12 | 165 | 7 | 38.62 | 1.49 | 0.055 | 0.002 | 0.32 |
| SNM4-1-11-zr-1 | 3540 | 304 | 0.09 | 0.187 | 0.012 | 0.024 | 0.001 | 0.321 | 0.0566 | 0.0013 | 474 | 36 | 174 | 10 | 154 | 6 | 41.49 | 1.72 | 0.057 | 0.001 | 0.16 |
| SNM4-2-8Zr-1 | 2835 | 388 | 0.14 | 0.246 | 0.020 | 0.024 | 0.001 | 0.364 | 0.0740 | 0.0034 | 1046 | 76 | 224 | 15 | 152 | 6 | 41.98 | 1.67 | 0.074 | 0.003 | 0.02 |
| SNM4-2-13ZrMz-1 | 1602 | 50.5 | 0.03 | 0.194 | 0.020 | 0.026 | 0.001 | 0.294 | 0.0533 | 0.0034 | 368 | 98 | 180 | 16 | 165 | 7 | 38.52 | 1.63 | 0.053 | 0.003 | 0.08 |
| SNM4-9Zr-1 | 4369 | 1627 | 0.37 | 0.250 | 0.034 | 0.020 | 0.001 | 0.216 | 0.0899 | 0.0070 | 1435 | 77 | 227 | 23 | 125 | 6 | 50.99 | 2.34 | 0.090 | 0.007 | 0.59 |
| SNM4-1-15-Zr-1_x | 3040 | 1550 | 0.51 | 0.671 | 0.069 | 0.036 | 0.003 | 0.716 | 0.1334 | 0.0078 | 2120 | 110 | 518 | 44 | 229 | 17 | 27.55 | 2.12 | 0.133 | 0.008 | −0.14 |
| SNM4-1-7-zr-1 | 3840 | 1080 | 0.28 | 0.217 | 0.360 | 0.020 | 0.008 | 0.328 | 0.0794 | 0.0230 | 1160 | 190 | 199 | 100 | 127 | 45 | 50.30 | 19.74 | 0.079 | 0.023 | 0.75 |
| SNM4-5Zr-1_x | 10,100 | 13,000 | 1.29 | 29.800 | 4.000 | 0.399 | 0.058 | 0.470 | 0.5990 | 0.0570 | 4530 | 110 | 3510 | 140 | 2110 | 260 | 2.51 | 0.36 | 0.599 | 0.057 | 0.39 |

Data obtained by K–Ar and Rb–Sr dating (both for pegmatites and related plutonic rocks by previous researchers, e.g., Valizadeh and Cantagrel 1975; Braud 1987; Masoudi 1997; Baharifar et al. 2004), are relatively close to each other, but they are younger than U–Pb ages estimated in previous research and those measured in this study. These younger ages may be the resultof re-heating of the region by later tectono-magmatic activity, and they do not show ages consistent with primary crystallization of those rocks. On the basis of these old data, previous researchers (e.g., Sepahi 2008) postulated a Cretaceous magmatic–metamorphic event in the region. However, recent data have indicated more possible Jurassic magmatic and metamorphic activities in the region. Metamorphic ages of zircon also give nearly similar ages as plutonic rocks (unpublished data).

On the basis of these geochronologic results and comparing them with previous published data, the geodynamic-magmatic evolution of the Sanandaj–Sirjan zone can be summarized as follows: Agard et al. (2011) have reviewed this subject, but they have not considered any important role for middle Jurassic magmatism (plutonism) in the region in their conclusions. They considered the time interval of subduction/obduction processes from ~150 Ma to present time (especially from ~115 Ma). Recent studies and our results revealed that this zone has been an active continental margin during the Jurassic (from nearly ~170 Ma ago) and eventually evolved to a continent–continent collision setting (Afro-Arabian to Eurasia collision) later. On the basis of data obtained in recent work and this research, the volume of Jurassic magmatism (plutonism) has been enormous, especially in the middle Jurassic within this zone. Various plutonic rocks, from mafic to intermediate and felsic, resulted from successive magmatic activity in the region. Therefore, subduction of Neo-Tethys oceanic crust beneath central Iran must have started sooner than those considered previously and took place over a wider time range (starting from middle Jurassic time, i.e., from ~170 Ma or slightly older). Tectono-magmatic events related to opening and closure of Neo-Tethys ocean in the region can be summarized as follows (Fig. 18): (a) break-off of Gondwana that resulted in the opening of Neo-Tethys ocean took place at Permian time by granitic magmatism [i.e., Hasanrobat pluton (Alirezaei and Hassanzadeh 2012)], (b) spreading of the oceanic crust was continued during Triassic to lower Jurassic, (c) beginning of subduction and onset of continental arc magmatism were started from middle Jurassic time by intense plutonism in the region and continued by late Jurassic and younger times, and (d) collision of Afro-Arabia and Iranian microplate (Eurasian southern margin) possibly in Oligo-Miocene time.

**Table 12** U–Pb LA-ICPMS data of analyzed allanite grains from the Artiman area, Tueyserkan, south of Hamedan

| Comments | U (ppm) | Th (ppm) | Th/U | 207Pb/235U | 2σ | 206Pb/238U | 2σ | Err. corr. | 207Pb/206Pb | 2σ | 207Pb/206Pb | 2σ | 207Pb/235U | 2σ | 206Pb/238U | 2σ | 238U/206Pb | 2σ | 207Pb/206Pb | 2σ | Err. corr. |
|---|---|---|---|---|---|---|---|---|---|---|---|---|---|---|---|---|---|---|---|---|---|
| Art19-Alln1-1 | 416.1 | 5189 | 12.47 | 0.600 | 0.290 | 0.031 | 0.002 | 0.900 | −0.0500 | 0.1800 | 3110 | 260 | 580 | 250 | 260 | 150 | 18.59 | 0.45 | 0.485 | 0.012 | 0.61 |
| Art19-Alln2-1 | 798.6 | 7050 | 8.83 | 2.680 | 0.580 | 0.129 | 0.010 | 0.803 | 0.1490 | 0.0350 | 2760 | 220 | 1340 | 170 | 220 | 160 | 3.40 | 0.20 | 0.703 | 0.008 | −0.21 |
| Art19_alln-1 | 617.4 | 7990 | 12.94 | 0.230 | 0.170 | 0.026 | 0.002 | 0.879 | −0.0020 | 0.0460 | 2620 | 280 | 130 | 250 | 280 | 150 | 25.50 | 0.61 | 0.352 | 0.010 | 0.10 |
| Art19_alln-2_mixed | 487.5 | 7420 | 15.22 | 0.530 | 0.270 | 0.027 | 0.002 | 0.898 | 1.3000 | 1.7000 | 3270 | 210 | 580 | 200 | 210 | 130 | 23.47 | 0.66 | 0.460 | 0.014 | 0.35 |
| Art19_alln-3 | 743.1 | 11,038 | 14.85 | 0.690 | 0.310 | 0.044 | 0.003 | 0.861 | 0.0610 | 0.0570 | 2840 | 280 | 430 | 240 | 280 | 180 | 10.82 | 0.35 | 0.589 | 0.010 | 0.12 |
| Art19_alln-5 | 390.1 | 7710 | 19.76 | 0.137 | 0.006 | 0.022 | 0.001 | 1.000 | 0.0079 | 0.0003 | 2 | 1 | 132 | 138 | 9 | 159 | 26.25 | 0.67 | 0.377 | 0.013 | 0.47 |
| Art19_alln-6 | 616.9 | 8420 | 13.65 | 0.130 | 0.200 | 0.025 | 0.002 | 0.886 | 0.0100 | 0.0620 | 2540 | 250 | 20 | 520 | 250 | 230 | 28.44 | 0.72 | 0.297 | 0.008 | 0.59 |
| Art19_alln-7 | 531.2 | 8770 | 16.51 | 0.159 | 0.004 | 0.025 | 0.001 | 0.997 | 0.0080 | 0.0003 | 2 | 0 | 150 | 159 | 5 | 161 | 34.07 | 0.72 | 0.159 | 0.007 | 0.43 |
| Art19_alln-8 | 687.3 | 8880 | 12.92 | 0.170 | 0.160 | 0.026 | 0.002 | 0.887 | 0.0270 | 0.0440 | 2430 | 220 | 180 | 260 | 220 | 150 | 30.40 | 0.67 | 0.234 | 0.008 | 0.45 |
| Art19_alln-9 | 210.4 | 8980 | 42.68 | 0.161 | 0.007 | 0.025 | 0.001 | 1.000 | 0.0080 | 0.0003 | 2 | 0 | 152 | 161 | 7 | 162 | 29.41 | 0.86 | 0.259 | 0.014 | 0.33 |
| Art19_alln-10 | 196.7 | 8930 | 45.40 | −0.010 | 0.540 | 0.028 | 0.005 | 0.951 | 0.1000 | 0.4000 | 3690 | 420 | 850 | 410 | 420 | 190 | 17.24 | 0.51 | 0.479 | 0.017 | 0.30 |
| Art19_alln-11 | 209.1 | 9820 | 46.96 | −0.060 | 0.530 | 0.026 | 0.004 | 0.942 | −0.1000 | 0.4300 | 3900 | 330 | 730 | 330 | 330 | 240 | 20.37 | 0.66 | 0.452 | 0.018 | 0.48 |
| Art19_alln-12 | 749.5 | 10,200 | 13.61 | 0.161 | 0.003 | 0.025 | 0.001 | 0.997 | 0.0081 | 0.0003 | 2 | 0 | 152 | 161 | 3 | 163 | 36.35 | 0.69 | 0.110 | 0.004 | 0.46 |
| Art19_alln-13 | 694 | 10,780 | 15.53 | 0.210 | 0.250 | 0.030 | 0.002 | 0.923 | 0.0190 | 0.0800 | 2850 | 250 | 220 | 280 | 250 | 250 | 19.12 | 0.95 | 0.437 | 0.014 | 0.12 |
| Art19_alln-14 | 500.2 | 7770 | 15.53 | −0.150 | 0.330 | 0.036 | 0.004 | 0.843 | −0.0900 | 0.0760 | 2800 | 260 | 350 | 420 | 260 | 270 | 11.56 | 1.23 | 0.573 | 0.015 | −0.08 |
| Art19_alln-15 | 236.8 | 6394 | 27.00 | 0.420 | 0.430 | 0.028 | 0.003 | 0.900 | 0.0800 | 0.2100 | 3930 | 210 | 640 | 240 | 210 | 200 | 18.08 | 0.49 | 0.580 | 0.018 | 0.61 |
| Art19_alln-16 | 267.1 | 8750 | 32.76 | 0.179 | 0.007 | 0.028 | 0.001 | 0.993 | 0.0083 | 0.0003 | 1 | 0 | 167 | 178 | 7 | 167 | 21.37 | 0.55 | 0.352 | 0.012 | 0.48 |
| Art19_alln-17 | 773 | 13,510 | 17.48 | 49.300 | 1.500 | 0.623 | 0.014 | 0.868 | 0.5683 | 0.0150 | 4433 | 31 | 3979 | 20 | 31 | 25 | 0.94 | 0.01 | 0.771 | 0.007 | 0.40 |
| Art19_alln2-1 | 409.7 | 2889 | 7.05 | 0.160 | 0.300 | 0.033 | 0.003 | 0.903 | −0.0700 | 0.0910 | 3000 | 210 | 420 | 250 | 210 | 190 | 15.75 | 0.55 | 0.497 | 0.013 | 0.48 |
| Art19_alln2-2 | 571.4 | 4590 | 8.03 | 0.590 | 0.270 | 0.032 | 0.002 | 0.894 | 0.0860 | 0.0630 | 3130 | 280 | 610 | 230 | 280 | 150 | 16.98 | 1.07 | 0.508 | 0.014 | −0.10 |
| Art19_alln2-3 | 610.2 | 5415 | 8.87 | 0.370 | 0.300 | 0.041 | 0.003 | 0.775 | 0.0460 | 0.0560 | 2680 | 270 | 520 | 240 | 270 | 170 | 10.74 | 0.39 | 0.601 | 0.009 | −0.11 |
| Art19_alln2-4 | 296.9 | 2753 | 9.27 | 1.390 | 0.680 | 0.075 | 0.005 | 0.813 | 0.0980 | 0.0740 | 3350 | 240 | 1190 | 220 | 240 | 190 | 5.71 | 0.12 | 0.686 | 0.013 | 0.43 |
| Art19_alln2-5 | 573.5 | 6590 | 11.49 | 1.410 | 0.420 | 0.099 | 0.005 | 0.697 | 0.0900 | 0.0370 | 2780 | 270 | 950 | 280 | 270 | 270 | 4.39 | 0.21 | 0.679 | 0.012 | 0.32 |
| Art19_alln2-6 | 466.2 | 3748 | 8.04 | 0.500 | 0.270 | 0.031 | 0.002 | 0.913 | 0.0300 | 0.0880 | 3230 | 250 | 360 | 330 | 250 | 250 | 19.12 | 0.80 | 0.475 | 0.013 | 0.66 |
| Art19_alln2-7 | 430 | 3487 | 8.11 | 0.470 | 0.420 | 0.055 | 0.004 | 0.903 | 0.0000 | 0.0690 | 3140 | 240 | 870 | 290 | 240 | 270 | 7.64 | 0.28 | 0.638 | 0.011 | 0.48 |

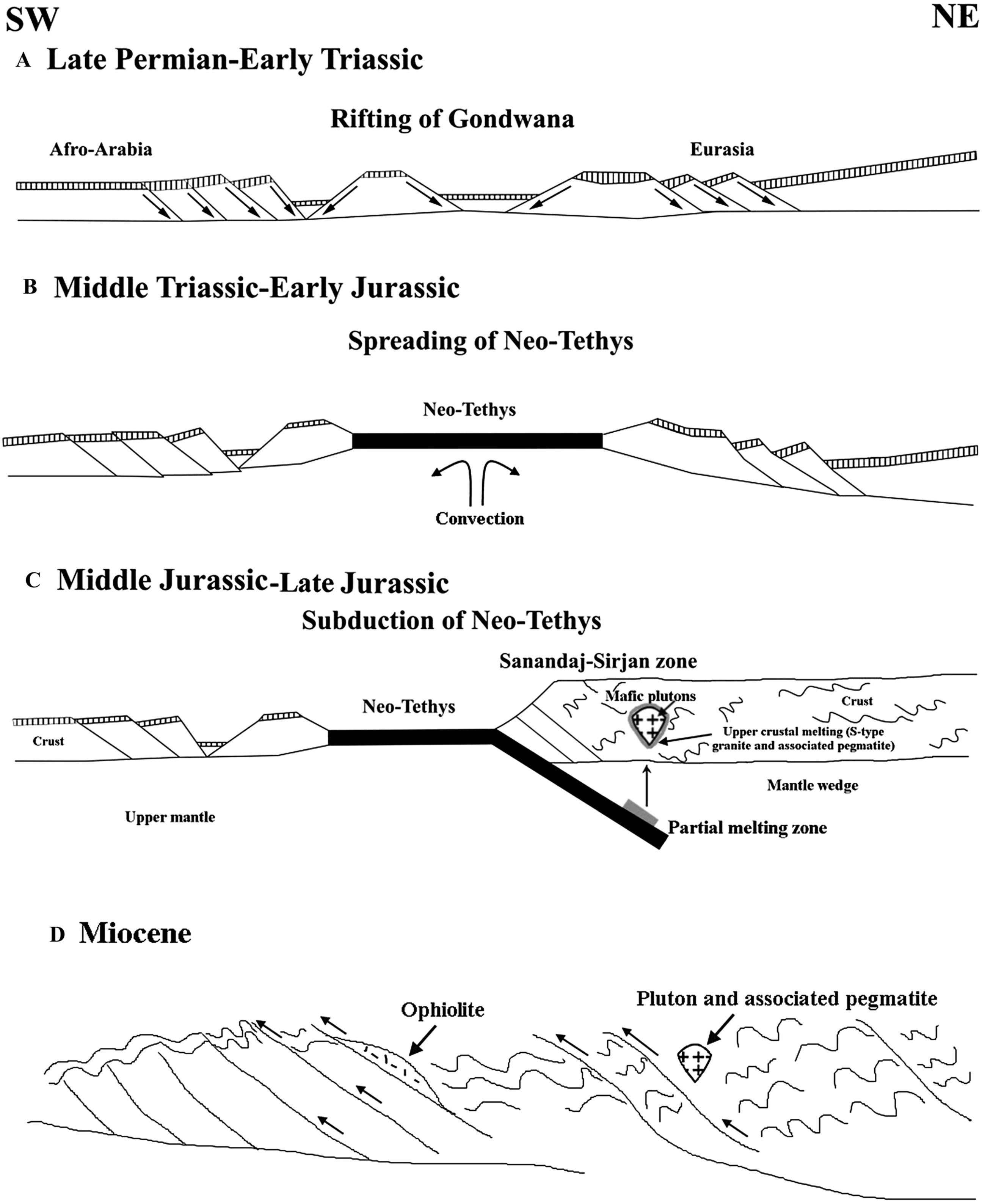

**Fig. 18** Schematic cross-section along the Zagros orogen, showing the tectonic evolution in Late Permian to Middle Jurassic and Miocene (Modified from Ahmadi-Khalaji et al. 2007)

## Concluding remarks

Pegmatitic and aplitic dykes intrude both plutonic rocks of the Alvand complex and surrounding regional and contact metamorphic rocks. Mineral-chemical studies of aplitic–pegmatitic rocks indicate that tourmaline composition is commonly schorl, garnet is Fe-rich (almandine), biotite is near siderophyllite, white mica is nearly pure muscovite, K-feldspar is Na- and Ca-poor feldspar, and plagioclase is albitic (Na-rich and Ca-poor) in composition. The geochemical and mineralogical characteristics of the studied aplites and pegmatites reveal high silica contents, low lime contents, high ASI index, and high amounts of alkali elements. The enrichment of LREE against HREE, high concentration of some REE and HFSE elements, such as Ce (up to 103 ppm), La (up to 125 ppm), Nb (up to 134 ppm), and LILE elements, such as Cs (up to 152 ppm), Ta (up to 67), Sn (>10,000 ppm), and K/Rb (19–193) reflects extreme fractionation. The occurrence of some accessory minerals, such as Th-silicate, U-silicate, U-oxides, Nb-oxide, zircon, allanite, phosphate minerals (monazite, xenotime, and apatite), beryl, and cassiterite, also emphasizes the highly fractionated nature of these peraluminous aplites and pegmatites; therefore, a highly evolved silicic magma led to formation of these dykes (see geochemistry section). On the basis of the pegmatite classification of Cerný and Ercit (2005), the studied pegmatites resemble LCT family of pegmatites, with mineralogical characteristics of Muscovite (MS) and Muscovite Rare Element (MS-REL) classes of pegmatites.

Our geochronological data indicate a middle Jurassic (~150 to ~170 Ma) age for the aplite and pegmatites of the Hamedan region, Sanandaj–Sirjan zone, which is consistent with ages obtained by previous researchers for plutonic rocks of the region. Therefore, our data reveal the importance of onset of magmatism within a continental arc setting from Middle Jurassic time in the region. The advective heat of largeamounts of mafic magmas (~167 Ma) into the continental crust associated with the magmatic arc has created diatexites and pluton-scale (batholithic) S-type granites (~165 Ma) of the region. Accordingly, fractionation of the S-type granitic magma at depth has produced some aplite–pegmatite dykes in the interior and margin of pluton, although some dykes appear exterior to the pluton, as well that are extensively fractionated locally to have beryl and cassiterite crystallization from these evolved melts; high B was significant to allowing extremely low T fractionation to occur in addition to the anomalous thermal gradient in the region.

Subduction of Neo-Tethys oceanic crust beneath central Iran (southern Eurasia), which started from about ~170 Ma or slightly older time in the region, has been the major cause of the magmatism in the region and adjacent areas in the Sanandaj–Sirjan zone of the Zagros orogen. During subduction, the heat advection associated with repetitive intrusion of mafic magmas has produced felsic magmas (S-type granites and associated aplites-pegmatites). This explains why mantle-derived mafic rocks and crustal-derived felsic rocks are nearly contemporaneous in the Hamedan region.

**Acknowledgements** David Lentz and Christopher McFarlane are each supported by a NSERC Discovery grant. We thank research office of Bu-Ali Sina University for providing part of the budget for geochemicaland microprobe analyses of this study.

## References

Abdel-Rahman AM (1994) Nature of biotites from alkaline, calc-alkaline and peraluminous magma. J Petrol 35:525–541

Agard P, Omrani J, Jolivet L, Whitechurch H, Vrielynck B, Spakman W, Monié P, Meyer B, Wortel R (2011) Zagros orogeny: a subduction-dominated process. Geol Mag 148:692–725

Ahadnejad V, Valizadeh MV, Deevsalar R, Rezaei-Kahkhaei M (2011) Age and geotectonic position of the Malayer granitoids: implication for plutonism in the Sanandaj–Sirjan zone, W Iran. Neues Jahrb Geol P-A 261:61–75

Ahmadi-Khalaji A, Esmaeily D, Valizadeh MV, Rahimpour-Bonab H (2007) Petrology and geochemistry of the granitoid complex of Boroujerd, Sanandaj–Sirjan zone, Western Iran. J Asian Earth Sci 29:859–877

Alavi M (1994) Tectonics of Zagros orogenic belt of Iran: new data and interpretation. Tectonophysics 229:211–238

Alavi M (2004) Regional stratigraphy of the Zagros fold-thrust belt of Iran and its proforeland evolution. Am J Sci 304:1–20

Alfonso P, Melgarejo JC, Yusta I, Velasco F (2003) Geochemistry of feldspars and muscovite in granitic pegmatite from the Cap de Creus field, Catalonia, Spain. Can Mineral 41:103–116

Aliani F, Maanijou M, Sabouri Z, Sepahi AA (2012) Petrology, geochemistry and geotectonic environment of the Alvand Intrusive Complex, Hamedan, Iran. Chem Erde-Geochem 72:363–383

Alirezaei S, Hassanzadeh J (2012) Geochemistry and zircon geochronology of the Permian A-type Hasanrobat granite, Sanandaj–Sirjan belt: a new record of the Gondwana break-up in Iran. Lithos 151:122–134

Anderson MO, Lentz DR, McFarlane CRM, Falck H (2013) A geological, geochemical and textural study of an LCT pegmatite: implications for the magmatic versus metasomatic origin of Nb-Ta mineralization in the Moose II pegmatite, Northwest Territories Canada. J Geosci 58:299–320

Annen C, Sparks RSJ (2002) Effects of repetitive emplacement of basaltic intrusions on thermal evolution and melt generation in the crust. Earth Planet Sci Lett 203:937–955

Arvin M, Pan Y, Dargahi S, Malekizadeh A, Babaei A (2007) Petrochemistry of the Siah-Kuh granitoid stock southwest of Kerman, Iran: implications for initiation of Neotethys subduction. J Asian Earth Sci 30:474–489

Azizi H, Asahara Y, Mehrabi B, Chung SL (2011) Geochronological and geochemical constraints on the petrogenesis of high-K granite from the Suffiabad area, Sanandaj–Sirjan Zone, NW Iran. Chem Erde Geochem 71:363–376

Azizi H, Zanjefili-Beiranvand M, Asahara Y (2015) Zircon U–Pb ages and petrogenesis of a tonalite–trondhjemite–granodiorite (TTG) complex in the northern Sanandaj–Sirjan zone, northwest

Iran: evidence for Late Jurassic arc–continent collision. Lithos 216:178–195

Baharifar AA (1997) New perspective on petrogenesis of the regional metamorphic rocks of Hamadan area, Iran. Unpublished M.Sc. Thesis (in Farsi), Tarbiat Moallem University of Tehran, Iran

Baharifar AA (2004) Petrology of metamorphic rocks in the Hamadan area. Unpublished Ph. D. Thesis (in Farsi), Tarbiat Moallem University of Tehran, Iran, 218 pp

Baharifar A, Moinevaziri H, Bellon H, Piqué A (2004) The crystalline complexes of Hamadan (Sanandaj–Sirjan zone, western Iran): metasedimentary Mesozoic sequences affected by Late Cretaceous tectono-metamorphic and plutonic events. CR Geosci 336:1443–1452

Baker DR (1998) The escape of pegmatite dikes from granitic plutons: constraints from new models of viscosity and dike propagation. Can Mineral 36:255–363

Boynton WV (1984) Cosmochemistry of the rare earth elements meteorite studies. In: Henderson P (ed) Rare earth element geochemistry. Elsevier Sciences, Amsterdam, pp 63–114

Braud J (1987) La suture du Zagros au niveau de Kermanshah (Kurdistan Iranian): reconstitution paleogeographique, evolution geodynamique, magmatique et structurale. Unpublished Ph.D. Thesis, Geodiffusion editeur, Paris

Brown M (2010) Melting of the continental crust during orogenesis: the thermal, rheological and compositional consequences of melt transport from lower to upper continental crust. Can J Earth Sci 47:655–694

Brown M (2013) Granite: from genesis to emplacement. Geol Soc Am Bull 125(7–8):1079–1113

Cerný P (1991) Rare-element granite pegmatites. Part I: anatomy and internal evolution of pegmatite deposits. Part II: regional to global relationships and petrogenesis. Geosci Can 18:49–81

Cerný P (1992) Geochemical and petrogenetic features of mineralization in rare element granitic pegmatites in the light of current research. Appl Geochem 7:393–416

Cerný P, Ercit TS (2005) The classification of granitic pegmatites revisited. Can Mineral 43:2005–2026

Cerný P, Meintzer RE, Anderson AJ (1985) Extreme fractionation in rare-element granitic pegmatites: selected examples of data and mechanisms. Can Mineral 23:381–421

Cerný P, London D, Novak M (2012) Granitic pegmatites as reflections of their source. Elements 8:289–294

Chappell BW, White AJR (1992) I and S-type granites in the Lachlan Fold Belt. Trans R Soc Edin Earth Sci 83:1–26

Chappell BW, White AJR (2001) Two contrasting granite types: 25 years later. Aust J Earth Sci 48:489–499

Chen CH, Lu HY, Lin W, Lee CY (2006) Thermal event records in SE China coastal areas: constraints from monazite ages of beach sands from two sides of the Taiwan Strait. Chem Geol 231:118–134

Chiu HY, Chung SL, Zarrinkoub MH, Mohammadi SS, Khatib MM, Iizuka Y (2013) Zircon U–Pb age constraints from Iran on the magmatic evolution related to Neotethyan subduction and Zagros orogeny. Lithos 162–163:70–87

Christiansen EH, Keith JD (1996) Trace element systematics in silicic magmas: a metallogenic perspective. In: Wyman D (ed) Trace element geochemistry of volcanic rocks, 12th edn. Geological Association of Canada Short Course Notes, Quebec, pp 115–151

Crowley JL, Brown RL, Gervais F, Gibson HD (2008) Assessing inheritance of zircon and monazite in granitic rocks from Monashee complex, Canadian Cordillera. J Petrol 49:1915–1929

Deer WA, Howie A, Zussman J (1982) Rock forming minerals. Longman, London, p 919

Dill HG (2015) Pegmatites and aplites: their genetic and applied ore geology. Ore Geol Rev 69:417–561

El Bouseily AM, El Sokkary AA (1975) The relation between Rb, Ba and Sr in granitic rocks. Chem Geol 16:207–219

Esna-Ashari A, Tiepolo M, Valizadeh MV, Hassanzadeh J, Sepahi AA (2012) Geochemistry and zircon U–Pb geochronology of Aligoodarz granitoid complex, Sanandaj–Sirjan zone, Iran. J Asian Earth Sci 43:11–22

Fazlnia A, Moradian A, Rezaei K, Moazzen M, Alipour S (2007) Synchronous activity of anorthositic and S-type granitic magmas in Chah-Dozdan Batholith, Neyriz, Iran: evidence of zircon SHRIMP and monazite CHIME dating. J Sci Islam Republ Iran 18:221–237

Foley SF, Wheller GE (1990) Parallels in the origin of the geochemical signatures of island arc volcanic and continental potassic igneous rocks: the role of residual titanites. Chem Geol 85:1–18

Frost RB, Barnes CG, Collins WJ, Arculus RJ, Ellis DJ, Frost CD (2001) A geochemical classification for Granitic Rocks. J Petrol 42:2033–2048

Gao P, Zheng YF, Zhao ZF (2016) Experimental melts from crustal rocks: a lithochemical constraint on granite petrogenesis. Lithos 266–267:133–157

Ghalamghash J, Mirnejad H, Rashid H (2009) Mixing and mingling of mafic and felsic magmas along the Neo-Tethys continental margin, Sanandaj–Sirjan zone, NW Iran: a case study from Alvand pluton. Neues Jahrb Mineral Abh 186(1):79–93

Gregory CJ, Rubatto D, Allen CM, Williams IS, Hermann J, Ireland T (2007) Allanite micro-geochronology: a LA-ICP-MS and SHRIMP U–Th–Pb study. Chem Geol 245:162–182

Hawthorne FC, Henry DJ (1999) Classification of the minerals of the tourmaline group. Eur J Mineral 11:201–215

Henderson P (1984) Rare earth element geochemistry. Elsevier Science, Amsterdam, p 501

Henry DJ, Guidotti CV (1985) Tourmaline as a petrogenetic indicator mineral: an example from the staurolite-grade metapelites of NW Maine. Am Mineral 70:1–15

Izadikian L (2009) Structural and petrofabric analysis of metamorphic rocks of Alvand mountain (south and southwest of Hamadan). Ph.D. Thesis in tectonic, Shahid Beheshti university, Tehran, Iran (in persian)

Karakas O, Degruyter W, Bachmann O, Dufek J (2017) Lifetime and size of shallow magma bodies controlled by crustal-scale magmatism. Nat Geosci 10:446–452

Linnen RL, Lichtervelde MV, Cerny P (2012) Granitic pegmatites as sources of strategic metals. Elements 8:275–280

Liu YS, Hu ZC, Zong KQ, Gao CG, Gao Sh, Xu J, Chen HH (2010) Reappraisment of zircon U–Pb isotope and trace element analyses by LA-ICP-MS. Chinese Sci Bull 55:1535–1546

London D (1999) Melt boundary layers and the growth of pegmatitic textures. Can Mineral 37:826–827 **(abstr.)**

London D (2005) Granitic pegmatites: an assessment of current concepts and directions for the future. Lithos 80:281–303

London D (2008) Pegmatites. Can Mineral 10:347p

London D (2009) The origin of primary textures in granitic pegmatites. Can Mineral 47:697–724

London D (2014a) A petrologic assessment of internal zonation in granitic pegmatites. Lithos 184–187:74–104

London D (2014b) Subsolidus isothermal fractional crystallization. Am Mineral 99:543–546

London D, Manning DAC (1995) Chemical variation and significance of tourmaline from SW England. Econ Geol 90:495–519

London D, Morgan GVI (2012) The pegmatite puzzle. Elements 8:263–268

Ludwig KR (2003) User's Manual for Isoplot/Ex, Version 3.0, A geochronological toolkit for Microsoft Excel Berkeley Geochronology Center Special Publication, v.4, Berkeley Geochronology Center, 2455 Ridge Road, Berkeley, CA 94709, USA

Mahmoudi S, Corfu F, Masoudi F, Mehrabi B, Mohajjel M (2011) U–Pb dating and emplacement history of granitoid plutons in the northern Sanandaj–Sirjan Zone, Iran. J Asian Earth Sci 41:238–249

Maniar PD, Piccoli PM (1989) Tectonic discrimination of granitoids. Geol Soc Am Bull 10:635–643

Manning DAC (1982) Chemical and morphological variation in tourmalines from the Hub Kapong batholith of Peninsular Thailand. Mineral Mag 45:139–147

Martin RF, Vito CD (2005) The patterns of enrichment in felsic pegmatites ultimately depend on tectonic setting. Can Mineral 43:2027–2048

Martin AJ, Gehrels GE, DeCelles PG (2007) The tectonic significance of (U, Th)/Pb ages of monazite inclusions in garnet from the Himalaya of central Nepal. Chem Geol 244:1–24

Masoudi F (1997) Contact metamorphism and pegmatites development in the region SW of Arak, Iran. Unpublished Ph.D. Thesis, University of Leeds, UK, 321p

McFarlane CRM (2016) Allanite U\Pb geochronology by 193 nm LA ICP-MS using NIST610 glass for external calibration. Chem Geol 438:91–102

McFarlane CRM, Luo Y (2012) U–Pb geochronology using 193 nm Excimer LA-ICP-MS optimized for in situ accessory mineral dating in thin sections. Geosci Can 39:158–172

McFarlane CRM, McKeough M (2013) Petrogenesis of the Kulyk Lake monazite-apatite-Fe(Ti)-oxide occurrence revealed using in situ LA-(MC)-ICP-MS trace element mapping, U–Pb dating, and Sm-Nd isotope systematics on monazite. Am Min 98:1644–1659

Mezeme EB, Cocherie A, Faure M, Legendre O, Rossi Ph (2006) Electron microprobe monazite geochronology of magmatic events: examples from Variscan migmatites and granitoids, Massif Central, France. Lithos 87:276–288

Middlemost EAK (1985) Magmas and magmatic rocks: an introduction to igneous petrology. John Wiley and Sons Inc, New York, p 266

Mohajjel M, Fergusson CL, Sahandi MR (2003) Cretaceous-Tertiary convergence and continental collision, Sanandaj–Sirjan zone, Western Iran. J Asian Earth Sci 21:397–412

Nabelek PI, Whittington AG, Sirbescu MC (2010) The role of $H_2O$ in rapid emplacement and crystallization of granite pegmatites: resolving the paradox of large crystals in highly undercooled melts. Contrib Mineral Petrol 160:313–325

Nachit H, Razafimahefa N, Stussi JM, Carron JP (1985) Composition chimique des biotites et typologie magmatique des granitoides. CR Heb Acad Sci 301:813–818

Paquette JL, Tiepolo M (2007) High resolution (5 µm) U-Th–Pb isotope dating of monazite with excimer laser ablation (ELA)-ICPMS. Chem Geol 240:222–237

Pearce JA, Harris NB, Tindle AG (1984) Trace element discrimination diagrams for the tectonic interpretation of granitic rocks. J Petrol 25:956–983

Rashidnejad-Omran N, Emami MH, Sabzehei M, Rastad E, Bellon H (2002) Lithostratigraphy and Paleozoic to Paleocene history of some metamorphic complexes from Muteh area, Sanandaj–Sirjan zone (southern Iran). CR Geosci 334:1185–1191

Sepahi AA (1999) Petrology of the Alvand plutonic complex with special reference on granitoids. Unpublished Ph.D. Thesis (in Farsi), Tarbiat Moallem University of Tehran, Iran, 326p

Sepahi AA (2008) Typology and petrogenesis of granitic rocks in the Sanandaj–Sirjan metamorphic belt, Iran: with emphasis on the Alvand plutonic complex. Neues Jahrb Geol P-A 247:295–312

Sepahi AA, Whitney DL, Baharifar AA (2004) Petrogenesis of andalusite-kyanite-sillimanite veins and host rocks, Sanandaj–Sirjan metamorphic belt, Hamadan, Iran. J Metamorph Geol 22:119–134

Sepahi AA, Shahbazi H, Siebel W, Ranin A (2014) Geochronology of plutonic rocks from the Sanandaj–Sirjan zone, Iran and new zircon and titanite U-Th-Pb ages for granitoids from the Marivan pluton. Geochronometria 41:207–215

Shahbazi H (2010) Petrology of igneous rocks and migmatitic complex of Alvand and intrusive body of Almogholagh, Hamedan and their genetic relationship. Unpublished Ph.D. Thesis (in Persian), ShahidBeheshti University, Tehran, Iran, 189p

Shahbazi H, Siebel W, Pourmoafee M, Ghorbani M, Sepahi AA, Shang CK, Vousoughi-Abedini M (2010) Geochemistry and U–Pb zircon geochronology of the Alvand plutonic complex in Sanandaj–Sirjan Zone (Iran): new evidence for Jurassic magmatism. J Asian Earth Sci 39:668–683

Shand SJ (1943) Eruptive Rocks, their genesis, composition, classification and their relation to ore deposits, 3rd edn. John Wiley and Sons, New York, p 448

Sheikholeslami R, Bullen H, Emami MH, Sabzehei M, Pique A (2003) New structural and $K^{40}$–$Ar^{40}$ data for the metamorphic rocks in Neyriz area (Sanandaj–Sirjan zone, southern Iran): their interest for an overview of the Neo-Tethyan domain in the Middle East. CR Geosci 335:981–991

Simmons WB, Webber KL (2008) Pegmatite genesis: state of the art. Eur J Mineral 20:421–438

Simmons WB, Webber KL, Falster AU, Nizamoff JW (2003) Pegmatology—Pegmatite mineralogy, petrology and petrogenesis. Rubellite Press, New Orleans, p 176

Thomas R, Davidson P (2015) Comment on "A petrologic assessment of internal zonationin granitic pegmatites" by David London (2014). Lithos 212–215:462–468

Thomas R, Förster HJ, Heinrich W (2003) The behavior of boron in a peraluminous granite–pegmatite system and associated hydrothermal solutions: a melt and fluid inclusion study. Contrib Mineral Petrol 144:457–472

Thomas R, Davidson P, Beurlen H (2012) The competing models for the origin and internal evolution of granitic pegmatites in the light of melt and fluid inclusion research. Miner Petrol 106:55–73

Thompson RN (1982) Magmatism of the British Tertiary volcanic province. Scot J Geol 18:9–107

Valizadeh MV, Cantagrel JM (1975) Premieres données radiométriques (K–AretRb–Sr) sur les micas du complexes magmatique du Mont Alvand, Pres Hamadan (Iran occidental). CR Acad Sci Paris 281:1083–1086

Vidal O, Goffé B, Bousquet R, Parra T (1999) Calibration and testing of an empirical chloritoid-chlorite Mg-Fe exchange thermometer and thermodynamic data for daphnite. J Metamorph Geol 17:25–39

Webber KL, Simmons WB, Falster AU, Foord EE (1999) Cooling rates and crystallization dynamics of shallow level pegmatite–aplite dikes, San Diego County, California. Am Mineral 84:708–717

Wedepohl KH (1995) The composition of the continental crust. Geochim Cosmochim Acta 59:1217–1232

Wilson M (2007) Igneous Petrogenesis. Unwin Hyman, London, p 461p

Yajam S, Montero P, Scarrow JH, Ghalamghash J, Razavi SMH, Bea F (2015) The spatial and compositional evolution of the Late Jurassic Ghorveh-Dehgolan plutons of the Zagros Orogen, Iran: sHRIMP zircon U–Pb and Sr and Nd isotope evidence. Geol Acta 13:25–43